Fall 11-12-2012

Electron-Phonon Coupling and Structural Phase Transitions on Au/Mo(112)

Keisuke Fukutani
University of Nebraska-Lincoln, nekocat@unl.edu

Fukutani, Keisuke, "Electron-Phonon Coupling and Structural Phase Transitions on Au/Mo(112)" (2012). *Theses, Dissertations, and Student Research: Department of Physics and Astronomy*. 22.
http://digitalcommons.unl.edu/physicsdiss/22

Electron-Phonon Coupling and Structural Phase Transitions on Au/Mo(112)

by

Keisuke Fukutani

A DISSERTATION

Presented to the Faculty of

The Graduate College at the University of Nebraska

In Partial Fulfillment of Requirements

For the Degree of Doctor of Philosophy

Major: Physics and Astronomy

Under the Supervision of Professor Peter A. Dowben

Lincoln, Nebraska

November, 2012

Electron-Phonon Coupling and Structural Phase Transitions on Au/Mo(112)

Keisuke Fukutani, Ph.D.

University of Nebraska, 2012

Advisor: Peter A. Dowben

The electronic structures, many-body interactions and Fermi surface topologies of Au/Mo(112) were investigated in detail and were found to play important roles in the newly discovered order-disorder structural phase transition of the system. First, the high-resolution angle-resolved photoemission spectroscopy was utilized to characterize the electronic band structure of Mo(112) in far greater details than before. This elucidated the existence of several surface-derived states and their dispersion relations in high precisions near the Fermi level, as well as the symmetries of the bulk and surface electronic states, which are in good quantitative agreement with the *ab-initio* calculations. Such thorough understanding of the electronic states on Mo(112) made it possible to investigate the more complex electronic structure and many-body interactions in the Au overlayers formed on the Mo(112) surface and their interface. Upon the Au adsorption on Mo(112) substrate, the Au overlayer states are seen to hybridize with those of Mo substrate, which resulted in the formation of the several surface resonance bands, exhibiting high electronic localization near the surface and interface of the combined system. Furthermore, the electron-phonon coupling, involving these surface resonance states, is found to cause strong effective mass enhancement of the electrons near the Fermi level, which can contribute significantly to the surface lattice instability. In particular, for the (4x1) Au overlayer on Mo(112), the noticeable temperature-dependent changes in the Fermi surface contours were observed near the room temperature and were

seen to act in favor of the stronger nesting condition and phonon-induced lattice distortions. The combination of the identified strong electron-phonon coupling and the critical Fermi surface topology near the room temperature likely relates to the overlayer lattice instability on the Au/Mo(112) system. In accord with the above general expectation, the order-disorder structural phase transitions were identified on Au/Mo(112) above the room temperature, which is characterized by the abrupt changes in the effective surface Debye temperature, indicative of significant softening of phonons on Au/Mo(112) across the transition. The sequence of these studies likely evidences that the strong electron-phonon coupling and the temperature-dependent Fermi surface topology are indispensable in driving the order-disorder transitions on Au/Mo(112).

Acknowledgements

It was certainly not possible for me to make it through my journey towards the Ph.D. without the people who, in many ways, supported me in accomplishing this work. I would like to express my sincere gratitude for all the individuals for their supports in their own way. The following list has no order.

To my wife Naomi, for her patience, caring and understanding throughout the entire journey towards my Ph.D.

To my son Yuto, for being there.

To my father Akira and my mother Ayako, for their supports and understanding, and especially for letting me pursue what I love.

To my grandfather Hideo in heaven and my grandmother Yaeko, for all the caring and supports during my journey towards Ph.D.

To my friend Susumu Hiragishi, for his friendship and for his support in the times of difficulty.

To my group members, Xin Zhang, Lingmei Kong, Thomas Scott, Shi Cao, Yaroslav Ketsman, for helping me during the experiments, and for sharing the thoughts with me. To Dr. Juan Colón Santana, for his friendship, understanding and valuable scientific conversations. To his wife Dr. Olha Ketsman, for her friendship and understanding. To Dr. Ning Wu, for his help and supports and for closely mentoring me in gaining valuable knowledge and experience in experiments.

To the graduate students and scientists at Hiroshima Synchrotron Radiation Center, Hirokazu Hayashi, Takafumi Habuchi, Daisuke Hirayama, Yorito Nagata, Taiki Horike Dr. Jian Jiang, Dr. Eike F. Schwier, Dr. Hideaki Iwasawa and Dr. Koji Miyamoto, for numerous valuable scientific conversations and for their generous help and supports in performing the experiments at BL-1.

To Prof. David Wisbey, for introducing me to the basics of UHV chambers and closely mentoring me.

To Dr. Yaroslav B. Losovyj, for closely mentoring me during the experiments at CAMD, and most of all, for introducing me to the world of Mo(112)

To Dr. Tula R. Paudel, for numerous scientific conversations, for his band structure calculations, and most of all, for working with me very patiently.

To Prof. Evgeny Y. Tsymbal, for number of valuable scientific discussions and for his kind helps on acquiring the important knowledge.

To James Glassbrener, for numerous valuable scientific discussions and for his computational assistances.

To Prof. Kirill Belashchenko, for number of precise scientific conversations.

To Prof. Ivan N. Yakovkin, for many of his band structure calculations, which are of critical importance in compiling this work.

To my committee members, Prof. Christian Binek, Prof. Alexei Gruverman, Prof. Wei-Ning Mei, and Prof. Herman Batelaan, for their interest and the time they devoted in reviewing my work.

To Prof. Kenya Shimada, for the close collaborations and the numerous valuable scientific conversations and advices, which were of critical importance to compiling this work.

And, last, but not the least, to my advisor Prof. Peter A. Dowben, who gave me countless lessons and patiently mentored me throughout the entire course of my work. His generous supports were not limited to science, and his kind help and understanding during the hard time are unforgettable. Thank you very much for your unlimited supports and I am proud to be your student!

Table of contents

Chapter 1
Introduction

The physics of solids is essentially the physics of interacting many-body system. Naturally, such complex interactions are responsible for many of the phenomena observed in the bulk as well as near the surfaces of solids. Therefore, the understanding of the solids must involve the detailed investigation of various types of many-body interactions. In particular, electron-phonon coupling, one type of many-body interactions, plays a critical role in many types of phenomena, ranging from surface reconstructions to superconductivity [1]. Of our interest here is the role of electron-phonon coupling in the surface structural phase transitions, in which the surface lattice undergoes the temperature-dependent structural distortion. Perhaps the simplest example of a phonon-induced lattice distortion is the Peierls' transition in one-dimensional atomic chain, which is caused by the so-called perfect phonon nesting condition of the Fermi surface, possible in one-dimension [1,2]. Although in two and higher dimensions, the perfect nesting condition is never strictly satisfied it has been pointed out [3] that given strong electron-phonon coupling and nesting condition (not necessarily perfect), the structural phase transition can occur through the mechanism similar to the Peierls' transition. It is important to note here that the strong nesting conditions of Fermi surface are usually expected and observed for highly anisotropic materials such as for the (110) surfaces of *fcc* crystals or (112) surfaces of *bcc* crystals.

The Mo(112) surface is known to exhibit highly anisotropic structural as well as electronic properties [5-10], which is expected to provide the good nesting properties [11]. On the other hand, the previously determined electron-phonon coupling parameters for

Mo [12,13] and Mo(112) [14] indicates relatively small strength of the interactions between the electrons and phonons, perhaps due to the fact that the phonon density of states is weighted towards relatively high energy (> 20 meV). However, in principle, the softer (lower energy) phonon modes can be induced on Mo(112) by adsorbing the atoms whose crystalline structure exhibits soft phonon modes. Our choice was Au atoms. We believe this choice is a feasible one, because it is known to form the commensurate overlayer structure on Mo(112) [15,16] preserving the anisotropy of the system besides (possibly) inducing the softer phonon modes. Thus, based on the above logic, the system for the investigations in this study is Au/Mo(112). The goals of our studies are to quantitatively characterize the electron-phonon coupling (and other many-body interactions) of Au/Mo(112), to identify the possible existence of structural phase transitions, and ultimately to unveil the fundamental mechanisms by which the two phenomena are interlinked.

In elucidating the complex many-body interactions in Au/Mo(112), particularly the electron-phonon coupling, angle-resolved photoemission spectroscopy (ARPES) is considered one of the premier tools, as it directly extracts the electronic band structures of solids as well as the single-particle excitation spectra [17-19]. When ARPES spectra are combined with density functional theory (DFT) calculations of the electronic band structure and Eliashberg function [20], it becomes possible to characterize the nature of electron-phonon coupling in Au/Mo(112) and other many-body interactions in the solids with great accuracy. Another attracting feature of ARPES is its capability of providing the experimental images of the Fermi surface of solids, which yields critical insights into the nesting conditions in solids and hence the ‘effectiveness’ of electron-phonon coupling in driving the structural instability. Thus, ARPES is our natural choice of experimental probe to investigate the many-body interactions in Au/Mo(112). In search for the surface structural instability, a natural choice of experimental technique is low energy electron diffraction (LEED), which is surface-sensitive and capable to characterizing the static as well as the dynamic properties of the surfaces and overlayers. Utilizing the abovementioned experimental and theoretical techniques, we now start to explore the many-body interactions and the fundamental mechanisms of structural phase transitions on Au/Mo(112).

References

[1] H. Bruus and K. Flensberg, *Many-Body Quantum Theory in Condensed Matter Physics* (Oxford University Press, 2004), ISBN 9780198566335.

[2] R. E. Peierls, *Quantum Theory of Solids* (Oxford University Press, 2001), ISBN 9780198507819.

[3] G. Gruner, *Density Waves in Solids* (Perseus Publishing, 1994), ISBN 0738203041.

[4] S-K Chan and V. Heine, *J. Phys.* F, **3**, 795 (1973).

[5] T. McAvoy, J. Zhang, C. Waldfried, D.N. McIlroy, P.A. Dowben, O. Zeybek, T. Bertrams, and S.D. Barrett, *European Physical Journal* B **14**, 747 (2000).

[6] I.N. Yakovkin, J. Zhang, and P.A. Dowben, *Phys. Rev.* B **63**, 115408 (2001).

[7] H.-K. Jeong, T. Komesu, I.N. Yakovkin, and P.A. Dowben, *Surface Science Letters* **494**, L773 (2001).

[8] N. Wu, Ya. B. Losovyj, Z. Yu, R.F. Sabirianov, W.N. Mei, N. Lozova, J.A. Colón Santana, and P.A. Dowben, *J. Phys. Cond. Matter* **21**, 474222 (2009).

[9] I.N. Yakovkin, *Surf. Sci*. **389**, 48 (1997).

[10] K. Fukutani, H. Hayashi, I.N. Yakovkin, T.R. Paudel, T. Habuchi, D. Hirayama, J. Jiang, H. Iwasawa, K. Shimada, N. Wu, E.Y. Tsymbal, Ya. B. Losovyj and P.A. Dowben, *Phys. Rev.* B **85**, 155435 (2012).

[11] I.N. Yakovkin, K. Fukutani, H. Hayashi, J. Jiang, T. Horike, Y. Nagata, T. Habuchi, D. Hirayama, H. Iwasawa, K. Shimada, Ya. B. Losovyj and P.A. Dowben, *Phys. Rev.* B **86**, 125401 (2012).

[12] S.Y. Savrasov and D.Y. Savrasov, *Phys. Rev.* B **54**, 16487 (1996).

[13] N. Wu, Ya. B. Losovyj, K. Fukutani and P.A. Dowben, *J. Phys.: Condens. Matter* **22**, 245501 (2010).

[14] I.N. Yakovkin and P.A. Dowben*, J. Phys.: Condens. Matter* **23**, 225503 (2011).

[15] K. Fukutani, Ya. B. Losovyj, N. Lozova, I.N. Yakovkin, N. Wu and P.A. Dowben, *Journal of Electron Spectroscopy and Related Phenomena* **184**, 318 (2011).

[16] K. Fukutani, N. Lozova, S.M. Zuber, P.A. Dowben, P. Galiy and Ya. B. Losovyj, *Applied Surface Science* **256**, 4796 (2010).

[17] S. Hufner, *Photoelectron Spectroscopy* (Springer, 2003), ISBN 3540418024

[18] S. Hufner (Ed.), *Very High Resolution Photoelectron Spectroscopy* (Springer, 2007), ISBN 9783540681304.

[19] Ph. Hofmann, I. Yu. Sklyadneva, E.D.L Rienks and E.V. Chulkov, *New Journal of Physics* **11**, 125005 (2009).

[20] Eliashberg function characterizes the nature of electron-phonon coupling for any given material. The detailed derivation is presented e.g. in “G. Grimvall, *The Electron-Phonon Interaction in Metals* (Selected Topics in Solid State Physics XVI), 1st ed. (Elsevier Science Ltd, 1981)”.

Chapter 2
Photoemission spectroscopy

2.1: Basic principles of photoemission

2.1.1 Fermi's golden rule

In photoemission process, the incident electromagnetic wave (or in the language of second quantization, the photon) imposes a harmonic time-dependent perturbation to the system of electrons in the solid. Therefore, the photoemission transition rate is given by the Fermi's golden rule:

$$w = 2\pi \left| \langle \Psi_f | \Delta | \Psi_i \rangle \right|^2 \delta(E_f - E_i - \omega) , \tag{2.1}$$

where w is the transition probability from the initial state Ψ_i to final state Ψ_f per unit time (i.e., transition rate) and Δ is the perturbation operator due to the incident electromagnetic field (note that in this treatment of photoemission, the electromagnetic field is not quantized and thus the vector potential A of the incident electromagnetic wave is just the vector $A(r)$, *not* an operator). In the photoemission experiment, the intensity of signal into the detector is determined by the photocurrent I, proportional to w (or equivalently, the square of the matrix element). The above expression is exact up to the 1st order in the time-dependent perturbation. Therefore if we know everything about the initial and final states (Ψ_i and Ψ_f), we can calculate the transition probability and the corresponding photoemission current (the photoelectron current out of our sample), and we know everything about the photoemission process (Δ can be determined fairly accurately). However, in reality, the situation is not that simple. The wave functions, Ψ_i and Ψ_f, for the initial and final states are enormously complicated by the fact that there are $\sim 10^{23}$

electrons and ions in the real solid and they are *all mutually interacting with each other*. In fact, *the most complex system* for which we can solve the many-body Schrodinger equation exactly is hydrogen molecular ion (H_2^+). Anything more complex than H_2^+ is impossible to solve analytically.

2.1.2: Photoemission Perturbation Hamiltonian

In order to evaluate the transition rate *w*, we first write the total Hamiltonian of the crystal system in the presence of external electromagnetic field.

$$\begin{aligned} H &= \frac{1}{2m}\left(p + \frac{eA}{c}\right)^2 - eU - e\phi \\ &= \frac{p^2}{2m} - eU + \frac{e}{2mc}\left(p\cdot A + A\cdot p\right) + \frac{e^2}{2mc^2}A\cdot A - e\phi \end{aligned}, \tag{2.2}$$

where $A = A(r, t)$ is the vector potential of external electromagnetic field and U is the crystal potential. The perturbation Hamiltonian $H'(t)$ can be identified as:

$$H'(t) = \frac{e}{2mc}\left(p\cdot A + A\cdot p\right) + \frac{e^2}{2mc^2}A\cdot A - e\phi . \tag{2.3}$$

We first simplify the above expression by ignoring the term with $A\cdot A$, which is usually small compared to the $p\cdot A$ terms (in the view of second quantization, this small term corresponds to two-photon absorption). Then,

$$H'(t) = \frac{e}{2mc}\left(p\cdot A + A\cdot p\right) - e\phi . \tag{2.4}$$

Now, we rewrite the first term in a simpler form (note that this is *not* an approximation). But, since p is an *operator*, we must be careful in doing this. Thus, we look at how $p\cdot A$ operates on the test function $f = f(r)$.

$$p\cdot Af(r) = -i\nabla\cdot(Af) = -i\left[f(\nabla\cdot A) + A\cdot\nabla f\right]. \tag{2.5}$$

If we use the Coulomb gauge for which $\nabla\cdot A = 0$, we have

$$\begin{aligned} &p\cdot Af(r) = -i\left[A\cdot\nabla f\right] = A\cdot pf(r) \\ &\Rightarrow p\cdot A = A\cdot p \end{aligned}, \tag{2.6}$$

which means the momentum operator p and vector potential A commute (note this is true only because A is not an operator). If we further take the gauge for which $\phi = 0$ (which is *always* possible), we finally have

$$\begin{aligned} H'(t) &= \frac{e}{mc}A\cdot p \\ &= \frac{e}{mc}A_0 e^{i(k\cdot r-\omega t)}\cdot p \end{aligned}, \tag{2.7}$$

and the time-independent part Δ is identified as

$$\Delta = \frac{e}{mc}\left(A_0\cdot p\right)e^{ik\cdot r}. \tag{2.8}$$

Note that the above derivation is essentially exact for *H'*(*t*) and Δ up to this point (in the case of *classical* field as opposed to quantized field for *A*). Now, we make our first approximation to the vector field *A*.

$$e^{ik\cdot r} = 1 + ik\cdot r + \cdots \approx 1. \tag{2.9}$$

Thus, we are assuming the vector field *A*, and hence the electromagnetic field, is *constant in space*. This is called *electric dipole approximation* (or simply *dipole approximation*) Thus, within the dipole approximation, Δ is given by

$$\Delta = \frac{e}{mc}A_0\cdot p, \tag{2.10}$$

where A_0 is the amplitude of the vector field (= constant). We now have the ingredients to describe the photoemission as soon as the initial and final states (Ψ_i and Ψ_f) are given.

2.1.3 Validity of dipole approximation

The physical interpretation of dipole approximation is that the electromagnetic wave is approximated by spatially constant electric field oscillating in time (with no magnetic field at all). This may seem a crude approximation. However, for the photoemission with ultraviolet light, which is utilized in this study, the wavelength of electromagnetic wave (~1000 Å) is much larger than the interatomic distance (~1 Å) of most crystals and therefore, the assumption of spatially constant electric field is a good approximation. Furthermore, since the magnetic field only couples to the spin magnetic moment of electrons that is small (for the purpose of describing photoemission process), the contribution of magnetic dipole term to the photoemission matrix element is negligible in the ultraviolet region.

2.1.4 What does photoemission spectroscopy measure?

In order to correctly interpret the photoemission spectra, it is important to understand the photoemission transition rate with account for the many-body nature of the system (system of ~10^{23} electrons and ions). As mentioned earlier, the photoemission transition rate is given by

$$w = 2\pi \left| \langle \Psi_f | \Delta | \Psi_i \rangle \right|^2 \delta(E_f - E_i - \omega) . \tag{2.1}$$

Note that this expression makes no reference to whether the state vectors are of single particle or many-particle system. Thus, we consider the system of N electrons and assume that N-electron initial state $|\Psi_i\rangle$ with energy E_i can be decomposed into two parts; the state of single electron, which is *to be* photoemitted $\left|\phi_i\right\rangle$, and the state of remaining N - 1 electrons $\left|\Psi_i^{N-1}\right\rangle$. Thus, the initial state can be written as

$$\left|\Psi_i\right\rangle = C\left|\phi_i\right\rangle\left|\Psi_i^{N-1}\right\rangle, \tag{2.11}$$

where C is the operator that anti-symmetrizes the entire wave function. The final state can be similarly decomposed into the states of photoemitted electron with kinetic energy E_{kin} and the remaining N - 1 electrons and we can write

$$\left|\Psi_f\right\rangle = C\left|\phi_f\right\rangle\left|\Psi_f^{N-1}\right\rangle. \tag{2.12}$$

Thus the photoemission matrix element is written as

$$\left\langle\Psi_f\right|\Delta\left|\Psi_i\right\rangle = \left[\left\langle\Psi_f^{N-1}\right|\left\langle\phi_f\right|C^*\right]\Delta\left[C\left|\phi_i\right\rangle\left|\Psi_i^{N-1}\right\rangle\right] = \left\langle\phi_f\right|\Delta\left|\phi_i\right\rangle\left\langle\Psi_f^{N-1}\middle|\Psi_i^{N-1}\right\rangle. \tag{2.13}$$

The above expression tells us that the photoemission matrix element consists of single-electron matrix element and the overlap integral. The overlap integral is nothing but the projection of initial N-1 electron state onto the final N-1 electron state, and thus tells us *how much* the initial and final state wave functions *overlap* (more the overlap, larger the overlap integral). In general, the initial and final N-1 electron states will be different because of the *excitation* caused by the removal (photoemission) of one electron. Thus, the final N-1 electron states is written as the superposition of the energy eigenstates of an appropriate Hamiltonian,

$$\left|\Psi_f^{N-1}\right\rangle = \sum_s a_s\left|\Psi_s^{N-1}\right\rangle \,. \tag{2.14}$$

Thus, the transition rate can be written as

$$w = 2\pi\left|\left\langle\phi_f\right|\Delta\left|\phi_i\right\rangle\right|^2\sum_s\left|\left\langle\Psi_s^{N-1}\middle|\Psi_i^{N-1}\right\rangle\right|^2\delta(E_f + E_{N-1} - E_N - \omega) \,. \tag{2.15}$$

If we take into account the finite temperature effect, we obtain

$$w = 2\pi \left| \langle \phi_f | \Delta | \phi_i \rangle \right|^2 \frac{1}{Z} \sum_s \left| \langle \Psi_s^{N-1} | \Psi_i^{N-1} \rangle \right|^2 e^{-\beta E_N} \delta(E_f + E_{N-1} - E_N - \omega) , \tag{2.16}$$

where Z is the partition function.

In order to understand the meaning of the transition rate, we introduce so-called single-particle Green's function for the many-electron system

$$G(k,t) = -i\theta(t) \left\langle \left[c_{k,t}, c_{k,0}^{+} \right]_{+} \right\rangle , \tag{2.17}$$

where the $c_{k,t}$ and $c^{+}_{k,0}$ are the annihilation operator for electron with momentum k at time t and the creation operator for electron with the same momentum k at time 0, respectively. The square bracket denotes the anti-commutator and $\langle ... \rangle$ denotes the thermal average. Roughly speaking, the above Green's function represents the probability that if the electron with momentum k is added to the system at time 0, the system is found still with added electron with k at later time t. If we represent this Green's function in the complete basis of the total Hamiltonian H, then we have

$$G(k,t) = i\theta(t) \frac{1}{Z} \sum_n e^{i(E_n - E_m)t} \langle n | c_{k,t} | m \rangle \langle m | c_{k,0}^{+} | n \rangle (e^{-\beta E_n} + e^{-\beta E_m}) , \tag{2.18}$$

where the partition function Z and Boltzmann factors $e^{-\beta E_i}$ account for the finite temperature. If we transform the Green's function from time domain to frequency domain (with complex frequency to ensure the convergence),

$$\begin{aligned} G(k,\omega) &= \int e^{i(\omega + i\delta)t} G(k,t) dt \\ &= \frac{1}{Z} \sum_n \langle n | c_{k,t} | m \rangle \langle m | c_{k,0}^{+} | n \rangle \frac{e^{-\beta E_n} + e^{-\beta E_m}}{\omega + E_n - E_m + i\delta} , \end{aligned} \tag{2.19}$$

where δ is a positive infinitesimal. Given the Green's function, its imaginary part contains very important information about how the many-electron system responds to the addition or removal of one electron.

$$\begin{aligned} A(k,\omega) &= -\frac{1}{\pi}\operatorname{Im} G(k,\omega) \\ &= \frac{1}{Z}\sum_n \langle n|c_{k,t}|m\rangle\langle m|c_{k,0}^{+}|n\rangle\left(e^{-\beta E_n}+e^{-\beta E_m}\right)\delta(\omega+E_n-E_m) \\ &= \frac{1+e^{-\beta\omega}}{Z}\sum_n \left|\langle n|c_{k,t}|m\rangle\right|^2 e^{-\beta E_m}\delta(\omega+E_n-E_m) \end{aligned} \tag{2.20}$$

This function, called the *spectral function*, is nothing but the sum of all the probabilities (or matrix elements) of transitions from the initial many-electron state $|m\rangle$ to the final many-electron state $|n\rangle$ during which the removal of electron with momentum *k* and energy ω occurs. Note that the partition function and Boltzmann factor appears as weighting factors to account for the finite temperature. Thus, the spectral function $A(\omega, k)$ describes the *single-particle excitation spectrum* of many-electron system as a function of energy and momentum.

At this point, the similarities between the expression for the photoemission transition rate and the spectral function can be identified. In fact, if $A(\omega, k)$ is multiplied by the Fermi function $1/(1+e^{-\beta\omega})$, we obtain

$$w = 2\pi\left|\langle\phi_f|\Delta|\phi_i\rangle\right|^2 f(\omega,T)A(\omega,k) \tag{2.21}$$

Thus, in principle, the photoemission spectroscopy measures the single-particle spectral function (or equivalently the excitation spectrum of removal of one electron (or creation of a hole)).

2.1.5 General form of spectral function

It can be shown that the single-particle Green's function introduced above can always be written in the form:

$$G(k,\omega)=\frac{1}{\omega-\xi(k)-\Sigma(k,\omega)+i\delta}, \tag{2.22}$$

where $\xi(k)$ is the eigenvalue of the Hamiltonian that is bilinear in creation and annihilation operators (such as free electron Hamiltonian), and $\Sigma(\omega, k) = \Sigma_R(\omega, k) + i\Sigma_I(\omega, k)$ is so-called self-energy which can be considered as (complex) energy correction to $\xi(k)$, which arises from the perturbative terms in the Hamiltonian that is *not* bilinear in creation and annihilation operators. Thus, taking the imaginary part of this Green's function, the general form of spectral function can be written as

$$A(k,\omega)=-\frac{1}{\pi}\frac{\Sigma_I(k,\omega)}{\left[\omega-\xi(k)-\Sigma_R(k,\omega)\right]^2+\Sigma_I(k,\omega)^2}. \tag{2.23}$$

Note that the small imaginary part δ has been absorbed into Σ_I. When the spectral function is written in this form with the introduction of self-energy, it can be given a rather clear interpretation. Evidently the spectral function is a peaked function in k as well as in ω. In the absence of many-body interaction (i.e., when the Hamiltonian is bilinear), the self-energy vanishes and the spectral function is a delta function peaked at $\xi(k)$ (in the limit $\Sigma \rightarrow 0$). For electrons, such spectral function gives the picture of their energy band structure in the absence of interactions. When many-body interactions are *turned on* (irrespective of the nature of the interactions), generally the self-energy becomes finite. According to the above general expression for the spectral function, it can be seen that the real part of self-energy shifts the peak of the spectral function and the imaginary part gives rise to the finite width.

2.2 Angle-resolved photoemission spectroscopy

2.2.1 Band structure mapping

As introduced above, photoemission spectroscopy, in principle, measures the spectral function and hence can be used to extract the electronic band structure, as well as the nature of the many-body interactions in solids in $E(k)$ space (via the analysis of self-energy). In this section, we describe how the experiments are carried out in practice and how the acquired photoemission spectra can be interpreted in terms of spectral function. Figure 2.1 shows the common setup of photoemission experiment. There are several types of photon sources available today, including gas discharge lamp, X-ray tube, synchrotron light source, and more recently, laser light source. Discharge lamps filled with noble gas (such as He, Kr and Xe) can be used as a source of monochromatic light with the frequency given by the energy difference of atomic energy levels. Synchrotron radiation light can also be utilized as a photon source. Synchrotron light sources have several advantages over discharge lamps. First, the frequency (or energy) of the photon can be tuned within the wide range, which allows the access to wider range of information than when utilizing the discharge lamps. Second, the synchrotron light is highly plane-polarized, and thus depending on the orientation of the light polarization with respect to the sample surface, yields different information. Such polarization dependence can be utilized, for example, to infer the symmetry of the electronic states under investigation as will be discussed below.

As the photon impinges on the sample surface and the photoelectrons are ejected, photoelectron analyzer collects those electrons within certain solid angle and measures their kinetic energies. The schematic representation of the relations between the electronic states in solid and photoemission spectrum is shown in Figure 2.2.

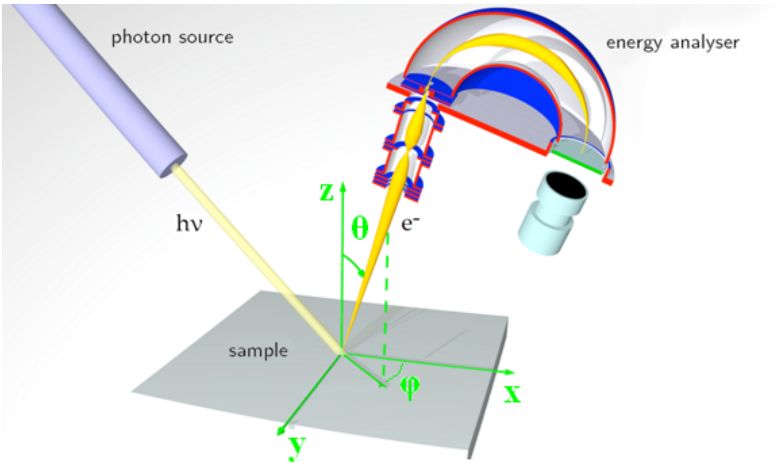

Figure 2.1: A common setup of photoemission experiment. The photons are incident on the sample within the *xz*-plane and excite the electrons (photoelectrons) from the sample. The energy analyzer detects the kinetic energy of the photoelectrons leaving at an angle (θ, φ) with θ measured relative to the surface-normal of the sample and φ measured relative to the *x*-axis.

If we tentatively assume that the creation of the hole will not give a rise to any relaxation of the remaining N-1 electrons (i.e., the initial N-1 electron state is the same as final N-1 electron state, called *frozen orbital approximation*), then the kinetic energy (E_{kin}) of photoelectrons are given by

$$E_{kin} = h\nu - \Phi - E_{bin} \ , \tag{2.24}$$

where $h\nu$ is the photon energy, Φ is the work function (i.e., potential "step" at the solid-vacuum interface) and E_{bin} is the binding energy of the initial electronic state. Thus, collecting the photoelectrons as a function of the measured kinetic energy can roughly be thought to represent a "copy" of the electronic distribution in solid as a function of energy. Of course, this view is an oversimplification. As seen in Figure 2.2 (e.g. for the core levels), the sharp peaks of energy levels (in frozen orbital approximation) are broadened in the photoemission spectrum, which is obviously an artifact of the experiment. Although there are many mechanisms causing such broadening due to the experiment (finite width of photon energy, inelastic scattering of photoelectrons within the sample etc.), it is important to note that the photoelectron detection process itself contributes to the broadening (i.e., finite instrumental resolution). Therefore, in the attempt of extracting the band structure (or the spectral function) of the solid, it is desirable to use the detector with as high-resolution as possible. That is, the smaller artificial broadening in the photoemission spectrum. After all, that is essentially the only thing we can directly control.

Up to this point, the discussion was limited to the photoemission spectra taken for the photoelectrons leaving the sample surface at fixed angle (particularly for θ, $\varphi = 0$), which gives the electronic structure as a function of energy at certain point in the Brillouin zone. It is, of course, possible to collect the photoelectrons leaving the sample at various non-zero angles (θ, φ). The initial states of those electrons (i.e., the state from which the electron was photoemitted) generally have finite momentum parallel to the sample surface (away from the surface Brillouin zone center). Figure 2.3 shows, as an example, the bulk Brillouin zone of *fcc* crystal and the projected surface Brillouin zone for its (110) surface. For any given angle (θ, φ) and photon energy, the photoemission probes the electronic structure of certain *k*-point according to the momentum conservation. Since in the direction parallel to sample surface, the potential has translational invariance within and outside the crystal (of course, within the crystal, the translational invariance is discrete), the surface-parallel momentum is conserved up to the crystal momentum:

$$k_{f\|} = k_{i\|} + G \ , \tag{2.25}$$

where G is an appropriate reciprocal lattice vector. On the other hand, the momentum perpendicular to the sample is generally not conserved due to the presence of the potential "step" at the solid-vacuum interface, called inner potential V_0. Thus, the direct determination of the wave vector in initial state (k_i) can be done only for the $k_{||}$ components and they can be related to the photoemission angles (θ, φ) by

$$k_{\|} = \begin{bmatrix} k_x \\ k_y \end{bmatrix} = \sqrt{2mE_{kin}} \sin\theta \begin{bmatrix} \cos\varphi \\ \sin\varphi \end{bmatrix} . \tag{2.26}$$

Therefore, measuring the photoemission spectrum at many different angles of emission allows for the determination of the electronic band structure in $E(k_{||})$ space.

2.2.2 Surface states and bulk states

The electronic states of solids can be classified into three categories according to the spatial extent of their wave functions, namely (a) bulk state, (b) surface state, and (c) surface resonance state. Bulk states are the three-dimensional Bloch state whose wave function is appreciable throughout the crystal and is characterized by $k_{||}$ (k_x, k_y) and $k_\perp$ (k_z) and other quantum numbers such as spin. On the other hand the surface state is localized near the surface of the crystal and its wave function decays exponentially into the bulk.

Thus, for surface state, $k_\perp$ is not a good quantum number and hence the state is characterized solely by $k_{||}$ and their electronic band structure is completely determined in $E(k_{||})$ space within the two-dimensional SBZ. Therefore, ARPES can be used to extract the entire band structure of surface states at a fixed photon energy. In contrast, since bulk state resides in the three-dimensional BZ, the indeterminacy of $k_\perp$ can pose a problem in identifying the initial state in BZ. However, if we assume that the photoemission final state is that of free electron, then with the reasonable estimate of the inner potential V_0, the $k_\perp$ of the initial state can be roughly calculated from

$$E_{kin} + V_0 = \frac{k_{\parallel}^2 + k_{\perp}^2}{2m} . \tag{2.27}$$

Thus, under certain reasonable approximations, ARPES allows us to extract the surface as well as bulk electronic band structures of materials.

2.2.3 Selection rules

As in equation (2.21), the photoemission transition rate is weighted with the single-electron matrix element $\left|\langle \phi_f | \Delta | \phi_i \rangle\right|^2$. Although the direct calculations of these matrix elements require considerable computational effort, the symmetry of the problem can be used to predict when the matrix element vanishes (i.e., for what initial/final states the transition is forbidden). The selection rules for photoemission (and, in fact, any other transition) can be derived from the symmetries of the initial state, final state, and photoemission perturbation operator (or appropriate operator pertinent to the problem). Since the initial state is a Bloch state in the crystal, its symmetry is determined by the symmetry of the crystal. For example, if we are probing the surface state on (110) surface of *fcc* crystal at $k_{||} = 0$ (i.e., the state at $\bar{\Gamma}$ in the surface Brillouin zone), the symmetry of the crystal surface is described by the group of C_{2v} (Schoenflie's notation), which consists of the following four symmetry operations: identity operation (E), π rotation (C_2), and reflections about two axes (σ_v, σ_v'). Although all the four operations above leave the crystal structure invariant, they generally do not leave the wave functions invariant. Therefore, the wave function of the any electronic state can be classified according to *how the wave function transforms* under each of the operations in the pertinent group (the four operations of C_{2v} group in the case of *fcc*(110) surface state). For the specific case of C_{2v} group, there are four distinct categories: A_1, A_2, B_1 and B_2, and thus any surface state at $\bar{\Gamma}$ on *fcc*(110) can be classified into one of these categories (called *irreducible representations* in the language of group theory) according to their transformation properties within the pertinent group. The irreducible representation is nothing but the *set of matrices* describing the transformation properties of the wave function.

In order to obtain the symmetry property of the photoemission perturbation operator Δ, it is customary to employ the dipole approximation. Then, it can be seen that Δ transforms as the vector parallel to the vector potential A. As for the symmetry property of final state, it is believed to be always the fully symmetric irreducible representation (i.e., the photoemission final state is invariant under all the symmetry operations that leave the system invariant). Now, given the transformation properties (i.e., the irreducible representations) for each of the ingredients in photoemission matrix element, the dipole selection rule (the decorative word "dipole" comes from the dipole approximation made here) can be derived. Taking the triple tensor product of irreducible representations to obtain the transformation property of $\langle \phi_f | \Delta | \phi_i \rangle$ will generally yield a 'linear combination' of irreducible representations (or *reducible* representation). However, since the matrix element is a (complex) number, it is evident that it must transform as a number (i.e., invariant under all the symmetry operations). Thus, the general statement can be made on the selection rule of matrix element as, *the matrix element must vanish unless it contains the fully symmetric irreducible representation, which gives the transformation property of scalar number*.

It might seem, at this point, that the selection rule is merely an unwelcome restriction on the photoemission experiment because certain states will be *invisible* due to the symmetry restriction. However, proper understanding and utilization of the photoemission selection rules, in fact, can provide us with very useful information difficult to obtain otherwise. For the photoemission matrix element, since the transformation property of final state is fixed, by controlling the polarization direction of incident light (i.e., the transformation property of Δ), it is possible to 'hide and show' the states with certain symmetry. Observing at which light polarizations the certain state appear/disappear, we can obtain the information on the symmetry of the initial state. Furthermore, when probing the materials with complex electronic structure, it is often desirable to selectively view the electronic states, which allows us to avoid artificial overlap of the spectral intensities from different states with different symmetries. Thus, the photoemission selection rule is a powerful tool, which expands the capabilities of photoemission spectroscopy.

2.2.4 Fermi surface mapping

Another important utilization of photoemission spectroscopy is its capability to directly measure the Fermi surface of solid. This is achieved by measuring the spectral intensity within the small finite energy window about the Fermi level in small increments of emission angle (θ, φ). Since the electrons at the Fermi surface play an important role, for example, in transport properties, structural stability, as well as formation of charge density waves, an ability to obtain the Fermi surface mapping is one of most attracting features of ARPES.

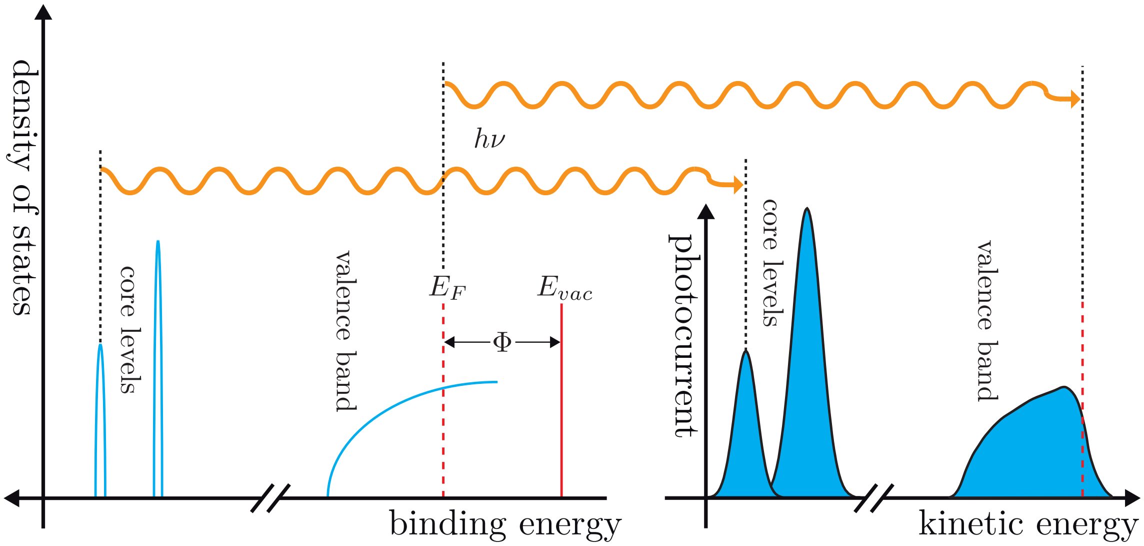

Figure 2.2: Schematic representation of electronic states in a solid (left) and the corresponding photoemission spectrum (right). The photon with energy $h\nu$ impinges on the sample and excites the electrons. The electrons excited above the vacuum level (E_{vac}) will gain finite kinetic energy. Note that the photoemission peaks gain the finite width due to the photoemission process (see text). Figure provided in courtesy of Dr. Eike F. Schwier.

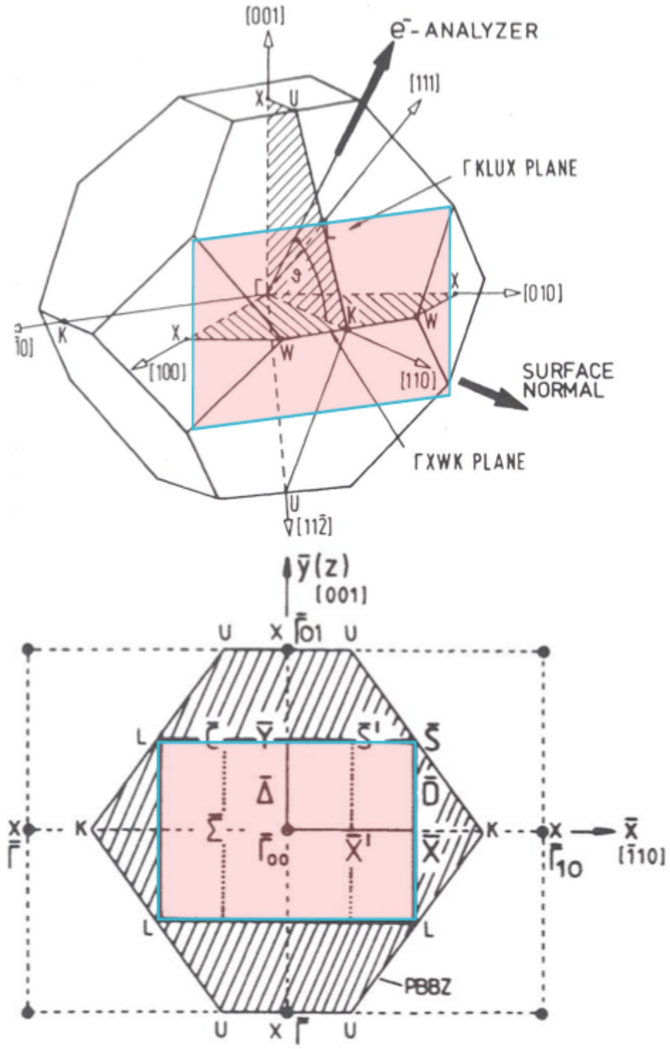

Figure 2.3: Top: The bulk Brillouin zone of *fcc* crystal with the surface Brillouin zone of (110) surface (red rectangle) overlaid. The bulk electronic states in the vertical hatched slice can be observed by varying θ while fixing $\varphi = 0$, and those in the horizontal hatched slice can be observe by varying φ while fixing $\theta = 0$. Bottom: The (110) surface Brillouin zone and the projected bulk Brillouin zone viewed along the <110> axis.

References

[1] S. Hufner, *Photoelectron Spectroscopy* (Springer, 2003), ISBN 3540418024.

[2] H. Bruus and K. Flensberg, *Many-Body Quantum Theory in Condensed Matter Physics* (Oxford University Press, 2004), ISBN 9780198566335.

[3] T. Giamarchi, A. Lucci and C. Berthod, *Introduction to Many Body physics – Lecture notes* (2008-2009).

Chapter 3
Low energy electron diffraction

3.1 Reciprocal lattice and diffraction

Since the states of electrons in solid are labeled by their crystal momentum *k* (i.e., *k* is one of the good quantum numbers), it is important to understand the structure of the crystal in the reciprocal space (or *k*-space). When the real lattice (or direct lattice) is specified by the set of vectors *R*, its *reciprocal lattice* is defined as the set of all the wave vectors *G* such that

$$e^{iG\cdot R}=1\,. \tag{3.1}$$

In principle, the reciprocal lattice can be directly observed by diffraction measurements. If *k* is the wave vector of incident wave and *k*' is the diffracted wave (here we assume the elastic scattering for which $|k| = |k'|$), it can be formally shown that the condition for the constructive interference is

$$\left(k-k'\right)\cdot R=2\pi n \tag{3.2}$$

or equivalently

$$e^{i(k-k')\cdot R}=1\,, \tag{3.3}$$

which gives, when compared to (3.1),

$$G=k-k'\,. \tag{3.4}$$

This is called the Laue condition (c.f., [1]), and thus by measuring the *k*' (the diffracted beam) for which the diffraction intensity has maxima, the reciprocal lattice vectors *G* can be determined. Figure 3.1 shows the visualization of the Laue condition, called the Ewald construction. In reciprocal space, if we draw the sphere of radius $|k| = |k'|$ (called the

Ewald sphere), then the diffraction peaks will be observed for the outgoing wave vector *k*' that connect the reciprocal lattice point *on* the sphere and the center of the sphere (see Figure 3.1). There are many types of waves (beams) that can be utilized in the diffraction experiments, such as X-ray, neutrons, and electrons. Each of the beam sources has its advantages and disadvantages in characterizing the crystal structures in real and reciprocal spaces. Here, we focus on the low energy electrons as the probing means to identify the crystal structures at the surfaces.

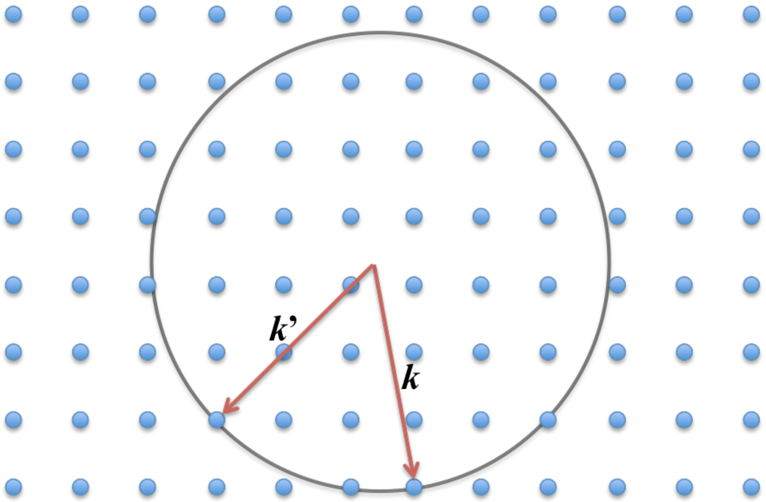

Figure 3.1: The Ewald construction in reciprocal space. Given the Ewald sphere, the diffraction peak will be observed for the outgoing wave vector *k*' that connects the center of the sphere and the reciprocal lattice point on the surface of the sphere.

3.2 LEED as a measure of surface structure

In order to probe the crystal structures near the surface (as opposed to the bulk), it is critical to utilize the diffraction technique that is surface-sensitive, and not obscured by the bulk. Low energy electron diffraction (LEED) utilizes the incident electrons of the kinetic energy between 30-300 eV. Within this range of energy the electron's mean free path is <10 Å [2], comparable to the lattice constant of most crystals. Although the mean free path depends on the structure and the nature of the crystals, it has been shown experimentally that such dependence is rather small [3]. Thus, LEED is an ideal experimental technique to identify the surface structure of the crystals. Since the probing depth of LEED is limited to the topmost layer (or at most a few layers from the surface), the Laue condition for the surface-parallel direction dictates the diffraction condition, namely,

$$G_{\parallel} = k_{\parallel} - k'_{\parallel}, \tag{3.5}$$

where $k_{\parallel}$ ($k_{\parallel}$') denote the incident (outgoing) wave vector parallel to the crystal surface. In visualizing the Ewald construction for LEED, which reflects only the structural information within the limited slab thickness, we may imagine increasing the inter-slab distance in the direction perpendicular to the surface. In the limit as this inter-slab distance tends to infinity, the corresponding reciprocal lattice points becomes more and more densely spaced in the surface-normal direction and eventually form the reciprocal lattice "rods" lying parallel to the surface-normal. Therefore, in visualizing the diffraction condition for LEED, the Ewald sphere should be constructed as described above but the diffraction peak now appears for outgoing wave vector k' that connects the center of the Ewald sphere with any point on the reciprocal lattice rods, as illustrated in Figure 3.2. Of course, this visualization is fully equivalent to the equation (3.5).

LEED has numerous applications in characterizing the surface structures and surface phenomena (e.g., structural phase transitions etc.). In the present study, it is utilized to verify the surface cleanness (characterized by the sharpness of the LEED spot), adsorbate structures (as will be discussed), and to estimate the surface Debye temperature (sec. 3.3). Due to the surface-sensitivity of LEED, when foreign atoms adsorb on the crystal surface, the LEED pattern can be affected as these atoms also serve as scattering centers in the diffraction. In particular if the adsorbed atoms form periodic structure, they give rise to extra diffraction spots. As an example, the LEED patterns for Mo(112) is shown in Figure 3.3a. When the certain number of oxygen atoms are adsorbed on Mo(112) surface, the LEED pattern shows additional spots midway between the original Mo-induced spots along $\langle 11\bar{1}\rangle$ direction (indicated by thick arrows in Figure 3.3b). These spots are called superstructure spots and signify the formation of periodic structure on the Mo(112) surface. Since the reciprocal lattice points (i.e., LEED spots) reflect the periodicity of the structure, these superstructure spots which have half of the periodicity of Mo(112) spots in the $\langle 11\bar{1}\rangle$ direction and the same periodicity in the $\langle 1\bar{1}0\rangle$ direction means that the oxygen atoms formed the structure with twice the periodicity in $\langle 11\bar{1}\rangle$ direction and the same periodicity in the $\langle 1\bar{1}0\rangle$ direction (relative to the Mo(112) substrate). Such overlayer structure is conventionally called (1x2) structure, where the first number (1) indicates the periodicity in $\langle 11\bar{1}\rangle$ direction and the second number (2) indicates the periodicity in the $\langle 1\bar{1}0\rangle$ direction. Although the LEED patterns tell us the periodicity of the overlayer structure, it does not uniquely determine the structure itself. For this reason, other methods such as Auger electron spectroscopy (AES) etc. should be utilized to determine the amount of adorbate atoms in combination with LEED to fully determine the structure formed by the adsorbate atoms.

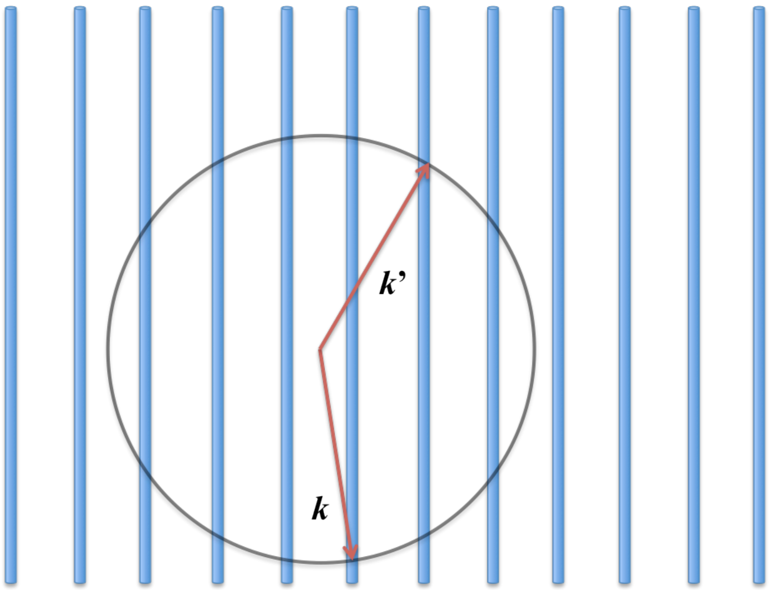

Figure 3.2: The Ewald construction for LEED. The diffraction peak is observed for any outgoing wave vector *k*' that connects the center of the sphere and any point on the reciprocal lattice rod.

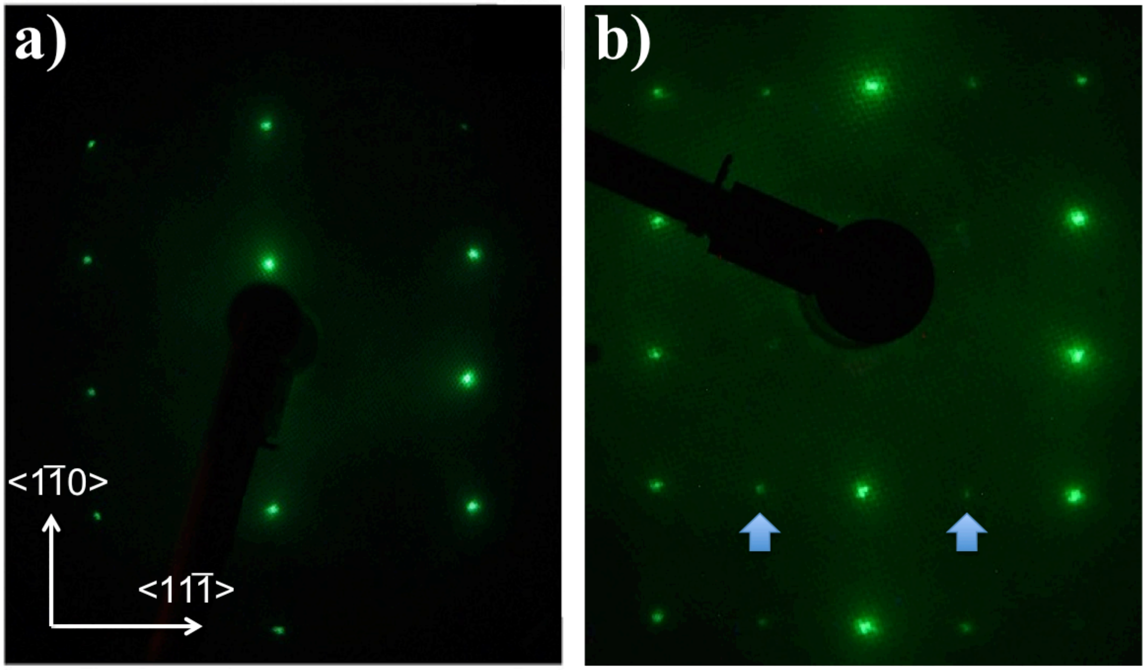

Figure 3.3: (a) The LEED patterns for clean Mo(112). The crystallographic directions parallel to the surface are indicated with thin arrows. (b) The LEED pattern for O/Mo(112) at the nominal coverage of 0.5 monolayer, which shows (1x2) superstructure spots (two of them are indicated by thick arrows).

3.3 Surface Debye temperature

LEED is not only useful for obtaining the static properties of surface such as the lattice period, but also for determining its dynamic properties. In particular, in the present study, LEED is utilized to estimate the surface Debye temperature of Mo(112), which can roughly be obtained from the temperature dependence of the LEED spot intensities, as will be shown. The scattering of electrons from massive bodies (ions) can be described by the scattering amplitude

$$A(k',k) \propto \sum_i e^{-ik'\cdot r_i} t_i(k',k) e^{ik\cdot r_i} \quad , \tag{3.6}$$

where r_i is position of *i*-th ion and t_i(k', k) is called *t*-matrix which describes the details of the scattering process from *i*-th ion. The complex exponential on the left (right) of *t*-matrix describes the outgoing (incoming) wave with wave vector *k*' (*k*). For the purpose of our discussion, the detailed scattering mechanism is irrelevant and we assume that *t*-matrix does not depend on positions and the detailed properties of *i*-th ion and regard it as dependent only upon *k* and *k*'. In a naïve picture, we may assume for any given (*k*', *k*), the *t*-matrix is chosen to be an appropriate constant *t*(*k*', *k*) that best reproduces the scattering amplitude *A* in (3.6). If we now let ions move around its equilibrium position, the instantaneous position of *i*-th ion r_i is defined as

$$r_i = R_i + \Delta r_i \quad , \tag{3.7}$$

where R_i is the equilibrium position and Δr_i is the excursion from R_i. Then the scattering intensity is

$$I(k',k) \propto \left|A(k',k)\right|^2 = \left|t(k',k)\right|^2 \sum_{ij} e^{i\Delta k\cdot\left(R_i - R_j\right)} e^{i\Delta k\cdot\left(\Delta r_i - \Delta r_j\right)} \ . \tag{3.8}$$

Now, since the time-scale of LEED measurement is much longer than that of the ionic motion in the crystal, the LEED spot intensity must be proportional to the time-averaged scattering intensity $\langle I(k',k)\rangle$. By noting that the last exponential is the only term that depends on time, we have

$$\langle I(k',k)\rangle \propto |t(k',k)|^2 \sum_{ij} e^{i\Delta k\cdot(R_i-R_j)} \left\langle e^{i\Delta k\cdot(\Delta r_i-\Delta r_j)}\right\rangle \quad . \tag{3.9}$$

If we now assume that the correlation between the motions of any two ions are weak or negligible (for justification, refer e.g., to sec. 5.9 on [2]), then

$$\left\langle e^{i\Delta k\cdot(\Delta r_i-\Delta r_j)}\right\rangle \approx \left\langle e^{i\Delta k\cdot\Delta r_i}\right\rangle\left\langle e^{i\Delta k\cdot\Delta r_j}\right\rangle . \tag{3.10}$$

If we further assume that the ions' displacements are small, it can be expanded and approximated as

$$\left\langle e^{i\Delta k\cdot\Delta r_i}\right\rangle \approx e^{-\frac{1}{2}\left\langle(\Delta k\cdot\Delta r_i)^2\right\rangle} \quad . \tag{3.11}$$

Note that the power series expansions of both sides in (3.11) are identical up to 2nd order. Therefore, the time-averaged scattering intensity (3.9) can be rewritten as

$$\langle I\rangle \propto \sum_{ij} e^{i\Delta k\cdot(R_i-R_j)} e^{-\frac{1}{2}\left\langle(\Delta k\cdot\Delta r_i)^2\right\rangle} e^{-\frac{1}{2}\left\langle(\Delta k\cdot\Delta r_j)^2\right\rangle} = e^{-\left\langle(\Delta k\cdot\Delta r)^2\right\rangle} \sum_{ij} e^{i\Delta k\cdot(R_i-R_j)} \quad . \tag{3.12}$$

Evidently, the Δr is the only temperature-dependent parameter. Thus, we expect the temperature-dependence of intensity I of any particular LEED spot to be described as

$$I = I_0 e^{-2W} \quad . \tag{3.13}$$

where I_0 is the LEED spot intensity at the fixed reference temperature and W is called Debye-Waller factor:

$$W = \frac{1}{2}\left\langle (\Delta k \cdot \Delta r)^2 \right\rangle . \tag{3.14}$$

This means that the LEED spot intensity is reduced exponentially by the mean-square displacement of ions. In order to extract the explicit temperature-dependence of W, the Debye model of phonons is conventionally employed, as it gives analytical solution. Using the Debye model of phonons, the Debye-Waller factor can be written, in the high temperature limit ($T > \Theta_D$), as

$$W = \frac{3}{2}\frac{\hbar^2 \left(\Delta k\right)^2 T}{m k_B \Theta_D} \tag{3.15}$$

in 3-dimension, accounting for three polarizations of phonons, where m is the ion mass and Θ_D is the Debye temperature. Therefore, under these assumptions, the LEED spot intensity decreases exponentially with increasing temperature and the decay factor directly relates to the Debye temperature of the material. Note that Debye temperature can be considered as the temperature scale for which the appreciable number of phonons are excited, or roughly speaking, the 'stiffness' of the lattice. This model is used in Chapter 9 to extract the Debye temperature of Au/Mo(112) overlayer from the observed exponential temperature-dependence of the LEED spot intensities.

References

[1] N. W. Ashcroft and D. N. Mermin, *Solid State Physics* (Brooks Cole, 1976), ISBN 9780030839931.

[2] L.J. Clarke, *Surface crystallography* (John Wiley & Sons, 1985), ISBN 0471905135.

[3] S. Hufner, *Photoelectron Spectroscopy* (Springer, 2003), ISBN 3540418024, Chapter 1 and references cited therein.

Chapter 4
Sample preparations

4.1 Cleaning of Mo(112)

In order to analyze the electronic structure and many-body interactions at the surface of Mo(112) and the interface of Au/Mo(112), the preparation of the atomically clean sample surface is critical. The Mo(112) sample with 99.99% purity with dimensions 7mm x 5mm x 1.5 mm was purchased from Princeton Scientific. It is known that Mo sample is contaminated mostly with carbon (C) and oxygen (O) at the surface and dissolved C within its bulk. Removal of these impurities requires heating of the sample up to ~ 1800 °C [1-6]. Thus, in order to achieve the high-temperature, the method of high-voltage electron bombardment is employed. The preparation of clean Mo(112) sample is performed in the sample-preparation chamber at ultra-high vacuum (UHV) of base pressure of ~10^{-10} torr. The apparatuses for the electron bombardment consist of a sample holder made of Mo attached to the high-voltage supply, and the filament made of tungsten (W) which can be resistively heated. The amount of contaminations including C and O are monitored by Auger electron spectroscopy (AES) and the surface structural order is monitored by LEED.

At the time of annealing and flashing of the Mo sample, the high-voltage between 0.9 – 1.5 kV is applied to the Mo sample and the movable filament, located several millimeters from the backside (unpolished side) of the Mo sample, is heated to liberate the thermal electrons. The thermally emitted electrons are accelerated towards the Mo sample at the high-voltage, releasing the kinetic energy and thereby heating the Mo sample (bombardment). The temperature of the sample is continuously monitored by infrared pyrometer. After degassing the sample, the UHV chamber is filled with oxygen atmosphere with the partial pressure of 10^{-6} – 10^{-8} torr and annealed at 1300 - 1450° C for at least 8 hours. This process removes most of C from the surface as well as some from the bulk. Although the prolonged annealing in oxygen atmosphere burns off C at the surface, it inevitably leaves oxygen at the surface. Thus, it is followed by flashing at ~1800 °C or higher, which eliminates the residual oxygen. Unfortunately, at the temperature of the flashing to eliminate oxygen, some amount of dissolved C within the bulk of the Mo(112) sample comes to the surface due to surface segregation. Therefore, in order to eliminate both C and O from the Mo(112) sample, the process of repeated annealing (in oxygen atmosphere) and flashing is continued until the amount of C arising to the surface upon flashing is negligible (undetectable in AES). In conjunction with AES to confirm the removal of most contaminations, LEED is used to confirm the sharp spots and hence the surface structural order as shown in Figure 4.1

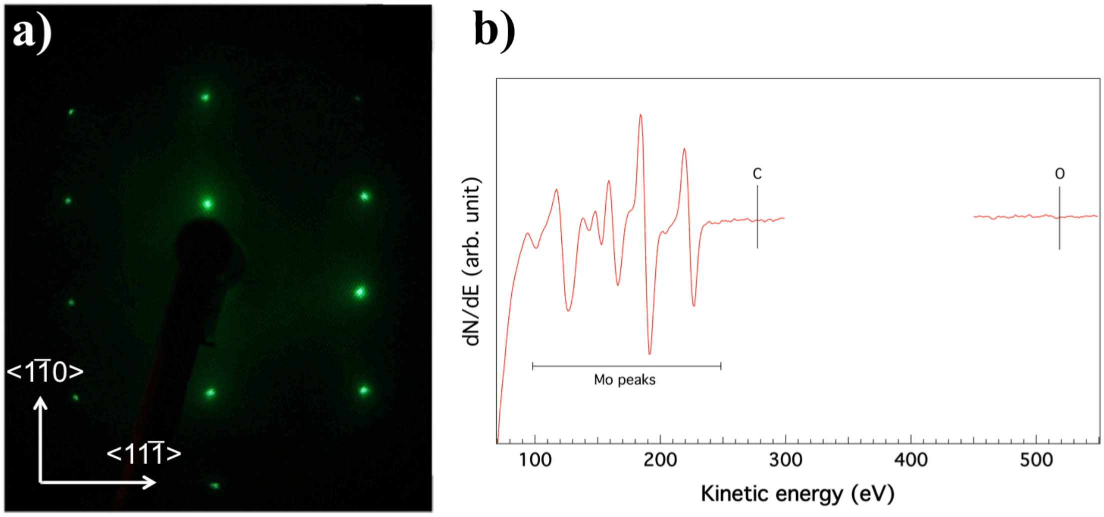

Figure 4.1: Characterization of clean Mo(112) surface. (a) Sharp spots of LEED characterized the periodic structural order of the sample and (b) absence of most pronounced peaks of C and O in AES characterizes the adsorbate-free clean surface.

4.2 Deposition of thin film Au

Deposition of Au was performed by heating the spherical Au source (diameter ~2 mm) below its melting point in front of the Mo(112) sample (physical vapor deposition). Since with a slow growth rate, Au is known to grow layer-by-layer on Mo(112) surface [6], the vapor pressure of Au and the distance between the Au source and the sample were adjusted so as to obtain sufficiently slow Au deposition rate as determined by the peak ratio of Mo and Au in AES spectra. Given the constant, slow deposition rate, the gradual growth of Au film in the submonolayer regime was monitored by observing the expected linear relation between the adsorbate coverage and Au peak intensity in AES [7] as well as the gradual formation of Au-derived superstructure spots in LEED. Near the completion of 1 ML coverage, the LEED was utilized to monitor and confirm the formation of 1 ML coverage, which is expected to show the sharp (1x1) structure following the disappearance of superstructure spots.

Above 1 ML coverage, three distinct Au overlayer structures are observed; (2x1), (3x1), and (4x1) as shown in Figure 4.2. For each of these structures, the AES was utilized to estimate the Au coverage and the corresponding LEED patterns were utilized to characterize the overlayer periodicity and the structures at the room temperature (300 K).

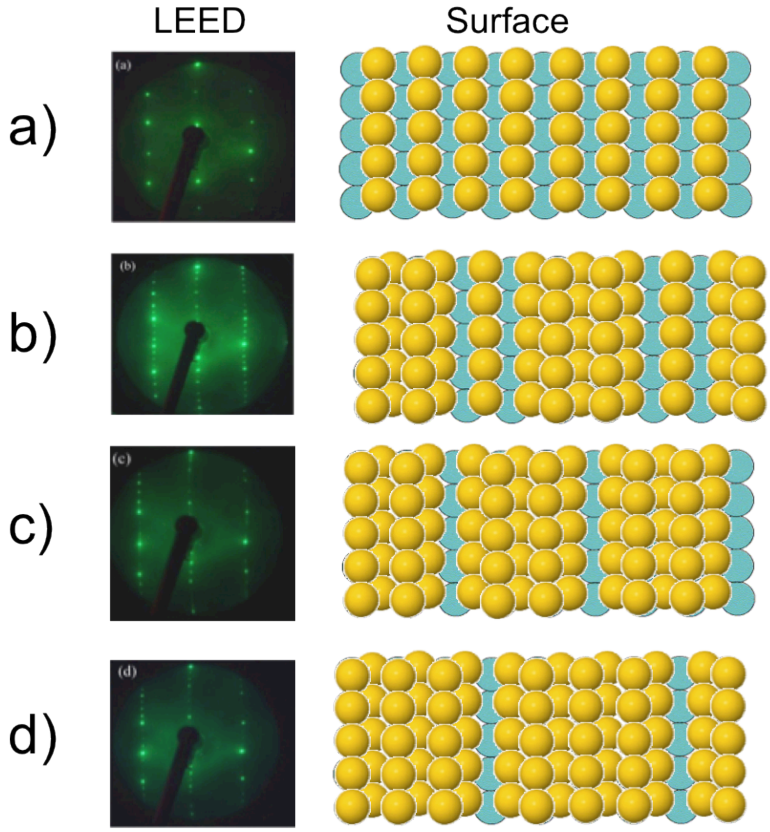

Figure 4.2: The surface structures and corresponding LEED patterns of Au/Mo(112) at the coverage of (a) 1 ML (1x1), (b) 1.5 ML (4x1), (c) 1.66 ML (3x1) and (d) 1.75 ML (4x1). The LEED images are taken at room temperature.

References

[1] K. Fukutani, H. Hayashi, I. N. Yakovkin, T. R. Paudel, T. Habuchi, D. Hirayama, J. Jiang, H. Iwasawa, K. Shimada, N. Wu, E. Y. Tsymbal, Y. B. Losovyj, and P. A. Dowben, *Phys. Rev.* B **85**, 155435 (2012).

[2] T. McAvoy, J. Zhang, C. Waldfried, D. McIlroy, P. Dowben, O. Zeybek, T. Bertrams, and S. Barrett, *Eur. Phys. J.* B **14**, 747 (2000).

[3] I. Yakovkin, J. Zhang, and P. Dowben, *Phys. Rev.* B **63**, 115408 (2001).

[4] H. K. Jeong, T. Komesu, I. N. Yakovkin, and P. Dowben, *Surface Science Letters* **494**, L773 (2001).

[5] N. Wu, Y. B. Losovyj, Z. Yu, R. F. Sabirianov, W. N. Mei, N. Lozova, J. A. Colón Santana, and P. A. Dowben, *J. Phys.: Condens. Matter* **21**, 474222 (2009).

[6] K. Fukutani, Y. B. Losovyj, N. Lozova, I. N. Yakovkin, N. Wu, and P. A. Dowben, *Journal of Electron Spectroscopy and Related Phenomena* **184**, 318 (2011).

[7] T. Gallon and J. Matthew, *Review of Physics in Technology* **3**, 31 (1972).

Chapter 5
Analysis of many-body interactions at metallic surfaces

5.1 Quasiparticles and Fermi liquid theory

It was described in Chapter 2 that photoemission spectroscopy measures the single-particle spectral function. The basic argument was that when a photon impinges on the surface of solid, it creates a hole in the occupied state and an electron in the unoccupied state (above the vacuum level). Such process is called single-particle excitation. If the many-body system of the solid was non-interacting (e.g. the Hamiltonian is $H = \sum_k E(k) c_k^+ c_{\boldsymbol{k}}$), then the Green's function can be easily computed as

$$\begin{aligned} G(k,t) &= -i\theta(t)\left\langle \left[c_{k,t}, c_{k,0}^+ \right]_+ \right\rangle \\ &= -i\theta(t) e^{-iE(k)t} \end{aligned} , \tag{5.1}$$

which, upon Fourier transform, gives

$$\begin{aligned} G(k,\omega) &= \int e^{i(\omega+i\delta)t} G(k,t) dt \\ &= \frac{1}{\omega - E(k) + i\delta} \end{aligned} , \tag{5.2}$$

where δ is a positive infinitesimal. Then the spectral function for the non-interacting system is

$$A(k,\omega) = -\frac{1}{\pi} \operatorname{Im} G(k,\omega) = \delta(\omega - E(k)), \tag{5.3}$$

which is nonzero only at the excitation energy given by the non-interacting electronic band dispersion relation $E(k)$. Above delta function for each k can be thought of as representing electrons (real particles) localized completely in the $E(k)$ space. This is of course expected, because in the absence of interactions, the electrons will remain in their eigenstates forever and their states are completely well defined. However, in reality, the many particles (not only electrons) in solids interact with one another. In such general and more *correct* case, the Hamiltonian governing the equation of motion for creation and annihilation operators of electrons is no longer bilinear, and the exact calculation of Green's function as in (5.2) is not possible. Nevertheless, we have shown in chapter 2 that general *form* of single-particle Green's function as well as the corresponding spectral function can be derived. The general form of single-particle spectral function is

$$A(\omega,k;T) = -\frac{1}{\pi}\frac{\Sigma_I(\omega,k;T)}{\left[\omega - E(k) - \Sigma_R(\omega,k;T)\right]^2 + \Sigma_I(\omega,k;T)^2} \,. \tag{5.4}$$

Roughly speaking, we converted the problem of calculating the Green's function to the problem of calculating the self-energy $\Sigma(k, \omega)$. In other words, all the many-body corrections to the simple delta function are now 'stuffed' into the self-energy. Unfortunately, full computation of self-energy is as difficult as the calculation of Green's function itself. So, it may seem that we achieved very little. However, the beauty is that since the spectral function, in principle, can be directly observed in ARPES, casting the many-body problem of realistic solid into the determination of self-energy is a convenient conversion from the experimental point of view. It can be seen that the spectral function is a Lorentizan-like function with the peak given by

$$\omega - E(k) - \Sigma_R(\omega,k;T) = 0 \,, \tag{5.5}$$

and the width (FWHM) given by $2\Sigma_I(\omega,k;T)$.

Although the spectral function is still a peaked function, it is no longer identified as real particle (electron etc.), but rather as quasiparticle; it has the renormalized dispersion relation and the finite spread in the $E(k)$ space.

The effects of the many-body interactions in solid are reflected in the self-energy, which, in turn, controls the shape of the spectral function. Thus, it is important to understand the physical meaning of the self-energy. First, in order to understand the imaginary part of the self-energy, we consider the following Green's function.

$$G(k,t) = -i\theta(t)e^{-iE(k)t}e^{-t/\tau}, \tag{5.6}$$

which is nothing but the free-particle Green's function with the decay parameter $e^{-t/\tau}$. The single-particle Green's function represents the probability amplitude that if the particle is inserted into a certain state of the system, the system will be found in the same state at later time t. Thus, the decaying exponential will decrease such probability as a function of time, which is of course due to the interactions within the system. As the extra particle enters the system, the interaction with all the other particles will scatter this extra particle out of the 'initial' state within the given time scale τ. The corresponding spectral function can be written as

$$A(k,\omega) = \frac{1/\tau}{\left[\omega - E(k)\right]^2 + (1/\tau)^2}\ , \tag{5.7}$$

in which case the self-energy can be identified as

$$\Sigma_R = 0,\ \Sigma_I = 1/\tau\ . \tag{5.8}$$

Thus, the imaginary part is directly related to the temporal decay of the single-particle excitation. Such decay can be considered as the *lifetime* of the quasiparticle. On the other hand, the real part of self-energy is seen to alter the single particle excitation energy. In the absence of interaction the excitation energy ω is given by

$$\omega = E(k) \quad . \tag{5.9}$$

But, when the interaction is turned on and the real part is finite, the new dispersion relation is

$$\omega = E(k) + \Sigma_R(\omega,k) \quad . \tag{5.10}$$

Thus, the interaction can *dress* the real (or bare) particle and 'changes' its dispersion relation. In order to see the consequence of this change in the dispersion relation, we note that dispersion relation (whether it is the bare or the modified dispersion relation) can be expanded in linear order in k sufficiently close to the Fermi level. Therefore, the bare dispersion $E(k)$ and the modified dispersion $E(k) + \Sigma_R(\omega, k)$ can be written as

$$\begin{gathered} E(k) \approx \frac{k_F}{m}\left(k - k_F\right) \\ E(k) + \Sigma_R(\omega,k) \approx \frac{k_F}{m^*}\left(k - k_F\right) \end{gathered} \tag{5.11}$$

near the Fermi level, where m is the band mass of the particle and m^* is the *renormalized* mass of the particle, which accounts for the change in the slope of the dispersion due to the many-body interactions. The band mass m and renormalized mass m^* can be related by writing

$$\frac{d\omega}{dk} = \frac{d}{dk}\left[E(k) + \Sigma_R(\omega,k)\right] = \frac{dE(k)}{dk} + \frac{\partial\Sigma_R(k,\omega)}{\partial k} + \frac{\partial\Sigma_R(k,\omega)}{\partial\omega}\frac{d\omega}{dk} \quad . \tag{5.12}$$

Since $d\omega/dk = k_F/m^*$ and $dE/dk = k_F/m$, then we have

$$m^* = \left(\frac{1 - \dfrac{\partial\Sigma_R}{\partial\omega}}{1 + \dfrac{m}{k_F}\dfrac{\partial\Sigma_R}{\partial k}} \right) m \quad . \tag{5.13}$$

Thus, the real part of self-energy gives rise to the renormalization of the effective mass of the particle. Although the real and the imaginary part of self-energy have quite distinct physical interpretations, since the self-energy is a causal complex function, they must be related by the Kramers-Kronig relation

$$\Sigma_R(\omega,k)=\frac{1}{\pi}P\int_{-\infty}^{\infty}\frac{\Sigma_I(\omega',k)}{\omega'-\omega}d\omega\quad, \tag{5.14}$$

where P denotes the Cauchy principal value.

In particular, for metals, the majority of the contributions to the self-energy come from electron-phonon coupling ($\Sigma^{(e\text{-}p)}$), electron-electron coupling ($\Sigma^{(e\text{-}e)}$), and electron-impurity coupling ($\Sigma^{(e\text{-}i)}$). The main focus on the current study will be on these three. Fortunately, the self-energies are additive, provided that the interaction mechanisms are independent, namely

$$\Sigma=\Sigma^{(e-p)}+\Sigma^{(e-e)}+\Sigma^{(e-i)}\,. \tag{5.15}$$

5.2 Characterization of many-body interactions

The central equation in the analysis of electron-phonon coupling as well as other many-body interactions is, again, the quasiparticle spectral function:

$$A(\omega,k;T)=-\frac{1}{\pi}\frac{\Sigma_I(\omega,k;T)}{\left[\omega-E(k)-\Sigma_R(\omega,k;T)\right]^2+\Sigma_I(\omega,k;T)^2}\,. \tag{5.4}$$

Note that Σ_I is an intrinsically negative quantity. From the experimental perspective, starting point is the observation of $A(\omega, k)$ by ARPES and the goal is to find the self-energy associated with each interaction mechanism. By finding the bare particle dispersion relation $E(k)$, it is possible to obtain the complex self-energy $\Sigma(\omega, k)$ from the observed spectral function, which characterizes the many-body interactions of the material in question. Of course, as (5.4) is a general expression, the experimentally extracted self-energy is a 'mixture' of electron-phonon coupling ($\Sigma^{(e\text{-}p)}$), electron-electron coupling ($\Sigma^{(e\text{-}e)}$), and electron-impurity coupling ($\Sigma^{(e\text{-}i)}$). In identifying each of the three contributions in the experimentally extracted self-energy, the theoretically expected general features of each of $\Sigma^{(e\text{-}p)}$, $\Sigma^{(e\text{-}e)}$ and $\Sigma^{(e\text{-}i)}$ as well as the Kramers-Kronig relation (5.14) can be utilized. Besides the self-energy Σ, another quantity of interest is mass enhancement parameter at the Fermi level $\lambda(k = k_F;\, T)$, which is defined by the equation (5.13) assuming $\partial\Sigma/\partial k = 0$

$$m^* = \left[1 + \lambda(k_F;T)\right]m, \tag{5.16}$$

where

$$\lambda(k_F;T) = -\left.\frac{\partial\Sigma_R(\omega,k_F;T)}{\partial\omega}\right|_{\omega=0}, \tag{5.17}$$

where m and m^* are the 'bare' (or unrenormalized) band mass and the dressed (or renormalized) mass of the electron respectively.

Experimentally, there are two physically equivalent methods to extract the self-energy from the observed spectral function. One method is to slice the ARPES spectrum at constant wavenumber k, which gives the sequence of energy distribution curves (EDCs) for each k. The other method is to slice the ARPES spectrum at constant energy, which gives the sequence of momentum distribution curves (MDCs). Although, in principle, both methods are equivalent, it is usually more advantageous to employ the MDC method. To see this point, it is important to note that a spectral function is not precisely Lorentzian either in EDC or MDC due to the energy and momentum dependence of Σ as well as the functional dependence of *E*(*k*). However, the momentum dependence of Σ is generally much smaller than the energy dependence and, in fact, nearly negligible in the vicinity of single band (where the spectral function is appreciable). Furthermore, if we make the approximation $E(k) = vk$ (i.e., linear dispersion), justified sufficiently close to E_F (where v is the group velocity), then the MDC lineshape is in fact Lorentizan with the peak position (k_{peak}) and FWHM (Γ) given by

$$\begin{aligned} k_{peak}(\omega) &= \frac{1}{v}\left[\omega - \Sigma_R(\omega)\right] \\ \Gamma(\omega) &= -\frac{2}{v}\Sigma_I(\omega) \end{aligned} \tag{5.18}$$

for each MDC with fixed energy ω. Thus, MDC slices are generally expected to fit Lorentzian lineshape better than the EDC slices in the presence of many-body interaction, which allows for more accurate analysis of the spectral function and hence the associated self-energy. For this reason, in the present study, the MDC methods are employed to extract the peak position and the width of the lineshape, which directly relates to the real and imaginary part of Σ as in (5.18). In order to correctly extract the self-energy contribution from each of the coupling (interaction) mechanisms, it is critical to understand the general features of self-energy associated with electron-phonon, electron-electron, and electron-impurity coupling.

Electron-phonon coupling is the interaction between the phonon modes with the electrons in which the electron exchanges its energy and momentum with phonons. In the phonon absorption process, certain phonon is annihilated and gives the energy and momentum to the electron, thereby scattering the electron out of the initial state. In the phonon emission process, the electron gives out certain amount of energy and momentum to create a phonon and gets scattered out of the initial state. Since the maximum excitation energy of phonon, characterized by Debye energy ω_D, is small ($\omega_D < 100$ meV), it is intuitive that any structures in the self-energy $\Sigma^{(e\text{-}p)}$ should be limited within this small range near the Fermi level. In principle, the self-energy $\Sigma^{(e\text{-}p)}$ can be calculated from so-called Eliashberg function $\alpha^2(\omega, k)F(\omega, k)$, where α^2 is the electron-phonon coupling function (related to the electron-phonon coupling matrix element) and F is the k-resolved phonon density of states (or phonon band structure). Roughly speaking, the Eliashberg function can be considered as the electron-phonon coupling matrix element summed over the entire Fermi surface, taking into account all the possible electronic scattering with the absorption/emission of a phonon. Once the Eliashberg function is known, it is straightforward to calculate the imaginary part of self-energy using the equation

$$\begin{aligned}\Sigma_I^{(e-p)}(\omega,k;T) = -\pi\int_0^\infty &\alpha^2(\omega',k)F(\omega',k)\\ &\times\left[1-f(\omega-\omega';T)+f(\omega+\omega';T)+2n(\omega';T)\right]d\omega' ,\end{aligned} \tag{5.19}$$

where f and n are Fermi and Bose distribution functions respectively, and the real part of self-energy can be obtained using the Kramers-Kronig relation (5.13). If the bare particle dispersion relation $E(k)$ is known, the spectral function can then be obtained. The difficulty is, of course, in calculating the Eliashberg function, which in most general case depends on energy ω as well as the wave vector k. The first-principle calculation of such ω- and k-dependent Eliashberg function is a formidable task and it is conventional to compute the Eliashberg function averaged over the entire Brillouin zone, so that it only depends on ω (i.e., $\alpha^2(\omega)F(\omega)$). Mass enhancement parameter λ at zero-temperature can be obtained as the inverse moment of the Eliashberg function in energy as

$$\lambda(T=0)=\int_0^\infty \frac{\alpha^2(\omega)F(\omega)}{\omega}d\omega \tag{5.20}$$

Electron-impurity coupling is the interaction between the electrons in the solids with the lattice defects or foreign atoms or anything that can break the perfect crystalinity (collectively called *impurities*). Such impurities can be though of as 'external' perturbation to the Hamiltonian of the perfect crystal and the electrons in the (unperturbed) eigenstates can be scattered out on some time scale (i.e., electrons acquire finite lifetime). It can be shown that if such impurities are randomly distributed in the crystal, electron-impurity coupling can give a rise to the imaginary part of self-energy that is independent of the excitation energy ω (i.e., $\Sigma^{(e\text{-}i)}{}_I$ = constant) (see for example ref. [1,2]). This means that, by virtue of the Kramers-Kronig relation, the real part of self-energy due to the electron-impurity coupling $\Sigma^{(e\text{-}i)}{}_R$ must vanish. Thus, $\Sigma^{(e\text{-}i)}$ is purely imaginary and only gives rise to the broadening of the spectral function, but does not alter the electronic dispersion relation.

Electron-electron coupling is the interaction between the electrons in which the mutual scattering in and out of the electronic states occur due to the Coulomb interactions. As in the case of electron-phonon coupling, the self-energy due to electron-electron coupling $\Sigma^{(e\text{-}e)}$ strongly depends on the topology of the Fermi surface. However, in the simple case of the three-dimensional spherical Fermi surface, the imaginary part of self-energy $\Sigma^{(e\text{-}e)}{}_I$ can be shown to be proportional to $[(\pi kT)^2 + \omega^2]$ and in the case of cylindrical Fermi surface, proportional to $\omega^2|\ln(\omega)|$ at zero-temperature, both near the Fermi level [3,4].

Therefore, when equipped with the above knowledge of the interactions mechanisms and the general features of self-energy to be expected from each type of interactions, it is possible to give, at least within the range of few adjustable free parameters, quantitative interpretations for the observed self-energy in terms of electron-phonon, electron-electron and electron-impurity couplings.

References

[1] G. D. Mahan, *Many-Particle Physics* (Plenum Publishing Corporation, 1990), ISBN 0306434237.

[2] H. Bruus and K. Flensberg, *Many-Body Quantum Theory in Condensed Matter Physics* (Oxford University Press, 2004), ISBN9780198566335.

[3] C. Hodges, H. Smith and J.W. Wilkins, *Phys. Rev.* B **4**, 302 (1971).

[4] D. Pines and P. Nozieres, *Theory of Quantum Liquids vol.1*, (Westview Press, 1994), ISBN 9780201407747.

Chapter 6
Electronic band structure of Mo(112)

6.1 Motivation

The surfaces of molybdenum are among the most studied in surface science, yet the detailed picture of their electronic structures as well as their many-body interactions remains incomplete. Surface states and surface resonance states in solids have a very long history [1-6] and the existence of surface resonance states was first verified for Mo(100) in 1977 [7,8], and subsequently characterized in more detail both theoretically and experimentally [9]. More recently, high-resolution angle-resolved photoemission spectroscopy (ARPES) made it possible to extract the detailed surface band structures as well as projected bulk band structures of solids, which has led to the elucidation of many-body interactions and their effects on the electronic structure of molybdenum [10,11]. In particular, theoretically predicted small yet characteristic band renormalization and quasi-particle lifetime effects due to electron-phonon coupling were first experimentally identified on Mo(110) in 1999, and were seen to be consistent, at least qualitatively, with the theoretical predictions [10].

The detailed characterization of the surface band structures near the Fermi level is particularly important in evaluating the effects of electron-phonon coupling in any material, for such effect is most pronounced within the Debye energy ω_D, which is about several tens of meV for transition metals. Electron-phonon coupling for the surfaces of molybdenum may provide insights into various kinds of surface structural phase transitions. In particular, the Mo(100) surface [12-19] is well known for the surface reconstructions driven by Peierls-like instability [20-24] that results from the surface charge density wave transition due to the nesting of the Fermi surfaces. The Mo(112) surface, on the other hand, has a very anisotropic in-plane band structure [25-29] with strongly surface-weighted density of states. It is important to note that Mo(112) exhibits a significant surface relaxation, in which interlayer distances show large variations (e.g. >15% contraction for the first two layers from the surface) from the bulk-truncated value [28,30,31].

The surface charge density of the Mo(112) substrate is a significant factor in the formation of well ordered quasi-one-dimensional structures such as seen for Li/Mo(112) [32,33], Sr/Mo(112) [34-37], Ba/Mo(112) [38] and Gd/Mo(112) [39], where overlayer systems have, in common, very large lateral distances between the adjacent atomic chains, favorable for the quasi-one-dimensionality [40]. Yet to understand the rich physics of these ordered quasi-one-dimensional overlayers, the details of the Mo(112) band structure must be understood and thus drives us to re-examine the band structure of Mo(112) in far greater detail than before.

6.2 Experimental details

The high-resolution angle-resolved photoemission spectroscopy (ARPES) was performed at the linear undulator beamline (BL-1) [41] of Hiroshima Synchrotron Radiation Center (HiSOR) at Hiroshima University, Japan. The surface of the Mo(112) sample was cleaned by the methods described in section 4.1 [25-28,42]. Low energy electron diffraction (LEED) and Auger electron spectroscopy (AES) were used to verify the quality of the Mo(112) surface, including the periodic structural order. The amount of surface contamination, such as C and O, were evaluated to be below the detection limit of the AES.

The high-resolution ARPES spectra were taken along the two lines ($\overline{\Gamma}-\overline{\mathrm{X}}$ and $\overline{\Gamma}-\overline{\mathrm{Y}}$) in the surface Brillouin zone (SBZ), schematically illustrated in Figure 6.1, with the *s*- and *p*-polarization geometries (with the electric field vector of the incident plane-polarized light parallel to the surface and within the plane containing the surface normal respectively). The ARPES experiments were carried out using an angular (display) mode of the hemispherical electron analyzer (R4000, VG-Scienta) with the acceptance angle of ±15°. The experimental band structure mapping was performed using multiple photon energies but with an emphasis on the incident photon energy of 22 eV. The energy resolution was estimated to be 10 meV and the angular resolution was 0.3°, corresponding to the wave vector resolution of 0.01±0.001 Å^{-1} at the Fermi level. The obtained ARPES spectra were not seen to be completely symmetric about $\overline{\Gamma}$ in the *p*-polarization geometry, which likely derives from the small misalignment of the sample. In addition, the electromagnetic field component perpendicular to the surface may vary due to the presence of vacuum-solid interface, which may give a rise to nontrivial dependence of photoemission matrix element on photon incident angle [43-50], so that in photoemission from surfaces for *p*-polarized geometry, there could be some apparent variation in the band intensities measured as a function of wave vector. For this reason, we have taken the averaged experimental band mapping on the both sides of $\overline{\Gamma}$. Thus, Figure 6.2b and 6.2e represents the band structure along $\overline{\Gamma}-\overline{\mathrm{X}}$ integrated over a finite thickness in k_y. The temperature of the sample was maintained at 50 K [51] by a constant flow of liquid helium. Throughout the discussion, the binding energies are referenced to the Fermi level, in terms of $E_F - E$.

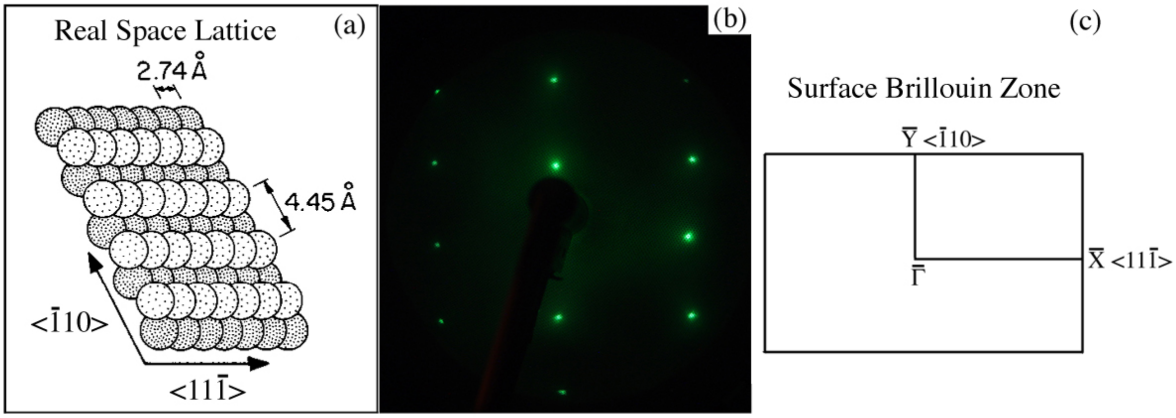

Figure 5.1: The structure of Mo(112) in real space as well as in the reciprocal space. (a) shows the schematic of real space structure. (b) shows the LEED pattern with $\langle \bar{1}10 \rangle$ direction aligned vertically. (c) shows the surface Brillouin zone of Mo(112).

6.3 Theoretical methodology

In order to obtain a theoretical band structure to be compared with the ARPES band mapping, DFT semi-relativistic calculations in generalized gradient approximation (GGA) [52] were performed with the ABINIT [53] package using Troullier-Martins norm-conserving pseudopotentials [54] by Prof. Ivan N. Yakovkin at the National Academy of Sciences of Ukraine. The periodicity in the direction normal to the surface was maintained by adopting the repeat-slab model. The slabs were built of 7 layers of Mo(112) atomic planes. The vacuum gap was about 10 Å. The optimizations of the atomic positions were performed until all forces became less than 0.05 eV/Å. The energy cutoff of 20 Hartrees (Ha) and 8×5×1 Monkhorst-Pack set of special *k* points provided the 0.001 Ha convergence of the total energy. The band structure along the high symmetry lines in the SBZ was calculated with a small step (0.036 Å^{-1}, corresponding to

33 *k*-points within the $\overline{\Gamma}-\overline{\mathrm{X}}$ line), which was found to be important to reveal the details of surface resonance bands in vicinity of E_F.

Surface weights for every band and *k*-point were estimated by integration of the partial local electron density within the atomic spheres (with r = 2.5 Bohr), using post-processing tools of the ABINIT. As the next-to-surface atomic layer of the open Mo(112) surface can also be attributed to the surface, the surface resonances correspond to the localization of the wave function within the first two surface layers. Some surface-derived states were found to be strongly localized in the top two surface layers (with weights of more than 90%), as discussed below. The symmetry of the surface bands was determined from the dominant partial weights of the states decomposed into spherical harmonics at the surface atoms.

Additionally, the band structure calculations based on 9 and 13 layer thick slabs of Mo(112) were performed in order to minimize the possible misinterpretation of the computational artefacts of the of the 7-layer slab calculation. Although the 7-layer slab calculation should reproduce most essential features deriving from the surface, these additional calculations serve to distinguish the possible ‘artificial’ surface resonances (i.e., arising solely due to the limited slab thickness) from the real surface resonances.

In order to further identify the ARPES spectral contribution from the pure bulk states, the projected bulk band structure calculations were performed by Dr. Tula R. Paudel at the University of Nebraska-Lincoln under the supervision of Prof. Evgeny Y. Tymbal. In these calculations, Mo unit cell was constructed such that two-dimensional Brilluoin zone matches the SBZ of Mo(112). Projector augmented-wave (PAW) [55] Perdew-Burke-Ernzerhof (PBE) [52] pseudopotential within the density functional theory

(DFT) band structure approach as implemented in VASP code [56,57] was utilized. The Mo 4*p*, 4*d* and 5*s* were treated as valence orbitals in the pseudopotential. The kinetic energy cutoff of 340 eV and 8x12x4 Monkhorst-Pack [58] *k*-points were taken for Brilluoin zone sampling.

6.4 The band structure characterization of Mo(112)

Utilization of linearly polarized light, as is available from synchrotron light sources, enables us to exploit the dipole selection rules for the photoemission process and allows us to clarify the symmetry properties of the electronic states in solids [59-61]. Although strictly peaking, Mo(112) is invariant only under the reflection about *xz*-plane (i.e., Mo(112) has C_{1h} symmetry), it is observed that the similarity of the crystal structure under the reflection about yz-plane (*near*-symmetry) is enough to produce the strong polarization dependence in accord with the dipole selection rule for C_{2v} structure (in which both reflection symmetries under *xz*- and *yz*-planes are present). Thus, for the discussion of symmetry of the electronic states of Mo(112), it is reasonable to assume that Mo(112) has a (near-) C_{2v} symmetry. Under such assumption, the pertinent point group symmetry is C_{2v} at $\bar{\Gamma}$, $\bar{\mathrm{X}}, \bar{\mathrm{Y}}$ and C_{1h} along the two high-symmetry directions ($\bar{\Gamma}-\bar{\mathrm{X}}$ and $\bar{\Gamma}-\bar{\mathrm{Y}}$). Since the final state of photoemission can be described by the plane wave traveling to the photoelectron analyzer, the photoelectrons in the final state transform as the fully symmetric representation in both groups of C_{2v} and C_{1h}. Under these assumptions, we may identify the symmetries of the initial states allowed to make a photoemission transition [59-61]. These allowed initial symmetries are summarized in Table 6.1 according to the directions of light polarization. Note that, throughout the present discussion, the coordinate axes are defined so that the $\langle 11\bar{1}\rangle$ direction (the $\bar{\Gamma}-\bar{\mathrm{X}}$ direction in SBZ) coincides with *x*-axis and the $\langle \bar{1}10\rangle$ direction (the $\bar{\Gamma}-\bar{\mathrm{Y}}$ direction in SBZ) coincides with *y*-axis. Since the direction of light incidence and photoelectron detection lie within the same plane (*xz*-plane for the spectra taken along the $\bar{\Gamma}-\bar{\mathrm{X}}$ direction and *yz*-plane for the spectra taken along the $\bar{\Gamma}-\bar{\mathrm{Y}}$ direction), the vector potential of incident light in the *p*-polarization (*s*-polarization) geometry lies in the *xz*-plane (*y*-axis) for the spectra taken along the $\bar{\Gamma}-\bar{\mathrm{X}}$ direction and lies in *yz*-plane (*x*-axis) for the spectra taken along the $\bar{\Gamma}-\bar{\mathrm{Y}}$ direction.

High symmetry points	Symmetry group	Irreducible representations (Basis functions)	Allowed initial symmetries		
			A || x	A || y	A || z
$\bar{\Gamma}-\bar{\mathrm{X}}$	C_{1h}	A’ (x, z, z^2, xz, x^2-y^2), A” (y, xy, yz)	A’	A”	A’
$\bar{\Gamma}-\bar{\mathrm{Y}}$	C_{1h}	A’ (y, z, z^2, yz, x^2-y^2), A” (x, xy, xz)	A”	A’	A’
$\bar{\Gamma}$, $\bar{\mathrm{X}}$, $\bar{\mathrm{Y}}$	C_{2v}	A_1 (z, z^2), A_2 (xy), B_1 (x, xz), B_2 (y, yz)	B_1	B_2	A_1

Table 6.1: The dipole selection rules for the electronic states at $\bar{\Gamma}$, $\bar{\mathrm{X}}$, $\bar{\mathrm{Y}}$ points (C_{2v}) and along the $\bar{\Gamma}-\bar{\mathrm{X}}$ and the $\bar{\Gamma}-\bar{\mathrm{Y}}$ directions (C_{1h}). The irreducible representations in each point group are listed in the third column with the representative basis functions in the parentheses. Allowed initial state symmetries in the photoemission are listed for each direction of incident light polarization determined by the vector potential A. The *x*-axis and *y*-axis are defined parallel to $\bar{\Gamma}-\bar{\mathrm{X}}$ and $\bar{\Gamma}-\bar{\mathrm{Y}}$ respectively, and *z*-axis is along the surface normal direction. For the ARPES taken along the $\bar{\Gamma}-\bar{\mathrm{X}}$ direction, vector potential in the *s*-polarized geometry only has *y*-component and that of the *p*-polarized geometry has the mixture of *x*- and *z*-components. Similarly, for the ARPES taken along the $\bar{\Gamma}-\bar{\mathrm{Y}}$ direction, vector potential in the *s*-polarized geometry only has *x*-component and that of the *p*-polarized geometry has the mixture of *y*- and *z*-components. The final state of photoemission is assumed to be described by a plane wave, which transforms as

the fully symmetric representations, A_1 and A', in both symmetry groups of C_{2v} and C_{1h} respectively.

6.4.1 The band structure along the $\overline{\Gamma}-\overline{X}$ direction

While two bands have been observed to cross the Fermi level at 0.45±0.05 $Å^{-1}$ and 0.59±0.05 $Å^{-1}$ along the $\overline{\Gamma}-\overline{X}$ direction in ARPES [25,26,28], with the higher resolution and improved sensitivity of ARPES, three additional bands can now be observed and resolved crossing the Fermi level along the $\overline{\Gamma}-\overline{X}$ direction, as seen in the experimental band structure in Figure 6.2. Figure 6.2b shows the ARPES band mapping taken along the $\overline{\Gamma}-\overline{X}$ direction with the p-polarized geometry. Four bands are found to cross the Fermi level (labeled as p_1, p_2, p_3, p_4). The Fermi level crossings of the p_1 and p_2 bands are identified to be 0.47 $Å^{-1}$ and 0.60 $Å^{-1}$ respectively and are consistent with the previously observed values [25,26,28]. The newly found bands, labeled as p_3 and p_4, are seen to cross the Fermi level at 0.64 $Å^{-1}$ and 0.81 $Å^{-1}$ respectively, as summarized in Table 6.2. It is known that for the electronic states along the $\overline{\Gamma}-\overline{X}$ direction, the symmetry of the wave function can be classified either as even (A' representation) or odd (A" representation) with respect to the reflection about *xz*-plane. Since the incident light polarization lies within *xz*-plane for the *p*-polarized geometry, the selection rule (Table 6.1) reveals that the light can only excite the electrons from the states with even reflection-parity about *xz*-plane (A'). Thus, the four bands seen to cross the Fermi level in Figure 6.2b are experimentally identified as even states for the binding energies near the Fermi level.

The result of the band structure calculation based on 7-layer slab model is shown in Figure 6.2a and the calculated surface weights (defined here as the charge localization within the first two layers) near the Fermi level for selected bands are summarized in Table 6.2. In Figure 6.2a, the states with noticeable surface weight are marked with blue symbols, and among those surface-weighted states, the clearly identified even states (A') are marked with blue circles. The calculated band structure has been overlaid on the experimental ARPES band mapping, as shown in Figure 6.2c and the respectable quantitative agreement is obtained between the theoretical and experimental band structures except for the p_3 band.

Among the four bands experimentally observed crossing the Fermi level along the $\overline{\Gamma}-\overline{X}$ direction, the band labeled p_1 was found to exhibit noticeable photon energy dependence. Although this band (p_1) is seen to cross the Fermi level at 0.47 $Å^{-1}$ at the photon energy of 22 eV (Figure 6.2b), the Fermi level crossing of this band is found to be 0.40 $Å^{-1}$ at the photon energy of 50 eV and variously reported to be crossing the Fermi level with wave vectors as high as 0.54 $Å^{-1}$ [11,28]. Such photon energy dependence indicates dispersion of the p_1 band in $k_\perp$ (the wave vector perpendicular to the surface) and suggests the bulk origin of the band. This identification is supported by the relatively small surface weight of 51% in the band structure calculation, as summarized in Table 6.2. Figure 6.3b shows the projected bulk band structure along $\overline{\Gamma}-\overline{X}$ direction in which the calculated band structures at 10 different $k_\perp$ are overlaid. Since this calculation shows the high density of bulk bands that gives quantitative agreement with the p_1 band in ARPES band mapping, it serves to further confirm the bulk band structure origin of the p_1 band.

The p_2 band, with the Fermi level crossing at 0.60 $Å^{-1}$ (experiment), was found to be sensitive to small amount of surface contamination (the intensity of this band was seen to vary while those of the other bands remained nearly constant). Such surface sensitivity of the p_2 band most likely derives from the fact that it carries a strong surface weight (78% as shown in Table 6.2), and it can be seen in Figure 6.2c that the calculated position of the band as well as its Fermi level crossing (k_F = 0.58 $Å^{-1}$) are in a good agreement with the experiment. Since the projected bulk band calculation, shown in Figure 6.3b, indicates no bulk band that exhibits the dispersion of the p_2 band in ARPES band mapping, evidently this band should not be identified as a bulk band. For these reasons, the p_2 band must largely be surface in origin and should be identified either as a surface resonance or true surface state of the Mo(112) surface. The further theoretical analysis revealed that the dominant orbital contributions to this band are of d_z^2 and d_{xz} character, leading to the even reflection-parity of the wave function near the Fermi level, which is consistent with the visibility of this band in the *p*-polarized spectrum and the invisibility in the *s*-polarized spectrum (Figure 6.2e).

The p_3 band, with the Fermi level crossing at 0.64 $Å^{-1}$ (experiment), is evident in the ARPES band mapping, but not reproduced in the band structure calculation based on 7-layer slab model (Figure 6.2c). On the other hand, the projected bulk band structure calculation (Figure 6.3b) clearly shows the presence of the densely spaced bulk bands in qualitative agreement with the p_3 band in observed in ARPES (Figure 6.2b) in terms of both the position and the dispersion. Therefore, the p_3 band likely originates from the bulk band continuum.

The p_4 band (Figure 6.2b), with the Fermi level crossing at 0.81 $Å^{-1}$ (experiment), was also found to exhibit surface sensitivity in the experiment. On the other hand, the result of the band structure calculations based on 7-layer slab model suggest the existence of two closely spaced bands, labeled as p_4 and p_4' in Figure 6.2a, with nearly equal significant surface weights (> 90%) with the Fermi level crossings at 0.82 and 0.88 $Å^{-1}$ (Table 6.2). These two bands (p_4 and p_4') both exhibit the predominant $d_z{}^2$ orbital character (i.e., even states), hence the expected visibility in the experimental band structure taken in the *p*-polarized geometry. This apparent discrepancy that the closely spaced double bands are not observed in ARPES is resolved by comparing the calculations based on the slab models of different thickness. Figure 6.3a shows the overlay of the calculated band structures using 7, 9 and 13-layer slab models. In this comparison, it is seen that the p_4 band found in 7-layer slab calculation remains nearly unchanged as the slab thickness is increased, which is an evidence of surface localization of the p_4 band. However, the wave vector position of the p_4' band is seen to be sensitive to the slab thickness, indicative of the greater bulk band structure attributes of the p_4' band. The calculated projected bulk band structure (Figure 6.3b) further verifies this assignment. It is evident in this calculation that the bulk bands exhibiting the dispersion similar to p_4' bands are present in the region of the p_4 and p_4' bands. Thus, the comparison of the calculated band structures among the different slab thickness as well as the projected bulk band structure leads us to identify the p_4' band in 7-layer calculation (Figure 6.2a) as the band from the bulk continuum that appears near the p_4 surface-derived band. Furthermore, since the surface-derived p_4 band lies within this bulk continuum which shares the same symmetry with that of the p_4 band, this band is likely identified as surface resonance, not the true surface band.

Figure 6.2e shows the experimental ARPES band mapping taken along the $\bar{\Gamma}-\bar{X}$ direction with the *s*-polarized geometry. It is evident that the band structure acquired in the *s*-polarized geometry is significantly different from that taken with the *p*-polarized geometry. In Figure 6.2e, there is a distinct band (labeled as s_1) with downward dispersion (towards greater binding energy) away from $\bar{\Gamma}$. Note that the s_1 band loses most of its intensity between 0.5 eV and 1.2 eV. The results of the band structure calculation are shown in Figure 6.2d, where the states with noticeable surface weight are marked with blue symbols and the electronic states clearly identified as odd (A”) with respect to *xz*-plane are marked with blue triangles. The position of the Fermi level crossing for this band (s_1) is in a respectable agreement with the calculation for the both parts (above 0.5 eV and below 1.2 eV) of this band, as seen in Figure 6.2f and Table 6.2. Since the incident light polarization lies along *y*-axis for the *s*-polarized geometry, by the selection rules (Table 6.1), the symmetry of this electronic state is identified to be odd under the reflection about *xz*-plane (A”). The strong photoemission intensity of this downward-dispersing band in the experimental band structure in the *s*-polarized geometry is in agreement with our expectations from the calculation (odd states are signified with blue triangles). We suggest that the s_1 band originates mostly from the bulk state continuum above 0.5 eV, as the projected bulk band structure calculation also reproduces the bands with very similar dispersions and positions to those of the s_1 band, as shown in Figure 6.3b. On the other hand, the lower part (below 1.2 eV) of the s_1 band should contain noticeable surface weight as it is only reproduced in the surface slab calculations

(Figure 6.3a), but not in the bulk calculation. The band structure calculation also predicts the existence of the shallow band crossing the Fermi level at 0.40 Å^{-1} and 0.62 Å^{-1}, much like an electron pocket (labeled as s_2 in Figure 6.2d). This band is predicted to be of odd reflection-parity (hence is expected to be visible only in the experimental band structure taken in the *s*-polarized geometry). The s_2 electron pocket is likely observed as the "glowing" region in the experimental band structure obtained in the *s*-polarized geometry (Figure 6.2e). Although the 7-layer slab calculation indicates the discernable surface weight of this band (between 62% and 77% depending on the wave vector $k_{||}$), we find in the comparison of 7, 9 and 13-layer slab calculations that the position of the band in wave vector k (but not its shape, that is to say the dispersion in $E(k)$) exhibits a noticeable dependence on the slab thickness as shown in Figure 6.3a. Furthermore, the projected bulk band calculation (Figure 6.3b) reproduced the bands of very similar characteristics (i.e., the electron-pocket-like bands between 0.4 Å^{-1} and 0.7 Å^{-1} that shifts vertically as a function of $k_{\perp}$). Thus, it is likely that s_2 band identified in ARPES band mapping and the 7-layer slab calculation (Figure 6.2d,e) is part of the projection of a bulk band. It is worthwhile to note, at the same time, that the s_2 band is predicted to exhibit fairly steep dispersion along $k_{\perp}$, as can be seen from the large spacing among the s_2 projected bulk bands in Figure 6.3c. Such steep dispersion in $k_{\perp}$ direction may have caused the spread of ARPES intensity in the wide range, as seen Figure 6.2e.

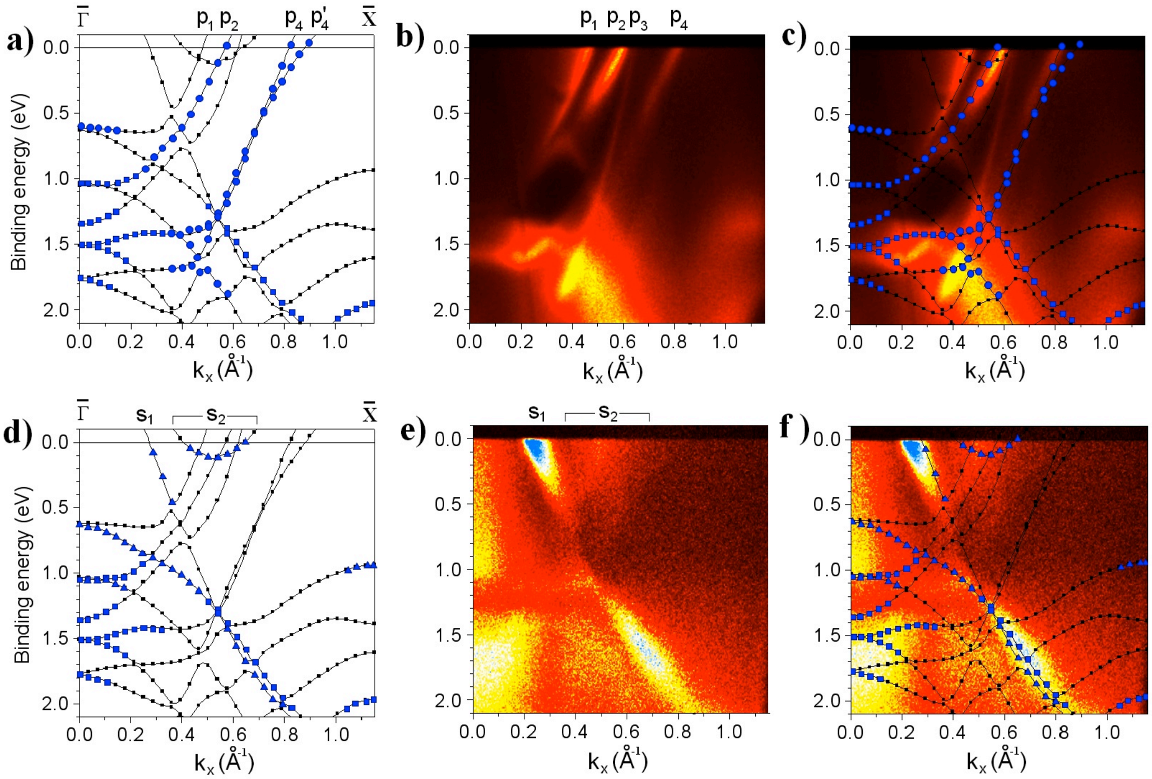

Figure 6.2: The band structure of Mo(112) along the $\bar{\Gamma}-\bar{\mathrm{X}}$ direction. (a) shows the calculated band structure with the 7-layer slab model. The states with noticeable surface weight (more than 60% charge localization within the first two layers) are marked with blue symbols (■,●) out of which circles (●) represent the states of clearly identified even symmetry with respect to *xz*-plane (A' representation). (b) shows the ARPES band mapping taken with the *p*-polarized geometry at the photon energy of 22 eV. (c) shows the comparison of the calculated band structure with the ARPES band mapping taken with the p-polarized geometry. (d) shows the calculated band structure (same as (a)) but with the clearly identified odd states with respect to *xz*-plane (A'') marked with blue triangles (▲). (e) shows the ARPES band mapping taken with the *s*-polarized geometry at the photon energy of 22 eV. (f) shows the comparison of the calculated band structure with the ARPES band mapping taken with the *s*-polarized geometry.

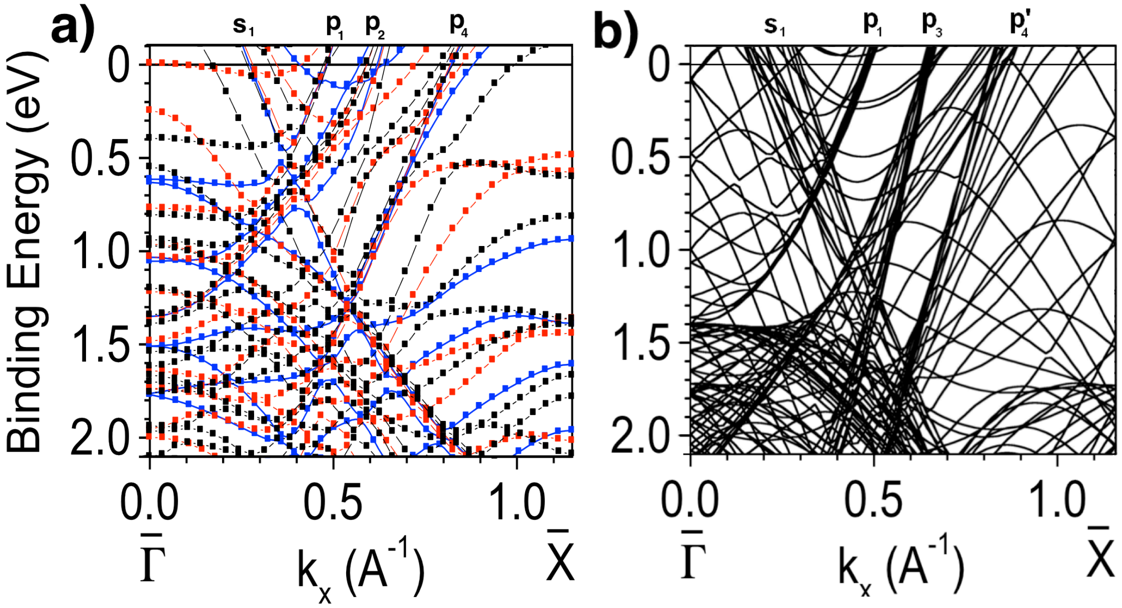

Figure 6.3: (a) the overlay of the calculated band structures along $\bar{\Gamma}-\bar{X}$ direction based on 7 (🟦), 9 (🟥) and 13 (⬛) layer slab models, which is expected to show the surface-derived bands as well as some of the bulk bands. (b) the projected bulk band structure of Mo(112), which is composed of the band structures calculated along $\langle 11\bar{1}\rangle$ direction (i.e., parallel to $\bar{\Gamma}-\bar{X}$) at 10 different $k_{\perp}$. The bands identified in AREPS band mapping and calculated band structure based on 7-layer slab model (Figure 2) are labeled correspondingly.

Band Label	k_F (Å^{-1}) experiment	k_F (Å^{-1}) theory	Surface Weight
p_1	0.47±0.01	0.48	51%
p_2	0.60±0.01	0.58	**78%**
p_3	0.64±0.01	-	-
p_4	0.81±0.01	0.82	**91%**
p_4'	0.81±0.01	0.88	**90%**
s_1	0.22±0.01	0.27	52%
s_2	~ 0.4-0.5	0.40-0.62	**62-77%**
y_1	0.34±0.01	0.36	**81%**

Table 6.2: The list of the bands crossing the Fermi level. The band labels are defined in the Figure 5.2 and 5.3. The 2nd and 3rd columns compare the Fermi wave vector for each band. The estimates of the surface weight (the percentage charge localization within the first two layers in the 7-monolayer model) near the Fermi level are listed for each band. Note that the experimentally observed p_3 band is not unambiguously reproduced in the present calculation.

6.4.2 The band structure along the $\bar{\Gamma}-\bar{\mathrm{Y}}$ direction

Due to the large in-plane interatomic distance along the $\langle\bar{1}10\rangle$ direction (4.45 Å), the electronic band structure along the $\bar{\Gamma}-\bar{\mathrm{Y}}$ direction is expected to be much less dispersive than in the $\langle 11\bar{1}\rangle$ direction (the $\bar{\Gamma}-\bar{\mathrm{X}}$ direction). This general tendency is evident in the experimental as well as in the calculated band structures, as shown in Figure 6.4. Along the $\bar{\Gamma}-\bar{\mathrm{Y}}$ direction, we note that the vector potential of incident light in the *p*-polarized geometry lies within *yz*-plane and that of the *s*-polarized geometry lies along *x*-axis. This dictates the selection rule for the ARPES along the $\bar{\Gamma}-\bar{\mathrm{Y}}$ direction, as summarized in Table 6.1.

Figure 6.4b shows the experimental band structure obtained along the $\bar{\Gamma}-\bar{\mathrm{Y}}$ direction with the *p*-polarized incident light geometry. The characteristic 'crossing' of the bands seen at $k_{\parallel}$ = 0.70 Å^{-1} and binding energy = 2.3 eV (2.4 eV in calculated band structure) experimentally places the edge of the surface Brillouin zone ($\bar{\mathrm{Y}}$) and is consistent with the value determined from the surface structure (0.706 Å^{-1}). Of particular interest in the band structure along the $\bar{\Gamma}-\bar{\mathrm{Y}}$ direction is the distinct parabolic band centered at $\bar{\Gamma}$, crossing the Fermi level at 0.34 Å^{-1} (labeled as y_1). This band is only evident in the ARPES band mapping obtained in the *p*-polarized geometry, indicating that the y_1 band is of even symmetry with respect to the *yz*-reflection (A') away from $\bar{\Gamma}$ and is of A_1 or B_2 symmetry at $\bar{\Gamma}$ (see Table 6.1). The calculated band structure, in Figure 6.4a (where again bands with significant surface weight are marked by blue symbols and even symmetry states are marked by blue circles), shows a good general agreement with the experimental band structure as shown in Figure 6.4c. In particular, there is an excellent agreement for the y_1 band in terms of dispersion, the placement of the Fermi level crossing (k_F = 0.36 Å^{-1} in theory), as well as the reflection-parity away from $\overline{\Gamma}$ (i.e., calculated to be even as signified by the circles in Figure 6.4a). Furthermore, the band structure calculation reveals the predominant $d_z{}^2$ orbital character and the noticeable surface weight (81%) for the y_1 band near the Fermi level.

To further verify the surface or bulk origin and weight of the y_1 band, band structure calculations based on different slab thickness as well as the projected bulk band structure calculations were performed and compared for $\overline{\Gamma}-\overline{\mathrm{Y}}$ direction. Figure 6.5a shows the overlay of slab calculations based on 7, 9 and 13 layer models. The y_1 band exhibits noticeable dependence on the slab thickness in the calculated band structure in terms of position and dispersion, an indication of bulk weight. On the other hand, the projected bulk band calculation, shown in Figure 6.5b, is not in good quantitative agreement with the y_1 band observed in ARPES. The ARPES band mapping is not expected to give precise agreement with the bulk band structure mapped along the straight line in bulk Brillouin zone, because the "sampling depth" of $k_\perp$ in ARPES varies with wave vector parallel to the surface for photoemission at single photon energy, but even with this consideration in mind, quantitative agreement between the ARPES and bulk band structure calculation is absent, particularly near the Fermi level. Such a discrepancy between experiment and theory may have arisen from two artificial effects of bulk and slab calculations that (1) the bulk calculation does not take into account any mixing of the states with surface-derived states, and (2) the present slab calculation does not properly include the mixing of the surface states with the bulk continuum for any weak surface resonance that penetrates into bulk more than 13 layers. We tentatively suggest that the y_1 band be identified as weakly surface weighted, particularly near the Fermi level (i.e., where the agreement between the bulk/slab calculations and ARPES is relatively poor).

Figure 6.4e shows the ARPES band mapping taken along the $\overline{\Gamma}-\overline{Y}$ direction with the *s*-polarized geometry. In this experimental band structure, there is no distinct band crossing the Fermi level. Although there is noticeable continuous spread of photoemission intensity, which resembles an hourglass shape between 0.3 and 0.4 Å^{-1} near the Fermi level, this is likely a contribution from the projected bulk bands, as is suggested by comparison with the bulk band structure calculation in Figure 6.5b. As seen in Figure 6.4d and 6.4f, the band structure obtained by ARPES and the calculated band structure are in general agreement. The upward-dispersing band and the downward-dispersing band that merge at $\overline{Y}$ near 2.3 eV, in Figure 6.3f, are most likely projected bulk bands. These bands are reproduced in the projected bulk band structure calculation. Since these bulk bands are only distinct in the *s*-polarized spectrum, they are experimentally identified as of odd symmetry.

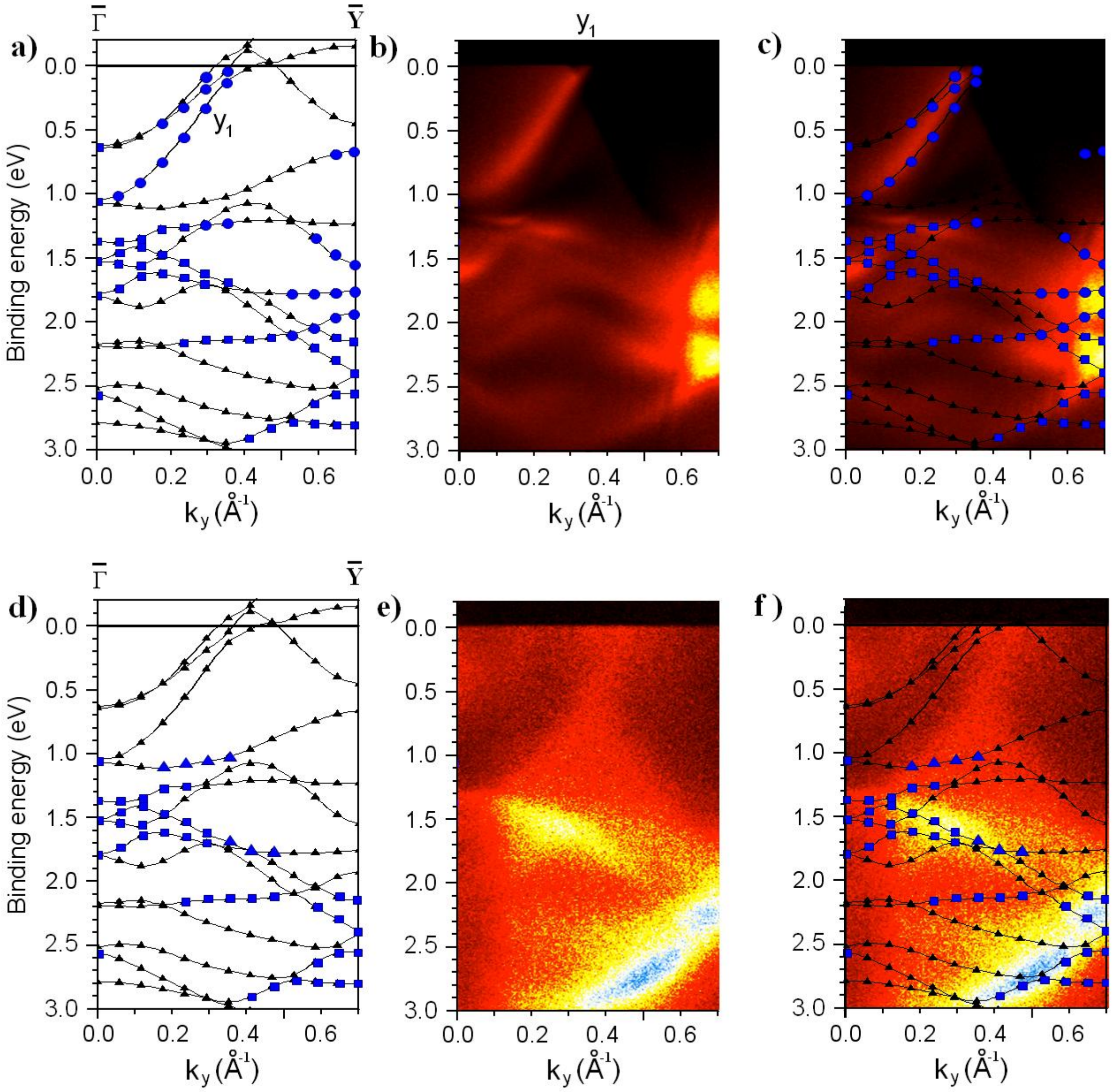

Figure 6.4: The band structure of Mo(112) along the $\overline{\Gamma}-\overline{Y}$ direction. (a) shows the calculated band structure with the 7-layer slab model. The states with noticeable surface weight (more than 60% charge localization within the first two layers) are marked with blue symbols (■,●) out of which circles (●) represent the states of clearly identified even symmetry with respect to *yz*-plane (A' representation). (b) shows the ARPES band mapping taken with the *p*-polarized geometry at the photon energy of 22 eV. (c) shows the comparison of the calculated band structure with the ARPES band mapping taken with the *p*-polarized geometry. (d) shows the calculated band structure (same as (a)) but with the clearly identified odd states with respect to *yz*-plane (A") marked with blue triangles (▲). (e) shows the ARPES band mapping taken with the *s*-polarized geometry

at the photon energy of 22 eV. (f) shows the comparison of the calculated band structure with the ARPES band mapping taken with the *s*-polarized geometry.

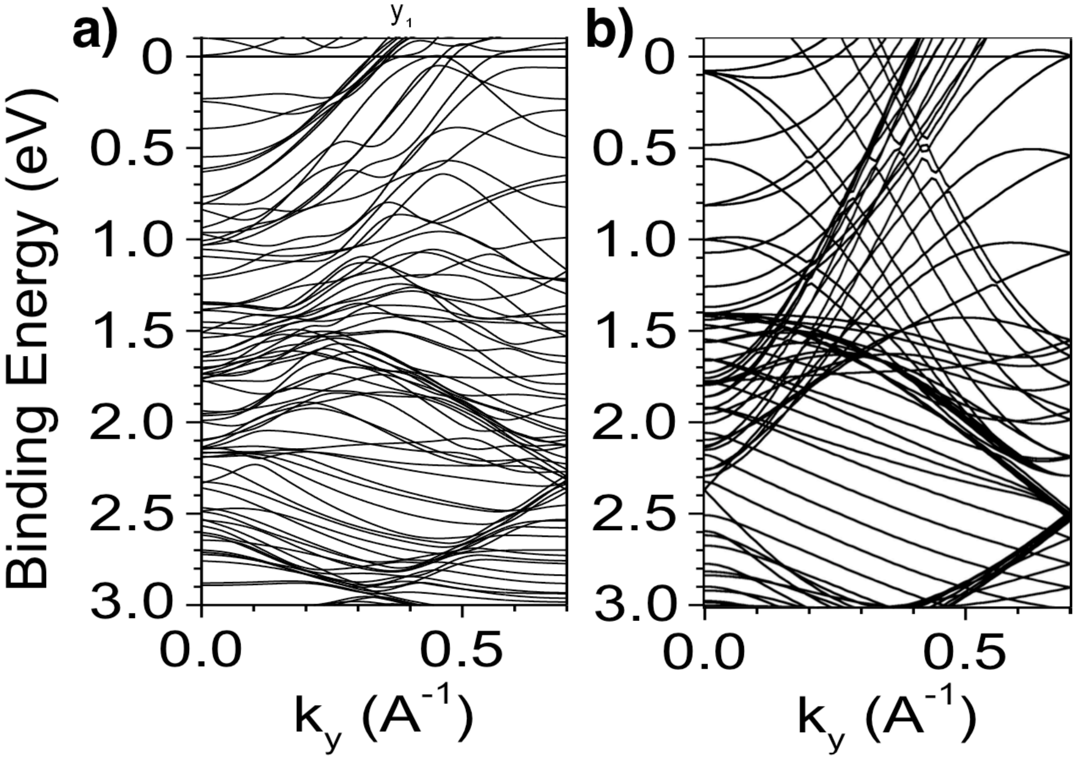

Figure 6.5: (a) the overlay of the calculated band structures along $\bar{\Gamma}-\bar{Y}$ direction based on 7, 9 and 13-layer slab models, which is expected to show the surface-derived bands as well as some of the bulk bands. (b) the projected bulk band structure of Mo(112), which is composed of the band structures calculated along $\langle\bar{1}10\rangle$ direction (i.e., parallel to $\bar{\Gamma}-\bar{Y}$) at 10 different $k_{\perp}$. The bands identified in AREPS band mapping and calculated band structure based on 7-layer slab model (Figure 6.4) are labeled correspondingly.

6.4.3 The electronic states near $\bar{\Gamma}$

There are number of distinct states observed near $\bar{\Gamma}$. Since the pertinent point group symmetry at $\bar{\Gamma}$ is C_{2v}, the symmetry of the electronic states at this point can be classified into A_1, A_2, B_1 and B_2 representations, as opposed to the even (A') and odd (A") classifications along the $\bar{\Gamma}-\bar{X}$ and the $\bar{\Gamma}-\bar{Y}$ directions. The utilization of the photoemission selection rules (Table 6.1) allows us to clarify the symmetry properties of the electronic states at $\bar{\Gamma}$. Figure 6.6 shows the energy distribution curves (EDCs) of the photoemission spectra at $\bar{\Gamma}$ (integrated over ±0.01 Å^{-1}) for the four distinct incident light polarizations (the polarization of vector potential A for each EDC is noted in the legend). The peak at around the binding energy of 1.0 eV is identified in the spectra (b) and (c) in which the light polarization lies within *yz*-plane and along *y*-axis respectively. The absence of this peak in the other two spectra is consistent and thus indicates that this state, at 1.0 eV binding energy near $\bar{\Gamma}$, is of B_2 symmetry. It was previously reported that the position of this band exhibited noticeable periodic photon energy dependence in the range of 18-83 eV [25,26]. Since our band structure calculations show the relatively low surface weight of 56-67% (note that the surface weight of this band near the Fermi level is estimated to be 81% along $\bar{\Gamma}-\bar{Y}$), this band at 1.0 eV binding energy near $\bar{\Gamma}$ is identified either as a projected bulk state or a surface resonance that is strongly hybridized with the bulk bands.

There is another peak at 1.5 eV binding energy near $\bar{\Gamma}$, which is pronounced only in the spectra (a) and (b) of Figure 6.6. From the selection rules, this state is most likely of A_1 symmetry character. In fact, this is consistent with the previously suggested symmetry of this state as inferred from the angular dependence of the photoemission intensity in the earlier study [26]. It was also reported that this state exhibited only weak, but discernable, photon energy dependence [26]. In fact our calculation identifies the significant surface charge localization for this state (87-92%) and thus we suggest attributing the observed state, at a binding energy of 1.5 eV, to a surface resonance state.

It is important to point out that the symmetry identification of the band at the binding energy of 1.0 eV at $\bar{\Gamma}$ (B_2) requires that while the p_2 band along $\bar{\Gamma}-\bar{X}$ (Figure 6.2a, 6.2b) and the y_1 band along $\bar{\Gamma}-\bar{Y}$ (Figure 6.4a, 6.4b) both reach $\bar{\Gamma}$ at around 1.0 eV binding energy, these two bands should not actually meet (or become degenerate) at $\bar{\Gamma}$, unless there is an accidental degeneracy. The reflection-parity of a B_1 state is odd with respect to *xz*-plane, but even with respect to *yz*-plane. However, since the reflection-parity of the p_2 band is identified as even with respect to *xz*-plane, the symmetry of the p_2 band is incompatible with the state found at 1.0 eV binding energy. Thus, the state of B_2 symmetry found at $\bar{\Gamma}$, in Figure 6.6, must be attributed to the y_1 band but not to the p_2 band. Therefore, the vanishingly small ARPES intensity of the p_2 band near $\bar{\Gamma}$ cannot a priori be associated with photoemission selection rules.

6.5 Summary

The band structures along the two high-symmetry directions, $\bar{\Gamma}-\bar{X}$ and $\bar{\Gamma}-\bar{Y}$, are shown to be significantly different, which is expected and serves to verify the strong anisotropy of the surface of Mo(112). By utilizing the light-polarization-dependence of ARPES spectra and the dipole selection rules, the symmetry character of some bands are identified and seen to be in good agreement with the expectations. Our study suggests the existence of at least two surface resonance bands along the $\bar{\Gamma}-\bar{X}$ direction (with k_F = 0.59 Å^{-1} and 0.81 Å^{-1}) and one along the $\bar{\Gamma}-\bar{Y}$ direction (with k_F = 0.34 Å^{-1}).

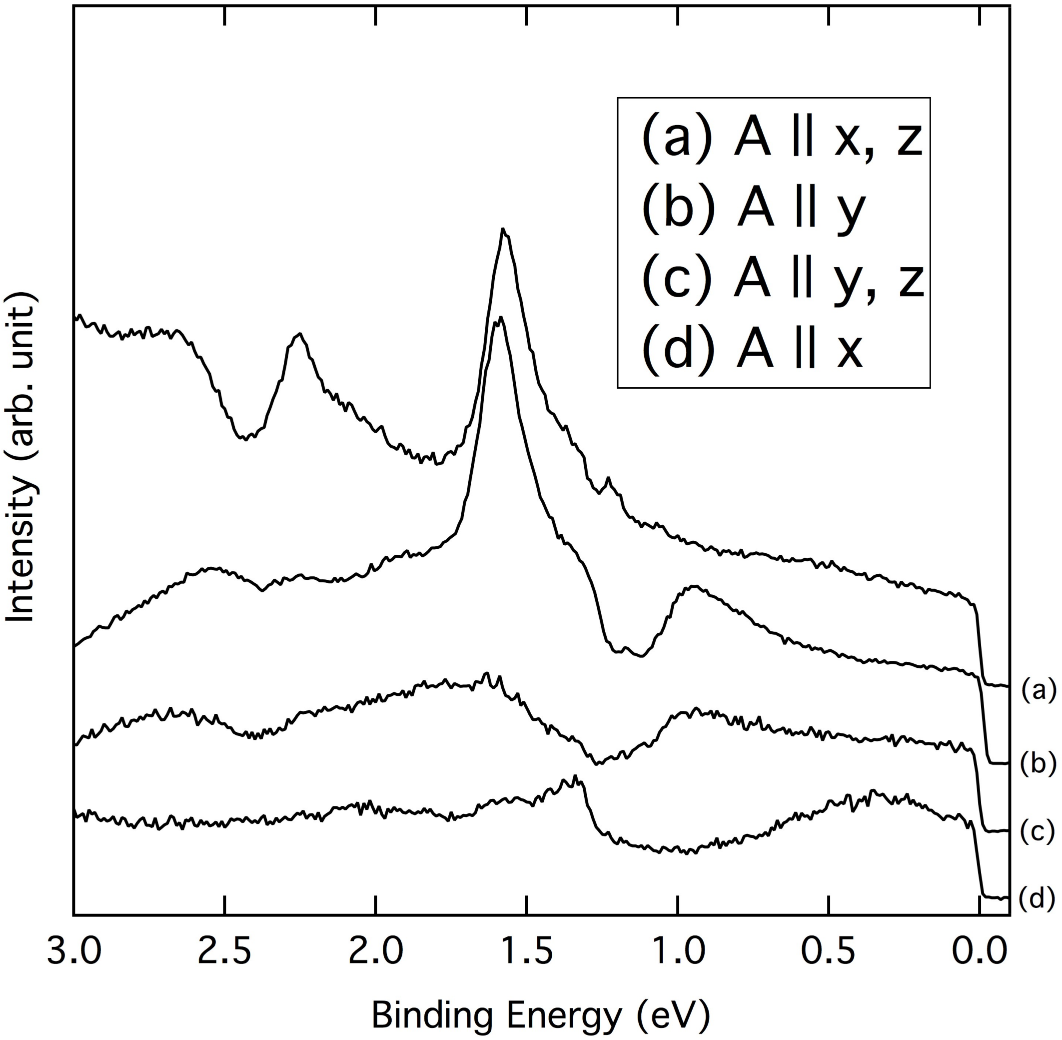

Figure 6.6: The energy distribution curves (photoemission intensity vs. binding energy) at $\bar{\Gamma}$ for the four different incident light polarization geometry. The data are obtained by integrating the ARPES spectra in Figure 6.2 (b), (e) and Figure 6.3 (b), (e) over ±0.01 $Å^{-1}$. The non-vanishing component(s) of vector potential A for the four incident light polarization geometries are; (a) x- and z-component (b) y-component, (c) y- and z-component, (d) x-component.

References

[1] I.E. Tamm, *Phys. Z. Soviet Union* **1**, 732 (1932).

[2] A.-W. Maue, *Z. Physik* **94**, 717 (1935).

[3] W. Shockley, *Phys. Rev.* **56**, 317 (1939).

[4] E.T. Goodwin, *Proc. Camb. Phil. Soc.* **35**, 205 (1939).

[5] E.T. Goodwin, *Proc. Camb. Phil. Soc.* **35**, 221 (1939).

[6] E.T. Goodwin, *Proc. Camb. Phil. Soc.* **35**, 232 (1939).

[7] S. Weng, *Phys. Rev. Lett.* **38**, 434 (1977).

[8] S.-L. Weng, T. Gustafsson and E.W. Plummer, *Phys. Rev. Lett*. **39**, 822 (1977).

[9] S.-L. Weng, T. Gustafsson and E.W. Plummer, *Phys. Rev*. B **18**, 1718 (1978).

[10] T. Valla, A.V. Fedorov, P.D. Johnson and S.L. Hulbert, *Phys. Rev. Lett.* **83**, 2085 (1999).

[11] N. Wu, Ya. B. Losovyj, K. Fukutani, and P.A. Dowben, *J. Physics Condensed Matter* **22**, 245501 (2010).

[12] T.E. Felter, R.A. Barker, and P.J. Estrup, *Phys. Rev. Lett*. **38**, 1138 (1977).

[13] J.W. Chung, K.S. Shin, D.H. Baek, C.Y. Kim, H.W. Kim, S.K. Lee, C.Y. Park, T. Kinoshita, M. Watanabe, A. Kakizaki, and T. Ishii, *Phys. Rev. Lett.* **69**, 2228 (1992).

[14] K.E. Smith and S.D. Kevan, *Phys. Rev.* B **43**, 3986 (1991).

[15] X.W. Wang, C.T. Chan, K.M. Ho, and W. Weber, *Phys. Rev. Lett*. **60**, 2066 (1988).

[16] I. Terakura, K. Terakura, and N. Hamada, *Surf. Sci.* **103**, 103 (1981).

[17] E. Hulpke and D.M. Smilgies, *Phys. Rev*. B **40**, 1338 (1989).

[18] J. E. Inglesfield, *J. Phys.* C **11**, L69 (1978).

[19] J. E. Inglesfield, *J. Phys.* C **12**, 149 (1979).

[20] R.A. Barker, P.J. Estrup, F. Jona, P.M. Marcus, *Sol. State Commun*. **25**, 375 (1978).

[21] R.E. Peierls, *Qunatum Theory of Solids* (Oxford University Press, Oxford, 1955).

[22] E. Tosatti, *Solid State Commun*. **25**, 637 (1978).

[23] H. Krakauer, M. Posternak, and A.J. Freeman, *Phys. Rev. Lett*. **43**, 1885 (1979).

[24] J. C. Campuzano, D.A. King, C. Somerton, and J.E. Inglesfield, *Phys. Rev. Lett*. **45**, 1649 (1980).

[25] T. McAvoy, J. Zhang, C. Waldfried, D.N. McIlroy, P.A. Dowben, O. Zeybek, T. Bertrams, and S.D. Barrett, *European Physical Journal* B **14**, 747 (2000).

[26] I.N. Yakovkin, J. Zhang, and P.A. Dowben, *Physical Review* B **63**, 115408 (2001).

[27] H.-K. Jeong, T. Komesu, I.N. Yakovkin, and P.A. Dowben, *Surface Science Letters* **494**, L773 (2001).

[28] N. Wu, Ya. B. Losovyj, Z. Yu, R.F. Sabirianov, W.N. Mei, N. Lozova, J.A. Colón Santana, and P.A. Dowben, *J. Phys. Cond. Matter* **21**, 474222 (2009).

[29] I.N. Yakovkin, *Surf. Sci.* **389**, 48 (1997).

[30] I.N. Yakovkin, *Eur. Phys. J.* B **44**, 551 (2005).

[31] D. Kolthoff, H. Pfnür, A.G. Fedorus, V. Koval and A.G. Naumovets, *Surf. Sci.* **439**, 224 (1999).

[32] A. Fedorus, D. Kolthoff, V. Koval, I. Lyuksyutov, A.G. Naumovets, and H. Pfnur, *Phys. Rev.* B **62**, 2852 (2000).

[33] A. Kiejna and R.M. Nieminen, *Phys Rev.* B **66**, 085407 (2002).

[34] A. Fedorus, G. Godzik, V. Koval, A. Naumovets, and H. Pfnur, *Surf. Sci*. **460**, 229 (2000).

[35] A. Kiejna and R.M. Nieminen, *Phys. Rev.* B **69**, 235424 (2004).

[36] V.K. Medvedev and I. N. Yakovkin, *Fiz. Tverd. Tela* **20**, 928 (1978).

[37] V.K. Medvedev and I. N. Yakovkin, *Fiz. Tverd. Tela* **21**, 313 (1979) [*Sov. Phys. Solid State* **21** (1979) 187]

[38] V.K. Medvedev and I. N. Yakovkin, *Fiz. Tverd. Tela* **23**, 669 (1981).

[39] Ya.B. Losovyj, I.N. Yakovkin, H.-K. Jeong, D. Wisbey, and P.A. Dowben, *J. Phys. Condens. Matter* **16**, 4711 (2004).

[40] I.N. Yakovkin, *Journ. Nanosci. Nanotechnol.* **1**, 357 (2001).

[41] K. Shimada, M. Arita, Y. Takeda, H. Fujino, K. Kobayashi, T. Narimura, H. Namatame, and M. Taniguchi, *Surface Review and Letters* **9**, 529 (2002).

[42] K. Fukutani, Ya.B. Losovyj, N. Lozova, N. Wu, P.A. Dowben, *J. of Electron Spectroscopy and Related Phenomena* **184**, 318 (2011).

[43] P.J. Feibelman, *Phys. Rev.* B **12**, 1319 (1975)

[44] H.J. Levinson, E.W. Plummer and P.J. Feibelman, *Phys. Rev. Lett*. **43**, 952 (1979)

[45] T. Miller, W.E. McMahon and T.-C. Chiang, *Phys. Rev. Lett.* **77**, 1167 (1996)

[46] E.D. Hansen, T. Miller and T.-C. Chiang, *Phys. Rev. Lett*. **78**, 2807 (1997)

[47] T. Miller, E.D. Hansen, W.E. McMahon and T.-C. Chiang, *Surf. Sci.* **376**, 32 (1997)

[48] F. Pforte, T. Michalke, A. Gerlach and A. Goldmann, *Phys. Rev.* B **63**, 115405 (2001)

[49] V.B. Zabolotnyy, S.V. Borisenko, A.A. Kordyuk, D.S. Inosov, A. Koitzsch, J. Geck, J. Fink, M. Knupfer, B. Buchner, S.-L. Drechsler, V. Hinkov, B. Keimer and L. Patthey, *Phys. Rev.* B **76**, 024502 (2007)

[50] N.J. Speer, M.K. Brinkley, Y. Liu, C.M. Wei, T. Miller and T.-C. Chiang, *EuroPhys. Lett*. **88**, 67004 (2009)

[51] Temperature is confirmed by deconvolution of the experimental width of the Fermi function and the expected instrumental broadening.

[52] J.P. Perdew, K. Burke, and M. Ernzerhof, *Phys. Rev. Lett*. **77**, 3865 (1996).

[53] X. Gonze, J.-M. Beuken, R. Caracas, F. Detraux, M. Fuchs, G.-M. Rignanese, L. Sindic, M. Verstraete, G. Zerah, F. Jollet, M. Torrent, A. Roy, M. Mikami, Ph. Ghosez, J.-Y. Raty, and D.C. Allan, *Comput. Mat. Sci*. **25**, 478 (2002).

[54] N. Troullier and J.L. Martins, *Phys. Rev.* B **43**, 1993 (1991).

[55] P. E. Blöchl, *Phys. Rev*. B **50**, 17953 (1994).

[56] G. Kresse and J. Furthmüller, *Comput. Mater. Sci*. **6**, 15 (1996).

[57] J. Paier, R. Hirschl, M. Marsman, and G. Kresse, *J. Chem. Phys*. **122**, 234102 (2005).

[58] H. Monkhorst and J. Pack, *Phys. Rev.* B **13**, 5188 (1976).

[59] P.A. Dowben, J. Choi, E. Morikawa, and B. Xu, *The Band Structure and Orientation of Molecular Adsorbates on Surfaces by Angle-Resolved Electron Spectroscopies*, in Handbook of Thin Films, ed. H. S. Nalwa, Characterization and Spectroscopy of Thin Films, (Academic Press, 2002) ch. 2, vol. 2, pp. 61–114.

[60] J. Hermanson, *Solid State Communications* **22**, 9 (1977).

[61] W. Eberhardt and F. J. Himpsel, *Phys. Rev.* B **21**, 5572 (1980).

Chapter 7
Enhanced Electron-phonon Coupling on Au/Mo(112)

7.1. Motivation

Electron-phonon coupling is one of the most fundamental many-body interactions in solid state physics, which is essential for the proper description of normal properties of materials as well as critical phenomena in solids [1]. The former includes low-temperature electronic heat capacity and finite electrical conductivity. The latter ranges from surface reconstructions to superconducting phase transitions [2,3]. Although the electron-phonon coupling is ubiquitous, due to the low excitation energy of phonons (typically <100 meV for metals), its effect on the electronic structure is most pronounced in the vicinity of Fermi level (E_F). Therefore, the quantification of electron-phonon coupling is most readily realized in the metallic systems for which the excitation energy is, by definition, zero.

The detailed experimental investigations of electron-phonon coupling utilizing high-resolution angle-resolved photoemission spectroscopy (ARPES) have become more common. Since the first direct experimental quantification of the electron-phonon coupling in Mo(110) [4], ARPES has been applied to various metals including Be(0001) [5-7], Cu(111), Ag(111), Au(111) [8-11], Fe(110) [12,13], Al(100) [8,14-16], and Mo(112) [17,18]. So far, the characterization of the electron-phonon coupling has been largely limited to clean, adsorbate-free systems and only a few studies have been devoted to the examinations of the electron-phonon coupling of adsorbate structures, such as H/W(110), for which a noticeable enhancement of the electron-phonon coupling is observed [19,20]. Yet, the adsorbate structures are known to exhibit various types of interesting phenomena such as overlayer structural phase transitions, and thus, major insights in such adlayer phase transitions and its properties may be obtained from a quantitative characterization of the electron-phonon coupling in overlayer structures.

Mo(112) surface is known to exhibit highly anisotropic electronic structure [21] on which Au forms the commensurate atomic chains, as schematically illustrated in Figure 7.1a. At certain coverages of Au/Mo(112), order-disorder transitions of the Au chains have been observed [22], as will be discussed in the later chapter. Electron-phonon coupling may well play an important role in such overlayer instabilities and thus, our investigation of the electron-phonon coupling of Au/Mo(112) can serve as an important milestone in the study of such overlayer instability.

7.2. Experimental details

The high-resolution ARPES was performed at the linear undulator beamline (BL-1) [23] of Hiroshima Synchrotron Radiation Center (HiSOR) at Hiroshima University, Japan. The surface of the Mo(112) sample was cleaned by the methods described in section 4.1 [21,24-28]. Low energy electron diffraction (LEED) and Auger electron spectroscopy (AES) were used to verify the quality of the Mo(112) surface. The amount of surface contamination, mainly C and O, were evaluated to be below the detection limit of the AES.

Deposition of Au was performed by physical vapor evaporation of Au onto the Mo(112) sample by heating the Au source below the melting temperature. The Au growth rate was adjusted to be sufficiently slow to ensure the layer-by-layer growth on Mo(112) surface up to the coverage of 1 monolayer (ML), for which the structure is illustrated in Figure 7.1a. The constant gradual growth of Au film within the submonolayer coverage was monitored by the linear relationship between the adsorbate coverage and Au peak intensity in AES [29]. At coverages near the completion of 1 ML, LEED was utilized to confirm the formation of the 1 ML 1x1 adlayer.

The high-resolution ARPES spectra were taken along the $\overline{\Gamma}-\overline{\mathrm{X}}$ line in $\langle\bar{1}\bar{1}1\rangle$ direction in the surface Brillouin zone (SBZ), schematically illustrated in Figure 7.1b, with the *s*-polarization geometry (where the vector potential A of incident light is perpendicular to the detection plane, lying parallel to y-direction in Figure 7.1a) and *p*-polarization geometries (where A lies within the detection plane or *xz*-plane in Figure 7.1a). The ARPES experiments were carried out using the angular mode of the hemispherical electron analyzer (R4000, VG-Scienta). The experimental band structure mappings for the entire dimension along $\overline{\Gamma}-\overline{\mathrm{X}}$ line (Figure 7.2) were performed using the incident photon energy of $\hbar\omega = 22$ eV with the analyzer acceptance angle of ±15° (Angular 30 mode). The energy resolution was estimated to be 10 meV and the angular resolution was ~0.9°, corresponding to the wave vector resolution of ~0.03 Å^{-1} at E_F. The close-up of the surface resonance band near E_F (Figure 7.3) was taken with the incident photon energy of $\hbar\omega = 22$ eV with the analyzer acceptance angle of ±7° (Angular 14 mode) with the estimated energy resolution of ~10 meV and the angular resolution of ~0.2°, corresponding to a wave vector resolution of ~0.008 Å^{-1} at E_F. The temperature of the sample was maintained at ~60 K by constant flow of liquid helium. Throughout the discussion, the binding energies are referenced to the Fermi level, in terms of $E_F - E$.

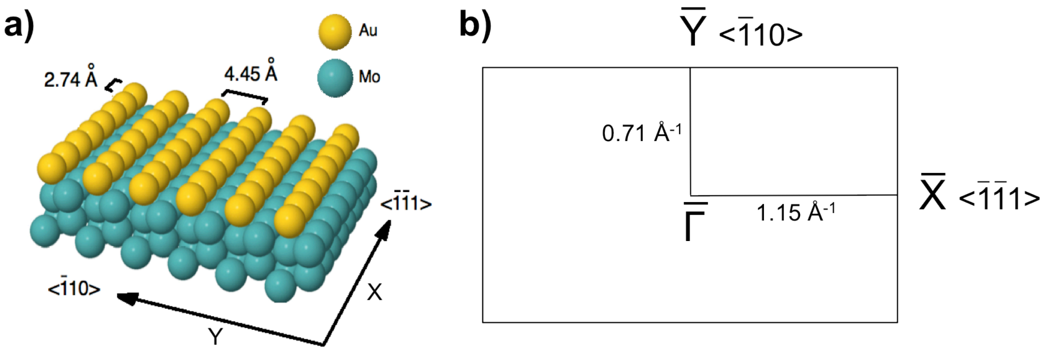

Figure 7.1: The schematic illustration of Au/Mo(112) at the coverage of nominal 1 ML (a). The corresponding surface Brillouin zone is illustrated in (b) with the approximate dimensions along $\bar{\Gamma}-\bar{X}$ and $\bar{\Gamma}-\bar{Y}$ lines.

7.3. Theoretical methodology

The DFT semirelativistic calculations in generalized gradient approximation (GGA) [30] were performed with the ABINIT [31] package using Troullier-Martins norm-conserving pseudopotentials [32] by Prof. Ivan N. Yakovkin at the National Academy of Sciences of Ukraine. The periodicity in the direction normal to the surface was maintained by adopting the repeat-slab model. The slabs were built of 7 layers of Mo(112) atomic planes with one Au layer on one side of the slab for the 1 ML Au/Mo(112) system. The vacuum gap was about 10 Å. The optimization of positions of atoms was performed until all forces became less than 0.05 eV/ Å. The energy cutoff of 20 Ha (Hartrees) and 6×4×1 Monkhorst-Pack set of special *k* points provided the 0.001 Ha convergence of the total energy.

Prof. Yakovkin has also provided the phonon band structure, phonon density of states, $F(\omega)$, and the Eliashberg function, $\alpha^2F(\omega)$, calculated by the response function method [33], implemented in the ABINIT set of programs [31]. The isotropic Eliashberg function was obtained by averaging over the wave vectors k_i and k_f of initial and final states on the Fermi surface. Using the Eliashberg function, we calculated the real and imaginary parts of the self-energy due to the electron-phonon coupling, and compared with the experimental ones in Sec. 7.5.

7.4. Electronic structure of Au/Mo(112)

Prior to the investigation of the electron-phonon coupling of Au/Mo(112), its detailed electronic band structure near E_F must be understood. This is crucial in two ways: (1) since the electron-phonon coupling parameters in bulk and in surface are generally different, the origin of the bands (that is to say the contributing weight is surface-derived, bulk-derived, or a surface resonance) should be clearly understood when the experimental results are to be compared to the *ab initio* calculation, (2) due to the finite resolution of ARPES, there arises, in some cases, overlap of the spectral intensities which can obscure the small renormalization of the electronic band dispersion [21]. Having the detailed picture of the band structure mapped by AREPS enables us to choose the appropriate band (not obscured by the band nearby) for the accurate characterization of the electron-phonon coupling parameters.

Figure 7.2a shows the experimental band structure of the clean Mo(112) substrate along the $\overline{\Gamma}-\overline{\mathrm{X}}$ line obtained by ARPES with the *p*-polarization geometry (after ref. [21]). Among the four bands seen to cross the Fermi level, the two bands with $k_F = 0.60$ and 0.81 Å^{-1} have been identified to be surface-derived, while the other two are projected bulk bands. As the surface of Mo(112) is covered by Au, the significant change in the band structure is observed. Figure 7.2b shows the experimental band structure of

Au/Mo(112) at the nominal Au coverage of 1 monolayer (1 ML) as schematically illustrated in Figure 7.1a. As is expected, the adsorption of Au monolayer results in the significant modification to the surface-derived bands of the Mo(112) substrate. While the surface band with k_F = 0.81 Å^{-1} is shifted towards the edge of the SBZ at k_F = 0.91 Å^{-1}, the other surface-derived band of Mo(112) at k_F = 0.60 Å^{-1} has disappeared from the ARPES spectrum. On the other hand, the bulk-derived bands are less affected upon Au adsorption. Although the projected Mo bulk band with k_F = 0.47 Å^{-1} is slightly shifted and ARPES intensity diminishes within 0.5 eV from E_F (relative to the rest portion of the band), the general features of dispersion remain unchanged. The dispersion of the other Mo bulk band with k_F = 0.64 Å^{-1} is more significantly affected by the Au adsorption as can be seen from the 'bending' of the dispersion and the enhancement of the ARPES intensity near 0.8 eV. Thus, it is experimentally evident that the adsorption of Au monolayer results in modification of the band structure of Mo(112) not only for its surface-derived states but also for the projected bulk states.

It is important to note that the modification of the surface potential induced by the Au adsorption should quickly diminish into the bulk of Mo(112) due to the screening in metal substrate and therefore, the observed change in the projected bulk band structure should not be directly attributed to the change in the surface potential. The noticeable modification in the projected bulk states should therefore be derived from the hybridization with the electronic states of Au overlayer. Consequently, it is plausible to expect that the observed bands with k_F = 0.51 and 0.64 Å^{-1} are surface resonance bands which have large weight (i.e., amplitude of the wave function) near the surface and penetrates into the Mo bulk with non-negligible amplitude.

This view is consistent with the theoretical expectations. Figure 7.2d shows the band structure of free-standing Au monolayer (detached from Mo(112) surface as in Figure 7.1a) plotted along the $\overline{\Gamma}-\overline{X}$ direction. In this plot, the band that crosses the Fermi level at k_F = 0.64 Å^{-1} is apparent and it is seen to exhibit nearly parabolic dispersion down to ~500 meV. Due to the presence of projected bulk continuum of Mo(112) in this region [21], this Au band is expected to form a surface resonance band upon adsorption on the Mo(112) surface. Figure 7.2c shows the calculated surface band structure of 1 ML Au/Mo(112) based on the 7-layer slab model overlaid on the ARPES spectrum shown in Figure 7.2b. The expected surface resonance band appears with k_F = 0.66 Å^{-1} and its dispersion is also modified. The calculation indicates noticeable surface weight for this band (~52%) as well as for the two bands seen to cross the Fermi level in ARPES spectrum. Thus, the band with k_F = 0.66 Å^{-1} (0.64 Å^{-1} in ARPES) is most likely identified as surface resonance arising from the hybridization between the Au overlayer states and the projected bulk states on Mo(112).

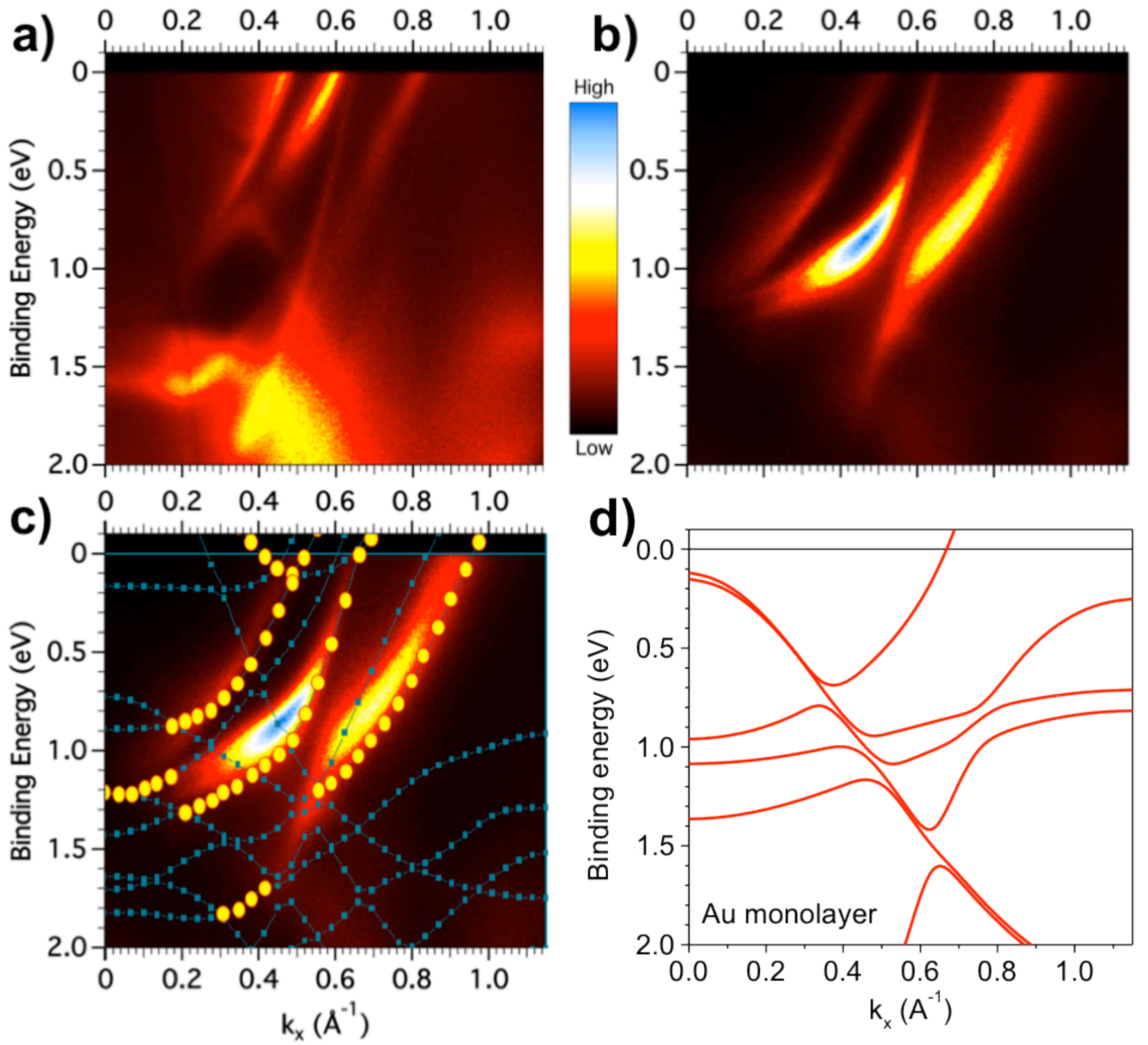

Figure 7.2: The ARPES band mapping taken along the $\bar{\Gamma}-\bar{X}$ line with the incident photon energy of 22 eV with p-polarization geometry (i.e., only the states with even reflection-parity about $\bar{\Gamma}-\bar{X}$ are visible) for (a) Mo(112) (reprinted from [21]) and, (b) 1 ML Au/Mo(112). The band structure calculated from the 7-layer slab model are overlaid for 1 ML Au/Mo(112) in (c). For (c), the significantly surface-weighted states with even reflection-parity are marked with yellow circles (●). (d) shows the band structure along $\bar{\Gamma}-\bar{X}$ line of free-standing monolayer of Au with the same structure as the topmost layer of Mo(112). The band with a Fermi level crossing of $k_F = 0.64$ Å^{-1} can be identified and is expected to hybridize with the Mo bulk state with nearly the same Fermi momentum k_F.

7.5. Electron-phonon coupling

The presence of the surface resonance states on Au/Mo(112) resulting from the hybridization of the Mo bulk states with the surface states on Au overlayer makes the system ideal for investigating the effect of adsorption on the strength of electron-phonon coupling. So far, several experimental and theoretical studies have been devoted to the characterization of the electron-phonon coupling parameters of the bulk as well as surfaces of Mo [4,17,18,33]. In particular, the mass enhancement parameter due to the electron-phonon coupling for Mo bulk is calculated to be $\lambda = 0.39\text{-}0.42$ [18,33], which is in agreement with the experimental identification of $\lambda = 0.42$ for the bulk-weighted band [17,21]. The electron-phonon coupling parameters λ for Mo(110) and Mo(112) are also reported [4,18] and are summarized in Table 7.1. Thus, there are fairly consistent characterizations of the electron-phonon coupling parameters for the Mo substrate.

In the present study, the theoretical and experimental investigations of the electron-phonon coupling parameters for 1 ML Au/Mo(112) have been carried out and are compared to those of clean Mo substrate. Here, the band with $k_F = 0.64$ Å^{-1} (see Figure 7.2b) is analyzed with MDC method described above with the energy increment of 1.5 meV to extract the peak positions (k_{peak}) as well as the linewidth (Γ). Figure 7.3a shows the ARPES spectrum of the analyzed band within 150 meV from EF. The MDC peak positions as well as the expected bare dispersion (broken curve fitted by parabola with the fixed k_F determined from the experiment) are overlaid. The distortion of the band within ~50 meV below E_F, characteristic of the electron-phonon coupling, is apparent. The parabolic fit shows an excellent match down to at least 500 meV and is given by

$$E(k) = -17.666k^2 + 14.404k - 1.9828, \quad (7.1)$$

where E and k are measured in units of eV and $Å^{-1}$ respectively.

Figure 7.4 shows the calculated phonon density of states $F(\omega)$ and the phonon band structure. The electron-phonon coupling function $\alpha^2(\omega)$ are calculated as outlined in sec. 7.3 and it gives the Eliashberg function $\alpha^2(\omega)F(\omega)$ shown as solid curve in Figure 7.4. Given the Eliashberg function, the spectral function can be calculated using the experimentally determined bare dispersion $E(k)$ given by (7.1) and the broadening due to the electron-impurity coupling (whose value is estimated below) as shown in Figure 7.3b. The calculated MDC peak positions are shown as the solid curve. In the present simulation, the finite energy resolution and the self-energy due to the electron-electron coupling are not included. As described below the electron-electron coupling is not significant near E_F. In Figure 7.3b, the experimental MDC peak positions are also indicated and are in good agreement with the calculated spectral function. Figure 7.3c shows the calculated spectral function with electron-impurity coupling "turned off", in which the agreement between the experimental MDC peak positions and the characteristic distortion due to electron-phonon coupling is more clearly seen.

In order to get further quantitative insights into the self-energy due to electron-phonon coupling, the experimental self-energy is extracted using the equation (5.18) with the group velocity $v = -35.332k + 14.404$ eV/$Å^{-1}$ and are compared to the calculated self-energy at $T = 60$ K (solid curves) as in Figure 7.5. It can be seen that the real part (Figure 7.5a) shows reasonable agreement between the theory and the experiment (note that in the binding energy scale as employed here, Σ_R is negative for the occupied states). The imaginary part in Figure 7.5b also gives a good agreement provided that the calculated Σ_I is rigidly shifted up by 171 meV, corresponding to the electron-impurity coupling and the instrumental broadening of the MDC linewidth. Since the MCD width at E_F is evaluated to be ~0.022 Å^{-1} and the instrumental angular resolution is estimated to be 0.2° (or in *k*-space ~0.008 Å^{-1}), the broadening due to the electron-impurity coupling can be estimated as ~0.019 Å^{-1} (note that the electron-impurity coupling gives Lorentzian lineshape and the instrumental broadening is modeled by Gaussian lineshape). Thus, the self-energy contribution from the electron-impurity coupling can be estimated as $2\Sigma^{(e\text{-}i)}{}_I$ ~156 meV. Note that the electron-impurity coupling only affects the lifetime of the quasiparticle and hence $\Sigma^{(e\text{-}i)}{}_R = 0$.

Here, it is important to mention that since the analyzed band is a surface resonance, the hybridization of local (surface) state of Au with the Mo bulk continuum may cause the linewidth broadening. However, given the agreement of the experimental and calculated self-energy due to electron-phonon coupling and the internal consistency between experimental Σ_R and Σ_I (related by the Kramers-Kronig relation (5.14)), the linewidth broadening due to such hybridization is either negligible or nearly constant within the small window of 150 meV below E_F. Thus, some portion of the estimated $2\Sigma^{(e\text{-}i)}{}_I$ ~156 meV may be due to the bulk-surface hybridization. Note that the real part of self-energy due to hybridization is already accounted for in the 'unrenormalized' parabolic fit in Figure 7.3a and thus expected to give negligible alteration in Figure 7.5a.

Another scattering mechanism, electron-electron coupling is expected to give rise to the self-energy $\Sigma^{(e\text{-}e)}$ with the monotonic increase in $|2\Sigma^{(e\text{-}e)}{}_I|$ as a function of binding energy [14,34,35] and is observed in various metallic systems including Mo [17]. For

Au/Mo(112), as can be seen from the essentially constant imaginary part in Figure 7.5b ($2\Sigma_I \sim 210$ meV for $E > 50$ meV), $\Sigma^{(e\text{-}e)}$ appears to be dominated by $\Sigma^{(e\text{-}p)}$ and $\Sigma^{(e\text{-}i)}$ and the contribution from $\Sigma^{(e\text{-}e)}$ is likely rather small, which is in contrast to Mo substrate [17].

From the point of view of anisotropy of the system, it is rather surprising that the experimentally extracted $\Sigma^{(e\text{-}p)}$ for a specific band gives a good agreement with that calculated by averaging over all the possible k_i and k_f. Such a calculation gives identical $\Sigma^{(e\text{-}p)}$ values for all the bands in the entire SBZ, whereas in general it should be different for each band. Either that the structural and electronic anisotropy of 1 ML Au/Mo(112) is not significant enough to cause major anisotropy in electron-phonon coupling (to the degree it can be readily identified in the scale of Figure 7.5), or the band chosen for this particular analysis "coincidentally" agrees very well with the homogeneous (or averaged) model of electron-phonon coupling, in spite of the anisotropic electronic structure [21].

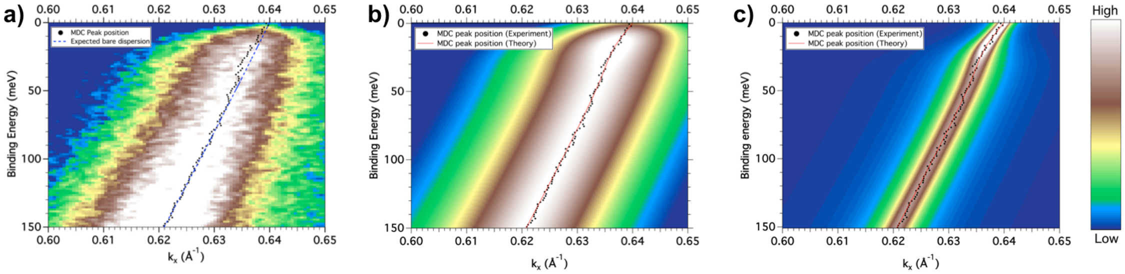

Figure 7.3: (a) The ARPES spectrum taken along the $\bar{\Gamma}-\bar{X}$ line in the vicinity of the Fermi level. The surface resonance band with $k_F = 0.64$ Å^{-1} can be identified to exhibit the renormalization due to electron-phonon coupling within ~50 meV below the Fermi level. The peak positions obtained in MDCs are indicated with circles (●) and the expected unrenormalized band dispersion is indicated with blue broken curve. (b) The spectral function weighted with the Fermi function at $T = 60$ K in the vicinity of Fermi level calculated from the theoretically determined Eliashberg function and experimentally determined bare band dispersion $E(k)$ and the impurity scattering rate (estimated to be ~78 meV contribution to Σ_I). The MDC peak positions (●) determined from ARPES is overlaid for the comparison and are seen to agree well with the theoretically expected renormalization. The peaks of the calculated spectral functions are shown in red solid

curve as a visual guide. (c) The calculated spectral function in which impurity scattering is turned off (band renormalization is solely due to electron-phonon coupling). The agreement between the ARPES-determined MDC peak positions (●) and the calculated band distortion is more apparent. Note that the Fermi edge cut-off at finite temperature (60 K) is also turned off for the visual clarity.

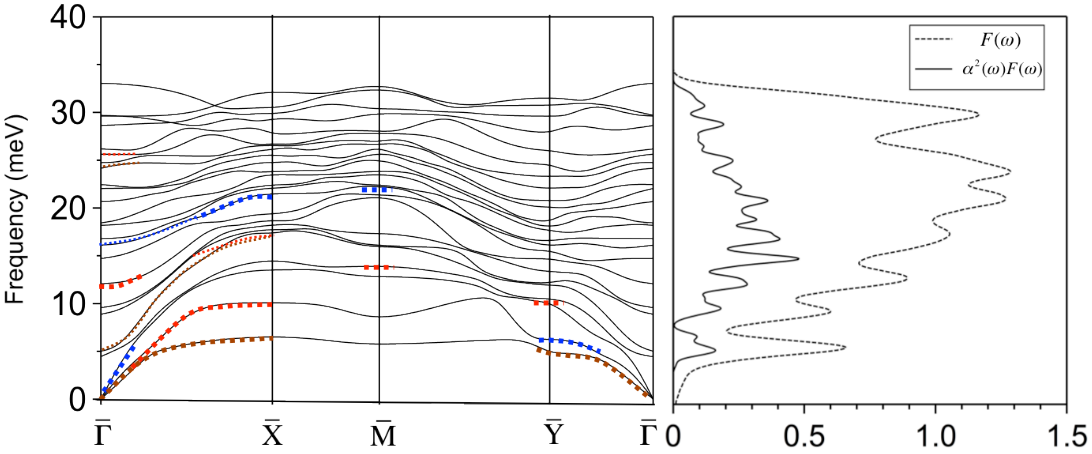

Figure 7.4: The phonon band structure calculated using the 7-layer slab model is shown in (a), where the surface-weighted modes are marked with thick dotted line (blue = longitudinal mode; red = vertical mode; brown = horizontal mode). Isotropic Eliashberg function, $\alpha^2F(\omega)$, calculated from the 7-layer slab model is shown in (b). Note that the Eliashberg function is dimensionless.

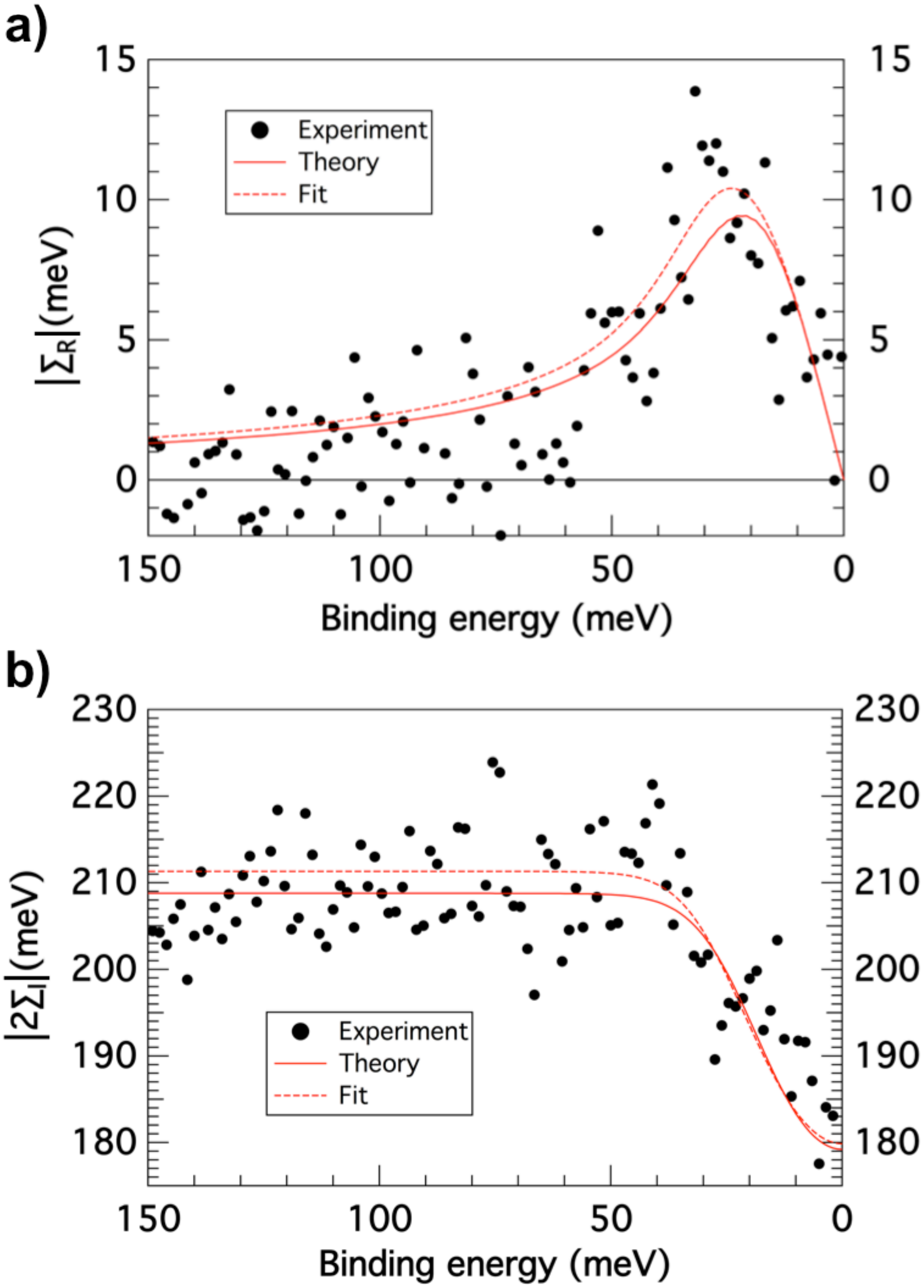

Figure 7.5: The real part (a), and the imaginary part (b) of self-energy for the surface resonance band with $k_F = 0.64$ Å^{-1}. The experimental data points (●) for Σ_R are obtained from the deviation of the ARPES peak positions from the expected unrenormalized band dispersion (see Figure 7.3a) and those for Σ_I are obtained from the (energy) width of the photoemission peaks as described in the text. For the theoretical part, the self-energy due to electron-phonon coupling are obtained from the calculated isotropic Eliashberg function at $T = 60$ K and plotted as solid curves. The calculated Σ_I is rigidly shifted up by

171 meV so as to fit the experimental data (interpreted as deriving from the electron-impurity coupling and instrumental broadening as discussed in text). The dotted curves represent the self-energy obtained from the free-parameter Eliashberg function that gives the best fit to the experimental data.

	Mass enhancement parameter $\lambda(T = 0)$	
	Theory	**Experiment**
Mo bulk	**0.39 – 0.42** [18,33]	**0.42** [17]
Mo(110)		**0.42-0.52** [4]
Mo(112)	**0.46** [18]	
Au/Mo(112)	**0.68 (0.67 at 60 K)**	**0.70 (0.65 at 60 K)**

Table 7.1: The mass enhancement parameters for bulk Mo as well as its various surfaces. The listed values are evaluated at $T = 0$ unless otherwise specified.

7.6. Important modes of coupling

Given the electron-phonon coupling near the interface of Au/Mo(112), it is worthwhile to explore qualitatively the important modes of coupling (i.e., which phonon modes may be giving rise to the major contribution to $\Sigma^{(e\text{-}p)}$) for the observed band with $k_F = 0.64$ Å^{-1}. Note that the low energy phonon modes contribute more significantly to the self-energy than those lying at higher energy. This can be seen from the fact that the electron-phonon coupling matrix element is proportional to $\omega^{-1/2}$ (see (A.5) in Appendix A). In fact, it has been pointed out that the contributions from the acoustic phonon modes (or Rayleigh modes) give dominant contribution to the electron-phonon coupling at the surface of Cu(111), Ag(111) and Au(111) [8,9]. In Figure 7.4, among the surface phonon modes for the $\overline{\Gamma}-\overline{X}$ line (marked by colored squares) the surface acoustic modes (shear horizontal modes in brown and vertical modes in red) lie well below the bulk band edge and produces the pronounced peaks at 5 and 9 meV in the phonon density of states $F(\omega)$. However, along the $\overline{\Gamma}-\overline{X}$ line, the symmetry of the electronic states and the phonon modes restricts the possible coupling modes. Since the electronic states and phonon modes lying along $\overline{\Gamma}-\overline{X}$ are described by C_{1h} group, they can be classified as either even (A' irreducible representation) or odd (A") with respect to the reflection about $\overline{\Gamma}-\overline{X}$ line. Since experimental band mapping in Figure 7.2b as well as Figure 7.3a are taken with *p*-polarization geometry, in which vector potential of the incident light lies within *xz*-plane (see Figure 7.1a), according to the dipole selection rules [36], the electronic bands analyzed for the electron-phonon coupling is of even symmetry (A'). On the other hand, the symmetry properties of phonons are classified by their polarizations. It can be derived for the group of C_{1h}, under certain reasonable approximations, that the electron-phonon coupling matrix element vanishes unless the electronic state and phonon mode are both even or both odd (the detailed derivations are summarized in Appendix A). Thus, the shear horizontal phonon modes (marked brown) are forbidden to couple with the electrons in the analyzed band. Although this selection rule is valid only along the $\overline{\Gamma}-\overline{X}$ line, the coupling matrix element is usually small near this high-symmetry line if it vanishes along it. One can therefore expect that shear horizontal modes contribute less to the observed self-energy than do the shear vertical modes. This leads to the inference that besides the bulk phonon contribution, the surface phonons, particularly shear vertical modes play an important role in the observed electron-phonon coupling.

7.7. Enhancement of electron-phonon coupling

The mass enhancement parameter $\lambda(T)$ is important in characterizing the electron-phonon coupling strength. In the present study, λ estimated from the calculated Eliashberg function gives $\lambda(T = 0) = 0.68$ and $\lambda(T = 60\text{ K}) = 0.67$. The experimental extraction of $\lambda(T)$ involves some difficulty as the slope of $\Sigma^{(e-p)}{}_R(\omega)$ with respect ω must be evaluated right at E_F, around which the ARPES intensity is diminished proportional to the Fermi function. In order to overcome this difficulty, we fit the experimental $\Sigma_R(\omega)$ using the free-parameter Eliashberg function $\alpha^2F(\omega)$, in which α^2 is taken to be the energy-independent free parameter, and extract λ associated with the $\alpha^2F(\omega)$ which gives the best fit for both $\Sigma_R(\omega)$ and $\Sigma_I(\omega)$.

The dotted curves in Figure 7.5 shows the self-energy extracted from the free-parameter Eliashberg function with $\alpha^2 = 0.23$. This fit gives a better overall match with the experimental data points (particularly for $\Sigma_R(\omega)$). Given this free-parameter Eliashberg function, the λ can be estimated as 0.70 at $T = 0$ and 0.65 at $T = 60$ K, providing fairly good agreement between the theory and the experiment. This is consistent with the overall agreement between the theory and the experiment obtained for the mass enhancement parameter λ, as summarized in Table 7.1.

The λ of 1 ML Au/Mo(112) should now be compared to that of the Mo substrate. Although the combination of theory and experiment gives the range of $\lambda = 0.68 – 0.70$, it is evidently larger than $\lambda = 0.39 - 0.42$ for Mo bulk and $\lambda = 0.42$ for Mo(112) surface as identified in the previous studies (see Table 7.1). It is plausible to argue that adsorption of Au on Mo(112) enhances the electron-phonon coupling. Such an increase in λ can be viewed as a direct consequence of the soft Au phonon contributions to the modes of coupling. Thus, the addition of soft phonon modes by means of adsorption does affect the electron-phonon coupling parameter and the quasiparticle effective mass.

7.8. Summary

The investigation of the electronic structure and the electron-phonon coupling parameters of Au/Mo(112), at the nominal coverage of 1 ML of Au, has been performed by means of high-resolution ARPES and DFT calculations. The adsorption of Au modifies the electronic band structure of Mo(112) and the details of the band structure indicates the hybridization occurs between the projected bulk electronic states of Mo(112) and those of Au overlayer. The detailed analysis of the ARPES spectrum leads to the quantitative evaluations of the many-body interactions in terms of electron-phonon, electron-electron and electron-impurity coupling near the interface of Au/Mo(112) and suggests that the electron-phonon coupling gives the dominant contribution to the self-energy of quasiparticles. In spite of the appreciable structural and electronic anisotropy of Au/Mo(112), the DFT calculation of the *k*-averaged Eliashberg function yields the self-energy due to electron-phonon coupling in good agreement with the particular *k* point along $\overline{\Gamma}-\overline{\mathrm{X}}$ in the experiment. Given the change in the quasiparticle self-energy upon Au adsorption on Mo(112), the Au overlayer enhances the strength of electron-phonon coupling at E_F (from 0.39-0.42 to 0.68-0.70) and noticeably suppresses the electron-electron interaction. The enhancement of electron-phonon coupling likely derives from the creation of the soft surface phonon modes upon Au adsorption.

References

[1] G. Grimvall, *The Electron-Phonon Interaction in Metals* (Selected Topics in Solid State Physics XVI), 1st ed. (Elsevier Science Ltd, 1981).

[2] P. Hofmann, I. Y. Sklyadneva, E. D. L. Rienks, and E. V. Chulkov, *New J. Phys.* **11**, 125005 (2009).

[3] J. Kroger, *Rep. Prog. Phys.* **69**, 899 (2006).

[4] T. Valla, A. Fedorov, P. Johnson, and S. Hulbert, *Phys. Rev. Lett.* **83**, 2085 (1999).

[5] T. Balasubramanian, E. Jensen, X. L. Wu, and S. L. Hulbert, *Phys. Rev.* B **57**, 6866 (1998).

[6] A. Eiguren, S. de Gironcoli, E. Chulkov, P. Echenique, and E. Tosatti, *Phys. Rev. Lett.* **91**, 166803 (2003).

[7] S. Lashell, E. Jensen, and T. Balasubramanian, *Phys. Rev.* B **61**, 2371 (2000).

[8] A. Eiguren, B. Hellsing, E. Chulkov, and P. Echenique, *Phys. Rev.* B **67**, 235423 (2003).

[9] A. Eiguren, B. Hellsing, F. Reinert, G. Nicolay, E. Chulkov, V. Silkin, S. Hüfner, and P. Echenique, *Phys. Rev. Lett.* **88**, 066805 (2002).

[10] B. McDougall, T. Balasubramanian, and E. Jensen, *Phys. Rev.* B **51**, 13891 (1995).

[11] F. Reinert, G. Nicolay, S. Schmidt, D. Ehm, and S. Hüfner, *Phys. Rev.* B **63**, 115415 (2001).

[12] X. Y. Cui, K. Shimada, M. Hoesch, Y. Sakisaka, H. Kato, Y. Aiura, M. Higashiguchi, Y. Miura, H. Namatame, and M. Taniguchi, *Surface Science* **601**,

4010 (2007).

[13] X. Cui, K. Shimada, Y. Sakisaka, H. Kato, M. Hoesch, T. Oguchi, Y. Aiura, H. Namatame, and M. Taniguchi, *Phys. Rev. B* **82**, 195132 (2010).

[14] J. Jiang, M. Higashiguchi, N. Tobida, K. Tanaka, S. Fukuda, H. Hayashi, K. Shimada, H. Namatame, and M. Taniguchi, *E-J. Surf. Sci. Nanotech.* **7**, 57 (2009).

[15] M. Jensen, T. Kim, S. Bengió, I. Sklyadneva, A. Leonardo, S. Eremeev, E. Chulkov, and P. Hofmann, *Phys. Rev.* B **75**, 153404 (2007).

[16] J. Jiang, K. Shimada, H. Hayashi, H. Iwasawa, Y. Aiura, H. Namatame, and M. Taniguchi, *Phys. Rev.* B **84**, 155124 (2011)

[17] N. Wu, Y. B. Losovyj, K. Fukutani, and P. A. Dowben, *J. Phys.: Condens. Matter* **22**, 245501 (2010).

[18] I. Yakovkin and P. Dowben, *J. Phys.: Condens. Matter* **23**, 225503 (2011).

[19] E. Rotenberg and S. Kevan, *Journal of Electron Spectroscopy and Related Phenomena* **126**, 125 (2002).

[20] E. Rotenberg, J. Schaefer, and S. D. Kevan, *Phys. Rev. Lett.* **84**, 2925 (2000).

[21] K. Fukutani, H. Hayashi, I. N. Yakovkin, T. R. Paudel, T. Habuchi, D. Hirayama, J. Jiang, H. Iwasawa, K. Shimada, N. Wu, E. Y. Tsymbal, Y. B. Losovyj, and P. A. Dowben, *Phys. Rev.* B **85**, 155435 (2012).

[22] K. Fukutani, N. Lozova, S. M. Zuber, P. A. Dowben, P. Galiy, and Y. B. Losovyj, *Applied Surface Science* **256**, 4796 (2010).

[23] K. Shimada, M. Arita, Y. Takeda, H. Fujino, K. Kobayashi, T. Narimura, H. Namatame, and M. Taniguchi, *Surf. Rev. Lett.* **9**, 529 (2002).

[24] T. McAvoy, J. Zhang, C. Waldfried, D. McIlroy, P. Dowben, O. Zeybek, T. Bertrams, and S. Barrett, *Eur. Phys. J.* B **14**, 747 (2000).

[25] I. Yakovkin, J. Zhang, and P. Dowben, *Phys. Rev.* B **63**, 115408 (2001).

[26] H. K. Jeong, T. Komesu, I. N. Yakovkin, and P. Dowben, *Surface Science Letters* **494**, L773 (2001).

[27] N. Wu, Y. B. Losovyj, Z. Yu, R. F. Sabirianov, W. N. Mei, N. Lozova, J. A. Colón Santana, and P. A. Dowben, *J. Phys.: Condens. Matter* **21**, 474222 (2009).

[28] K. Fukutani, Y. B. Losovyj, N. Lozova, I. N. Yakovkin, N. Wu, and P. A. Dowben, *Journal of Electron Spectroscopy and Related Phenomena* **184**, 318 (2011).

[29] T. Gallon and J. Matthew, *Review of Physics in Technology* **3**, 31 (1972).

[30] J.P. Perdew, K. Burke, and M. Ernzerhof, *Phys. Rev. Lett.* **77**, 3865 (1996).

[31] X. Gonze, J.-M. Beuken, R. Caracas, F. Detraux, M. Fuchs, G.-M. Rignanese, L. Sindic, M. Verstraete, G. Zerah, F. Jollet, M. Torrent, A. Roy, M. Mikami, Ph. Ghosez, J.-Y. Raty, and D.C. Allan, *Comput. Mat. Sci.* **25**, 478 (2002).

[32] N. Troullier and J.L. Martins, *Phys. Rev.* B **43**, 1993 (1991).

[33] S.Y. Savrasov and D.Y. Savrasov *Phys. Rev.* **B 54,** 16487 (1996).

[34] M. Higashiguchi, K. Shimada, M. Arita, Y. Miura, N. Tobita, X. Cui, Y. Aiura, H. Namatame, and M. Taniguchi, *Surface Science* **601**, 4005 (2007).

[35] C. Hodges and J. Wilkins, *Phys. Rev. B* **4**, 302 (1971).

[36] J. Harmanson, *Solid State Communications* **22**, 9 (1977).

Chapter 8
Fermi surface of (4x1) Au/Mo(112) and structural instability

8.1 Motivation

Electron-phonon coupling plays an important role in various types of phase transitions [1]. In one-dimension, the divergence of electronic susceptibility function leads to periodic lattice distortion well known as Peierls transition [2] and subsequent formation of charge density wave (CDW). Such transition occurs at finite temperature due to the perfect nesting condition on the Fermi surface in one-dimension. In two-dimension, several transition metal dichalcogenides are reported to undergo periodic lattice distortion induced by the strong, but not perfect, nesting condition in their Fermi surface topology [3-5]. The recent studies, presented above, have shown that the Au overlayer on Mo(112) surface exhibits significant electron-phonon coupling involving its surface resonance states [6]. Due to the highly anisotropic electronic structure of Mo(112) [7] and the quasi-one-dimensional properties of its Fermi surface [8] to which the electronic states of Au overlayer is strongly coupled, the electronic susceptibility of Au overlayer can exhibit lattice instability due to the strong phonon nesting. We explore the interplay between the strong electron-phonon coupling and its nesting properties, as determined by the topology of the Fermi surface.

8.2 Charge density wave and lattice instability

When electrons in solids are subject to perturbation (e.g., applied fields, ionic vibrations etc.), they respond in certain way to minimize their energy. Within the linear response theory (see e.g., ref. [9]), the induced charge (due to the perturbation) is given by

$$\rho_{ind}(r,t) = \int dr' \int_{-\infty}^{\infty} dt' \chi(r,t;r',t') \phi_{ext}(r',t') \ , \tag{8.1a}$$

or in energy-momentum space

$$\rho_{ind}(q,\omega) = \chi(q,\omega)\phi_{ext}(q,\omega) \quad , \tag{8.1b}$$

where ϕ_{ext} is the 'external' perturbation potential and χ is called susceptibility function, which describes how the system of many-electrons will respond to the applied perturbation. For simplicity, if we assume the non-interacting electron system (or Fermi gas, in which there is no 'internal' interaction), the susceptibility function χ can be calculated as

$$\chi(q,\omega) = \sum_k \frac{n_f(E_k) - n_f(E_{k+q})}{E_k - E_{k+q} + \omega + i\eta} \ , \tag{8.2}$$

where n_f is Fermi distribution function, q and ω are the momentum and frequency of excitation, respectively (i.e., the response of electrons to the q-th Fourier component of time-dependent external potential with frequency ω). The expression (8.2) is called Lindhard response function. Of course, the non-interacting electron system is a crude model, and it is possible and conventional to include the Coulomb interactions etc. within the random phase approximation (RPA). However, in arriving at the qualitative (or semi-quantitative) conclusion of this section, use of the non-interacting model is not a severe restriction. In the static limit $\omega = 0$, we have, for the real part of Lindhard response function,

$$\chi(q,\omega=0)=\sum_k \frac{n_f(E_k)-n_f(E_{k+q})}{E_k-E_{k+q}} . \tag{8.3}$$

For electron-phonon coupling, in which phonons provide the perturbation to the many-electron system, it is reasonable to adopt the above static limit due to the generally small frequency of phonons ($\omega \sim 10$ meV). The Lindhard function (8.3) for the non-interacting electron system is shown in Figure 8.1 for one-, two- and three-dimensions. It is seen that the Lindhard function in one-dimension exhibits a singularity at $q = 2k_F$. This means, mathematically, the Fourier component of the electronic charge density with $q = 2k_F$ diverges, and it physically means the system of electrons becomes unstable against the formation of the periodic electron density modulation of with wavelength $\lambda = \pi/k_F$. This is called a charge density wave (CDW). Formation of the CDW in one-dimension is a direct consequence of the Fermi surface of electrons in one-dimension, which consists of two points at k_F and $-k_F$. The phonons of wave vector $2k_F$, which provide the critical perturbation, span these two points on the one-dimensional Fermi surface and said to be a nesting phonon. Since in one-dimension all the phonon modes with $q = 2k_F$ can provide the critical perturbation to the many-electron system, such Fermi surface (two points at $-k_F$ and k_F) are said to satisfy the *perfect nesting condition*. Such nesting condition not only affects the electrons, but also the phonons. In particular, the frequency of phonon is renormalized due to the ‘rearrangement’ of surrounding electrons and is given by, within the mean field approximation,

$$\omega_{ren}^2(q)=\omega^2(q)+2g^2\omega(q)\chi(q;T), \tag{8.4}$$

where g is called the electron-phonon coupling constant (not to be confused with the electron-phonon coupling parameter λ), which is a pure imaginary quantity (i.e., $\omega_{ren} <$

ω). Thus, near the $2k_F$, the renormalized phonon frequency dips significantly (in fact, it becomes imaginary) in a purely one-dimensional system. At this point, the phonon of wave vector $2k_F$ freezes and the lattice becomes distorted with the new periodicity given by π/k_F. Such lattice distortion accompanied by the electronic CDW formation in one-dimension is called the Peierls transition [2]. The perfect nesting condition breaks down in two- and three-dimensions and the formation of CDW does not necessarily occur. However, if the coupling of electrons with phonons is strong enough and the Fermi surface exhibits strong (even if not perfect) nesting conditions, the CDW formation does in fact occur and has been observed. The criterion for the lattice instability is proposed to be [10]

$$4\overline{M}(q)^2/\omega(q) - 2\overline{U}(q) + \overline{V}(q) \geq 1/\chi(q), \qquad (8.5)$$

where $\overline{M}$ is the electron-phonon coupling matrix element, $\overline{U}(q) = \langle k+q, k' | U | k'+q, k \rangle$ is the direct Coulomb interaction matrix element, and $\overline{V}(q) = \langle k+q, k' | V | k, k'+q \rangle$ is the exchange Coulomb interaction matrix element. In this simplified view, it can be seen that, for any given q, the instability condition is more likely to be met with higher electronic response $\chi(q)$ and stronger electron-phonon coupling $\overline{M}(q)$.

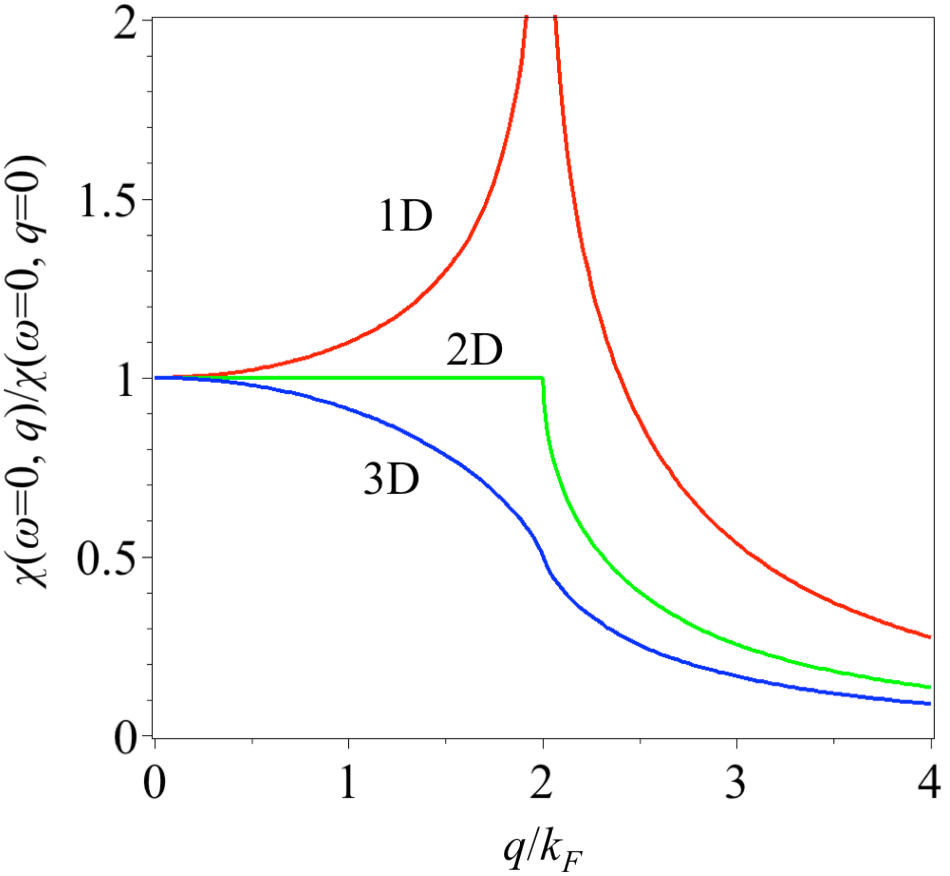

Figure 8.1: The Lindhard response function in the static limit ($\omega = 0$) for the three-, two- and one-dimensional Fermi gas (normalized to the value at $q = 0$). Peculiar features can be identified at $q = 2k_F$ in each dimension. The derivative of electronic response diverges in three-dimension, it is discontinuous in two-dimension, and the electronic response itself is divergent in one-dimension.

8.3 Experimental details

The surface of the Mo(112) sample was cleaned by the standard method of repeated annealing (at ~1400° C) in oxygen atmosphere with the oxygen partial pressure of ~1×10^{-6} torr, followed by cycles of annealing (at 1000-1300° C) and flashing (at ~1800°C) as described in section 4.1. Low energy electron diffraction (LEED) and Auger electron spectroscopy (AES) were used to verify the quality of the Mo(112) surface, including the periodic structural order. The amount of surface contamination, such as C and O, were evaluated to be below the detection limit of the AES. The deposition of Au was performed by the method described in section 4.2 to obtain the coverage of 1.75 ML. The corresponding LEED image and the schematic of the overlayer structure are illustrated in Figure 4.2d.

The high-resolution ARPES was performed at the linear undulator beamline (BL-1) [11] of Hiroshima Synchrotron Radiation Center (HiSOR) at Hiroshima University, Japan. The experiments were carried out using an angular (display) mode of the hemispherical electron analyzer (R4000, VG Scienta), with the acceptance angle of ±15°. The Fermi contour mapping was performed at the incident photon energy of $\hbar\omega = 50$ eV by rotating the sample in its surface plane by increments of 2°, using incident photon sources with both *p*-polarization geometries (the vector potential of the incident light is 50° with respect to the surface normal). The band mapping along the $\bar{\Gamma}-\bar{X}$ high symmetry direction was also performed with *p*-polarization geometry (with the vector potential lying 40° with respect to the surface normal). For both the Fermi contour mapping and the band mapping taken for a photon energy of 50 eV, the energy resolution was estimated to be ~18 meV and the angular resolution was ~0.3°, corresponding to a wave vector resolution of ~0.018 Å^{-1} at the Fermi level.

Throughout the experiment, the sample was maintained at the desired temperature by the combination of automated flow of liquid helium and heating of the filament behind the sample.

8.4 Temperature-dependent Fermi surface of (4x1) Au/Mo(112)

Figure 8.2 shows the Fermi surface contours of (4x1) Au/Mo(112) observed at 60 K. A number of distinct features can be identified on this Fermi surface mapping. The half-rectangular ‘box’ around $\overline{\Gamma}$ derives from the surface resonance states created upon Au adsorption [6] and the contour shaped like ‘$\subset$’ near $\overline{X}$ along the $\overline{\Gamma}-\overline{X}$ line derives from the bulk Mo Fermi surface.

Of particular importance is the vertical segment of the half-rectangle box (crossing the $\overline{\Gamma}-\overline{X}$ line at ~0.47 Å^{-1}). The Fermi contour for this segment was extracted from the peak fitting and shown in Figure 8.3 for five different temperatures. It can be seen that this segment exhibits noticeable temperature dependence, particularly within the range of 230-330 K. At low temperature, it is seen to be ‘convex’ (curving away from $\overline{\Gamma}$) up to at least 230 K. However, it can be seen that this segment is observed to be nearly straight, or perhaps slightly concave, (curving towards $\overline{\Gamma}$) at 290 K, which indicates the change in this Fermi surface segment between the temperature of 230 K and 290 K. Upon further increase of the temperature, this Fermi surface segment is, again, seen to exhibit the convex curvature, as can be seen for 330 K, showing that the change in Fermi contour is non-monotonic.

Although the detailed origin of such changes in the Fermi contour on Au/Mo(112) is not unambiguously determined, since the nesting condition is determined by the topology of the Fermi surface, the observed change in the Fermi surface segment will affect the surface phonon nesting properties on Au/Mo(112). In order to understand how the observed change in the Fermi contour may affect the nesting properties on Au/Mo(112), we note that the straight parallel Fermi contour segments give rise to the pronounced peak in the Lindhard function [1]. Thus, it is likely that as the Fermi surface segment flattens near 290 K, the Lindhard function becomes more and more peaked at the wave vector $2k_F = k_{F1} + k_{F2}$. As mentioned above, such pronounced response of electrons at $2k_F$, in turn, gives rise to the softening of the phonon mode (Kohn anomaly). It is not clear whether the instability condition (8.5) is met near 290 K. However, it is clear that the observed change of Fermi surface contour for the surface resonance states of (4x1) Au/Mo(112) near 290 K favors the stronger nesting condition and that the electron-phonon coupling is strongly enhanced on Au/Mo(112) as a result of Au adsorption, as presented in previous chapter. Therefore, it is plausible to speculate, based on the above facts uncovered in the course of this study, that combination of strong electron-phonon coupling and temperature-dependent nesting conditions are responsible for some structural instability and/or phonon softening which occurs for the Au overlayer structure on Mo(112).

Furthermore, even if the nesting of the Fermi surface is not strong enough to induce lattice instability (i.e., the instability condition (8.5) is not met) near 290 K, as the changes of Fermi surface are seen to be non-monotonic and persisting above 290 K, it is not difficult to imagine that at certain temperature above 290 K, the Fermi surface again evolves in favor of stronger nesting condition thereby inducing some type of structural phase transition.

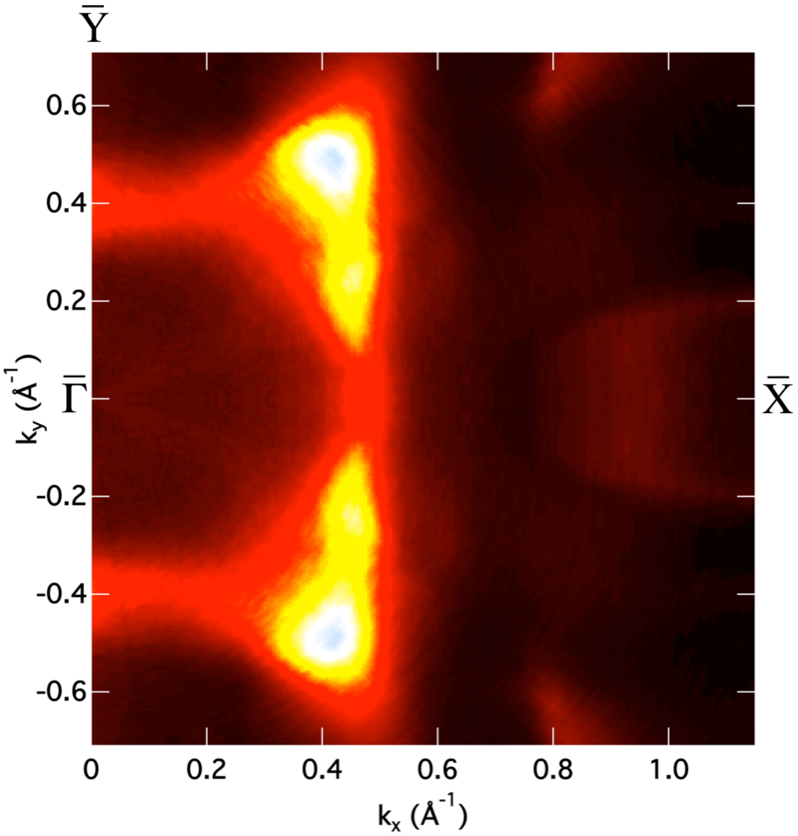

Figure 8.2: The Fermi surface contour mapping of (4x1) Au/Mo(112) within the SBZ. The high-symmetry points are labeled.

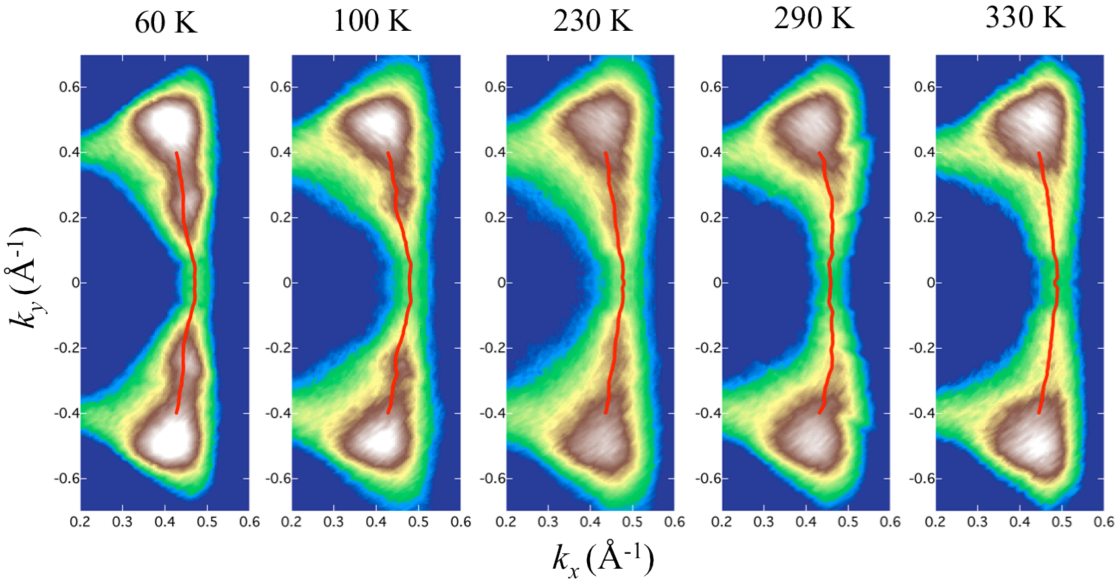

Figure 8.3: The temperature dependence of the segment of the Fermi surface. At low temperatures (60 – 100 K), this segment is seen to be convex and remains unchanged

(within the experimental error), but gradually flattens from ~230 K and becomes nearly straight at ~290 K. At 330 K, it is again seen to be convex.

8.5 Summary

We observed noticeable temperature dependence of the Fermi surface contours of (4x1) Au/Mo(112) by means of high-resolution angle-resolved photoemission spectroscopy. Within the temperature range of 60 K- 330 K, the vertical segment of the Fermi surface (parallel to $\langle 1\bar{1}0 \rangle$ direction), attributable to the surface resonance states, evolves in non-monotonic manner. Near 290 K, this vertical segment is seen to be nearly straight, which could cause the system to undergo the structural phase transition. The change in the Fermi surface persists above 290 K and possibly implies another lattice instability above 330 K.

References

[1] G. Gruner, *Density Waves in Solids* (Perseus Publishing, 1994) ISBN 0738203041.

[2] R. E. Peierls, *Quantum Theory of Solids* (Oxford University Press, 2001), ISBN 9780198507819.

[3] S.V. Borisenko, A.A. Kordyuk, A.N. Yaresko, V.B. Zabolotnyy, D.S. Inosov, R. Schuster, B. Buchner, R. Weber, R. Follath, L. Patthey and H. Berger, *Phys. Rev. Lett.* **100**, 196402 (2008).

[4] D.S. Inosov, D.V. Evtushinsky, V.B. Zabolotnyy, A.A. Kordyuk, B. Buchner, R. Follath, H. Berger and S.V. Borisenko, *Phys. Rev.* B **79**, 125112 (2009).

[5] D.S. Inosov, V.B. Zabolotnyy, D.V. Evtushinsky, A.A. Kordyuk, B. Buchner, R. Follath, H. Berger and S.V. Borisenko, *New Journal of Physics* **10**, 125027 (2008).

[6] K. Fukutani, H. Hayashi, I.N. Yakovkin, T. Habuchi, D. Hirayama, J. Jiang, H. Iwasawa, K. Shimada, Ya. B. Losovyj and P.A. Dowben, 'Enhanced Electron-Phonon Coupling at Au/Mo(112)' Submitted to *Phys. Rev.* B.

[7] K. Fukutani, H. Hayashi, I. N. Yakovkin, T. R. Paudel, T. Habuchi, D. Hirayama, J. Jiang, H. Iwasawa, K. Shimada, N. Wu, E. Y. Tsymbal, Y. B. Losovyj, and P. A. Dowben, *Phys. Rev.* B **85**, 155435 (2012).

[8] I. N. Yakovkin, K. Fukutani, H. Hayashi, J. Jiang, T. Horike, Y Nagata, T. Habuchi, D. Hirayama, H. Iwasawa, K. Shimada, Ya. B. Losovyj, and P. A. Dowben, *Phys. Rev.* B **85**, 155435 (2012).

[9] H. Bruus and K. Flensberg, *Many-Body Quantum Theory in Condensed Matter Physics* (Oxford University Press, 2004), ISBN 9780198566335.

[10] S-K Chan and V. Heine, *J. Phys.* F, **3**, 795 (1973).

[11] K. Shimada, M. Arita, Y. Takeda, H. Fujino, K. Kobayashi, T. Narimura, H. Namatame, and M. Taniguchi, *Surf. Rev. Lett.* **9**, 529 (2002).

Chapter 9
Order-disorder transition

9.1 Motivation

Lattice distortions, including both longitudinal distortions (a Peierls distortion) and transverse distortions (a transverse Peierls distortion) have been predicted to occur for quasi-one-dimensional overlayers structures [1,2], which results in the abrupt change in the lattice compressibility [3]. This type of lattice stiffening/softening transition has been observed for various systems, including a crystal made of parallel insulating polymer chains [4] and Gd/W(112) and Gd/Mo(112), in which Gd atoms form the chain-like structure on the furrowed substrates [5]. These transitions [4,5] are identified with the abrupt change in the effective Debye temperature across the transition temperature. Below the transition temperature of 240 K the gadolinium overlayer lattice has much higher effective Debye temperature than that observed for higher temperatures [5]. However, the detailed mechanism of these structural phase transitions are yet unknown. It was presented in the preceding chapters that Au/Mo(112) exhibits pronounced electron-phonon coupling near the surface and the strong phonon nesting condition within certain temperature range, which implies possible lattice instability. Thus, it is interesting to investigate if, in fact, Au/Mo(112) undergoes similar structural phase transitions, characterized by the abrupt change in the effective Debye temperature.

9.2 Experimental details

The scanning tunneling microscopy (STM) and low energy electron diffraction (LEED) experiments were performed in separate ultra high vacuum (UHV) chambers.

The scanning tunneling microscopy (STM) experiments were performed using a commercial Omicron variable temperature STM apparatus under the same conditions used for the LEED, photoemission and Auger electron spectroscopy measurements [6]. Much of experimental work was undertaken by Dr. Yaroslav Losovyj at Louisiana State University and the experimental data analysis was performed by me.

The LEED experiments were performed in the same UHV chamber as the photoemission spectroscopy [6] with the pressure of $1x10^{-10}$ torr. The LEED intensities were obtained as a function of electron kinetic energy and temperature using a CCD camera. Surface structures and surface order are seen to be strongly dependent upon Au coverage. The LEED images were taken at various substrate temperatures for each of the nominal gold coverages of 1.66 monolayer (ML), and 1.75 ML. The gold overlayers adopt ordered structures on Mo(112) corresponding to the 3x1 structure for 1.66 ML, and the 4x1 structure for 1.75 ML, as illustrated in Figure 4.2. The temperature dependent intensity analysis on LEED was performed for each of these overlayer gold coverages with the temperature ranging from approximately 300-800 K.

The surface of the Mo(112) crystal was cleaned by the method described in section 4.1 [6-9]. The quality of the surface order for the Mo(112) surface and Au overlayers was verified by LEED. Surface cleanness was monitored by Auger electron spectroscopy and photoemission. The crystal temperature was controlled by a combination of cooling with liquid nitrogen and resistive heating. The temperature was monitored with a W-5% Re/W-26% thermocouple with an accuracy of ±5 K.

9.3 Effective Debye temperature

It is known that the intensity of the LEED spots decays exponentially as a function of temperature, and can be quantified by Debye-Waller model (see section 3.3). Thus, by extracting the temperature dependence of the LEED spots, it is possible to obtain the effective Debye temperature from the following equations [8-13]:

$$\begin{aligned} I &= I_0 \exp(-2W) \\ 2W &= \frac{3\hbar^2 T(\Delta k)^2}{m k_B \Theta_D^2} \end{aligned} \qquad (9.1)$$

,

where W is the Debye-Waller factor as introduced in chapter 3, T is the temperature of the sample (in Kelvin), $\hbar(\Delta k)$ is the electron momentum transfer, m is the mass of the scattering center, k_B is the Boltzmann constant, and Θ_D is the effective Debye temperature. The magnitude of momentum transfer is given by:

$$|\Delta k| = |k_f - k_i| = |2k\cos\frac{\theta}{2}| \,, \qquad (9.2)$$

where θ is the angle between surface normal and diffracted electron beam. Due to geometry of our LEED experiments, sin(θ/2) (surface-parallel component of Δk) is much smaller than cos(θ/2) (surface-normal component of Δk). Thus, the calculated effective surface Debye temperature is most indicative of the vibrational modes normal to the surface [8-11].

In determining the intensity of LEED spots, the brightness in the fixed region around the spot was integrated and the background intensity was subtracted, a procedure similar to the temperature-dependent LEED analysis performed elsewhere [10-11]. Here we have also normalized to the value of the LEED spot intensities to the value obtained at the lowest temperature in each of the Au coverages on Mo(112), as is the common practice [8,11-13]. Although the superstructure spots (or fractional order spots) are produced by Au adatoms and it is reasonable to take the mass of the Au atom as the mass of the scattering centers *m* in equation (8.1), for the integral order spots, both the Au atoms and the Mo atoms contribute to the LEED spot intensity. For this reason, we have taken the geometric average of the masses of Au and Mo as the mass of the scattering center for the integral order spots analyzed in each of the Au coverages.

9.4 The surface order-disorder transition

The structure of gold adlayers on Mo(112) at the coverage of 1.66 ML forms the missing row 3x1 structure (two filled rows and one empty row parallel to the $<\bar{1}\bar{1}1>$ direction) as seen in the STM image in Figure 9.1c and d, which can be compared to those for the stoichiometric coverage (1 ML) as in Figure 9.1a and b. This structure can also be identified by the LEED image in Figure 4.2c, with two fractional order diffraction spots observed between the integral order diffraction spots. As seen in Figure 9.2a, the LEED intensity (logarithmic scale) as a function of temperature for integral order spot shows an abrupt change in the slope near 468 K. Thus, in an attempt to fit this graph (Figure 9.2a) with the Debye-Waller model (which gives straight line in the semi-log scale in Figure 9.2a), two separate fits must be used for each temperature region (i.e., above and below ~468 K), giving the two different effective Debye temperatures in the two regions. Although we have attempted to fit the entire range of data by including the 2nd dominant term in the Debye-Waller factor, as in:

$$2W = \frac{3\hbar^2(\Delta k)^2 T}{m k_B \Theta_D^2}\left[1+\frac{1}{36}\left(\frac{\Theta_D}{T}\right)^2+\cdots\right] , \tag{9.3}$$

the attempt was fruitless as in the case of Gd chains [5]. Furthermore, this need for two different effective Debye temperatures to fit our data is more evident in the temperature dependent intensities of the fractional order spots induced by the 3x1 structure of the gold overlayer as in Figure 9.2b. The abrupt change in the slope is easily identified near 470 K, the same temperature as in the case of integral order spots.

We have, therefore, a direct indication that there is a structural phase transition near 468 K, which significantly affects the stiffness of the phonons (or ionic vibrations). At this transition temperature, the surface effective Debye temperature dramatically decreases from 219±15 K to about 70±10 K as determined from the fractional order spots (the values are summarized in Table 9.1). For the integral order 1x1 diffraction spots this decrease in effective Debye temperature is less dramatic (386 to 184 K). As the integral order spots are produced by both Au and Mo atoms, if the structural phase transition has occurred only for Au overlayer and not for the Mo(112) surface, the observed less dramatic change in the effective Debye temperature can be qualitatively explained. However, it is important to note that the possibility some structural change in Mo(112) cannot be *a priori* excluded and the definite conclusion must be drawn from more complete quantitative analyses.

The similar behavior is also observed in the intensity of the fractional order diffraction spots at a coverage of 1.75 ML of gold (corresponding LEED image and structure are illustrated in Figure 4.2d) as seen in Figure 9.3b, where the gold overlayer forms a missing row 4x1 structure. Here the effective surface Debye temperature drops from 177±20 K to 63±15 K, at a critical temperature of about 407 K as determined from the fractional order spots (see Table 9.1). Note that for the integral order spots, the abrupt change in the effective Debye temperature (slope of Figure 9.3a) was not identified, which is perhaps due to the high kinetic energy of the electrons which probes several layers below the surface of Au/Mo(112). Thus, there is also a direct evidence of the structural phase transition for the Au overlayer of (4x1) 1.75 ML Au/Mo(112)

The abrupt change in the effective Debye temperature, as found for (3x1) 1.66 ML and (4x1) 1.75 ML Au/Mo(112) implies the sudden softening of phonon modes, particularly the ones polarized along the surface normal direction, across the transition temperature. Thus, it is evident that Au overlayer has undergone some structural phase transition and has led to the observed sudden softening of the lattice above the transition temperatures. In identifying the type of this structural phase transition for 1.66 and 1.75 ML, it is important to notice that, besides the rapid diminishing of the fractional order spots, no sudden change was observed in LEED patterns across the transition temperature (such as appearance/disappearance of extra spots). This likely means that the Au overlayer is significantly more disordered in the high-temperature phase, because if the Au overlayer was still ordered (commensurate or incommensurate) above the structural phase transition, appearance of additional spots ought to be observed as the fractional order spots (observed at room temperature) diminish. Note that commensurate 3x1 to 1x1 transition for 1.66 ML (and 4x1 to 1x1 transition for 1.75 ML) is not possible because the both are non-stoichiometric coverages (i.e., they cannot form ordered 1x1 structure due to the geometry restriction). Supported by these evidences, we identify the structural phase transitions observed for 1.66 ML and 1.75 ML are of order-disorder transition of the Au overlayer.

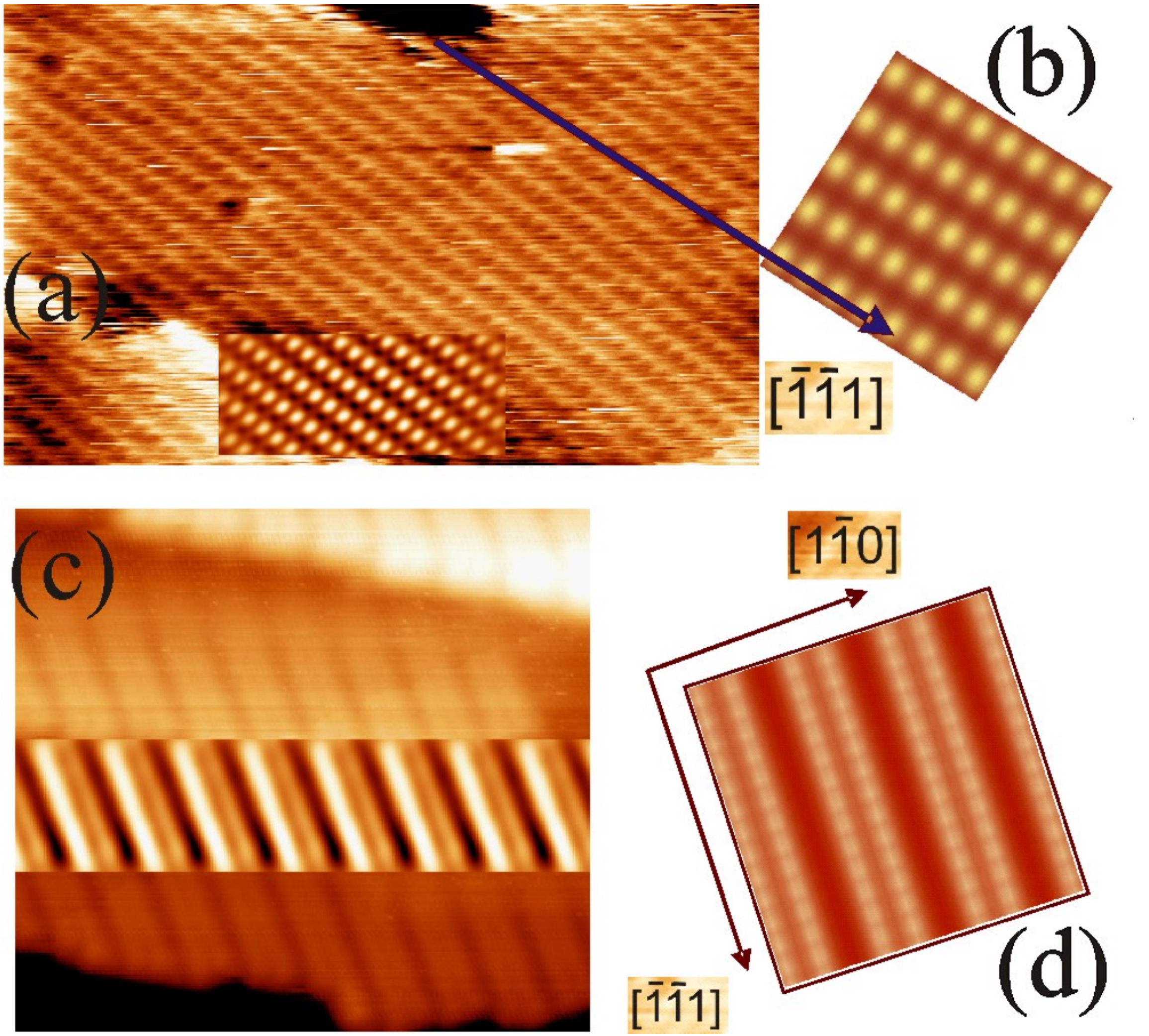

Figure 9.1: The STM images for Au/Mo(112) for (1x1) 1 ML and (3x1) 1.66 ML coverages. (a) The image for the stoichiometric coverage of 1 ML, where the inset shows the fast Fourier transform (FFT) of the image. (b) The simulated STM image for 1 ML coverage based on the images in (a). (c) The image for the (3x1) 1.66 ML coverage, where the inset shows the fast Fourier transform (FFT) of the image. (d) The simulated STM image for 1.66 ML coverage based on the images in (c).

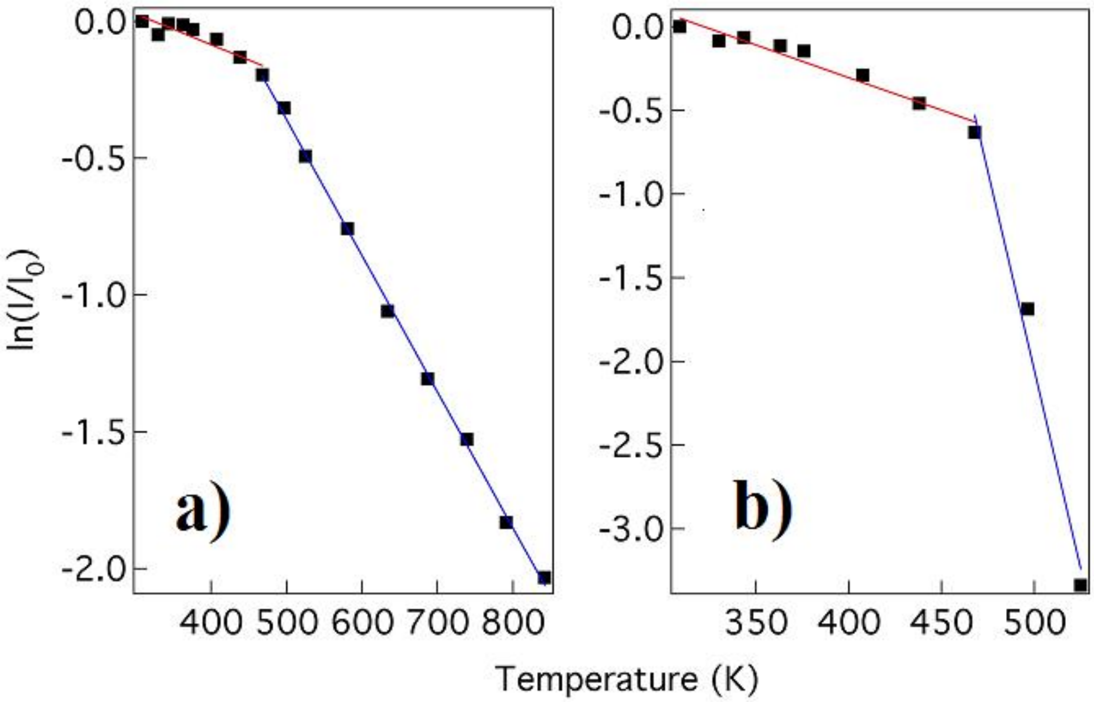

Figure 9.2: The intensity of the LEED spot for (3x1) 1.66 ML Au/Mo(112) as a function of temperature for (a) the integral order spot, and (b) fractional order spot. Note the log scale of the intensity referenced to the *I_0* (the LEED spot intensity at the lowest temperature analyzed)

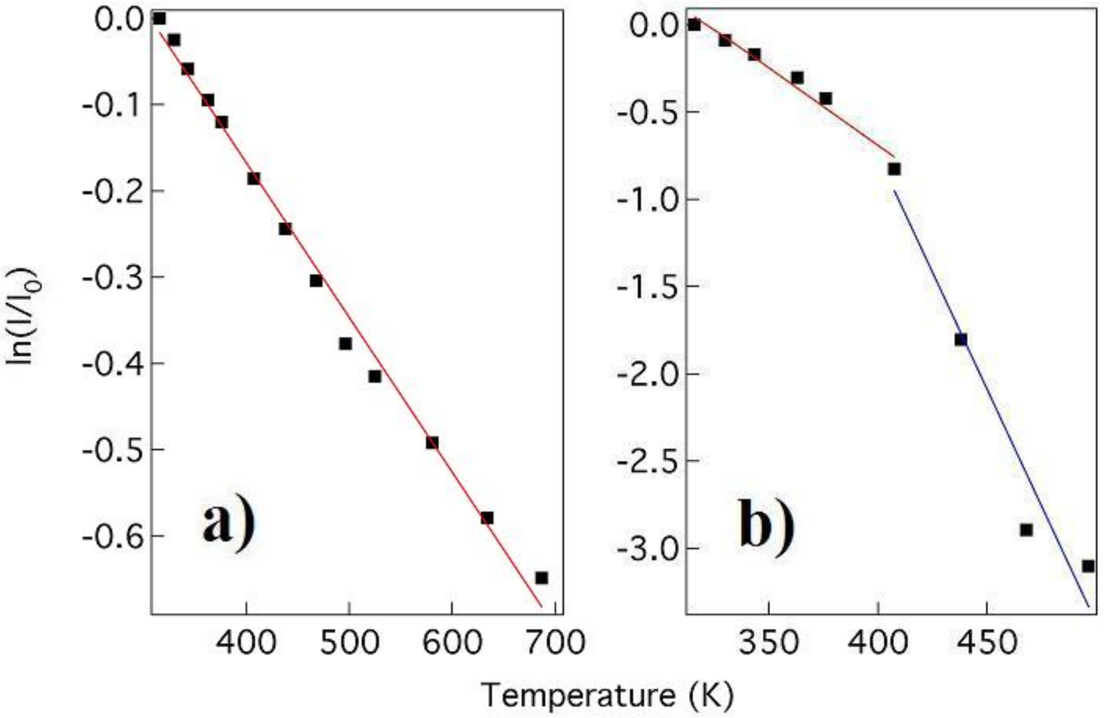

Figure 9.3: The intensity of the LEED spot for (4x1) 1.75 ML Au/Mo(112) as a function of temperature for (a) the integral order spot, and (b) fractional order spot. Note the log scale of the intensity referenced to the I_0 (the LEED spot intensity at the lowest temperature analyzed)

Nominal Au Coverage (ML)	Θ_D $T< T_c$	order-disorder T_c	Θ_D $T>T_c$
1.66	219±15 K (386±30 K)*	468±10 K	70±10 K (184±50 K)*
1.75	177±20 K	407±10 K	90±15 K

Table 9.1: The estimated effective surface Debye temperature Θ_D above and below the transition temperature T_c for each of 1.66 and 1.75 ML coverages, obtained from the fractional order spots. *The values in parentheses indicate the effective Debye temperature obtained from the integral order spots, which contains more contribution from the Mo atoms than for the fractional order spots.

9.5 Summary

The order-disorder structural phase transitions were observed for the Au overlayer structure of Au/Mo(112) at 1.66 ML and 1.75 ML. These transitions are accompanied by the significant softening of the lattice identified by the abrupt change in the effective surface Debye temperature, as determined by our temperature-dependent LEED analyses.

For 1.66 ML Au/Mo(112), which exhibits commensurate 3x1 structure at room temperature, the order-disorder transition temperature was identified to be ~ 470 K. Above this temperature, the effective Debye temperature was estimated to be about 70±10 K which is in sharp contrast to 219±15 K below the transition temperature. The same type of transition was observed also for the 1.75 ML (commensurate 4x1 structure) coverage, but with slightly lower transition temperature of ~407 K. For this coverage, the effective Debye temperature was estimated to be 177±20 K below the transition and 63±15 K above the transition.

References

[1] I.N. Yakovkin, *J. Nanoscience and Nanotechnology* **1**, 357 (2001).

[2] P.A. Dowben, *Surface Science Reports* **40**, 151 (2000).

[3] A. Moreo, S. Yunoki and E. Dagotto, *Science* **283**, 2034 (1999).

[4] C.N. Borca, S. Adenwalla, J. Choi, P.T. Sprunger, S. Ducharme, L. Robertson, S. P. Palto, J. Liu, M. Poulsen, V.M. Fridkin, H. You and P.A. Dowben, *Phys. Rev. Lett.* **83**, 4562 (1999).

[5] Ya.B. Losovyj, I.N. Yakovkin, H.-K. Jeong, D. Wisbey, P.A. Dowben, *J. Phys. Cond. Matter.* **16**, 4711 (2004).

[6] Ya.B. Losovyj, I. Ketsman, N. Lozova, J. Scott, P.A. Dowben, I.N. Yakovkin, S.M. Zuber, *Appl. Surf. Sci.* **254**, 4236 (2008).

[7] J. Zhang, D.N. McIlroy, P.A. Dowben, Phys. Rev. B **49**, 13780 (1994).

[8] C. Waldfried, D.N. McIlroy, J. Zhang, P.A. Dowben, G.A. Katrich and E.W. Plummer, *Surface Science* **363**, 296 (1996).

[9] Ning Wu, Ya. B. Losovyj, Zhaoxian Yu, R.F. Sabirianov, W. N. Mei, N. Lozova, J.A. Colón Santana, and P.A. Dowben, *J. Phys. Cond. Matter* **21**, 474222 (2009).

[10] M.A. Van Hove, W.H. Weinberg, C.M. Chan in: *Low-Energy Electron Diffraction*, (Springer Series in Surface Science, vol. 6, 1986) pp.134

[11] L.J. Clarke, *Surface Crystallography*, (Wiley, New York, 1985)

[12] H.K. Jeong, Takashi Komesu, P.A. Dowben, B.D. Schultz and C.J. Palmstrøm, *Physics Letters* A **302**, 217 (2002).

[13] N. Wu, D. Wisbey, T. Komesu, Z.X. Yu, M. Manno, L. Wang, C. Leighton, P.A. Dowben, *Physics Letters* A **372**, 2484 (2008).

Chapter 10
Conclusion and future

10.1 What do we think we understand?

As mentioned in the introduction, the two critical factors that contribute to the instability of the surface crystal structure are the strength of the electron-phonon coupling and the phonon nesting conditions of the Fermi surface. Our investigation on Au/Mo(112) (chapter 7) revealed the pronounced electron-phonon coupling for the surface resonance states, which is signified by the large mass enhancement parameter (λ) as high as 0.7, which is in contrast to $\lambda < 0.46$ for Mo(112). Such pronounced electron-phonon coupling near the interface of Au/Mo(112) makes the system more susceptible (compared to the clean Mo(112)) towards the formation of charge density wave and surface lattice distortion.

Another critical factor, the Fermi surface topology, has also been explored in this study for the (4x1) 1.75 ML Au/Mo(112). The ARPES-derived Fermi surface contour exhibits the nearly straight segment parallel to the $<1\bar{1}0>$ direction, composed of the surface resonance states of the system. This Fermi contour segment spans the large portion of the surface Brillouin zone in this direction. The presence of such feature in the Fermi surface is a characteristic of the quasi-one-dimensional structure of Au overlayer on Mo(112), which is expected to result in the enhanced response of the electrons to the applied 'perturbation' of phonons at particular wave vector ($2k_F$). Thus, as a result of the present study, the strength of both the electron-phonon coupling and the nesting conditions of Fermi surface have been identified and found to favor the occurrence of surface lattice instability.

The temperature dependence of the nearly straight Fermi contour segment, mentioned above, in (4x1) Au/Mo(112) is of further interest, particularly above 230 K, for which the discernable change is observed. At ~290 K, the Fermi contour segment is seen to be almost precisely straight within the experimental error. Such temperature-driven change in the Fermi surface is a direct indication of structural changes in the system. Moreover, the change in the Fermi surface persisted above 290 K in non-monotonic manner, which further modifies the nesting condition at higher temperatures.

Although the detailed mechanism is yet to be discovered, the combination of strong electron-phonon coupling and the non-monotonic temperature-dependent Fermi surface nesting condition likely implies the existence of structural phase transitions (possibly) at multiple temperatures. We believe that the order-disorder transition observed for (4x1) 1.75 ML Au/Mo(112) is closely related to such special properties of Au/Mo(112).

10.2 What is not fully understood?

Although the series of studies performed on Mo(112) and Au/Mo(112) has resulted in the number of findings related to their many-body interactions and the structural phase transitions, this is by no means the end of the story. That is to say, the most fundamental mechanism which bridges the two phenomena are not yet understood. Evidently, it takes more time and effort to find such bridge. Therefore, in this last section, we suggest several studies to be performed in order to approach the ‘solution’ to this problem.

First, the order-disorder transitions identified on the Au/Mo(112) must be further characterized. The analysis of integrated intensity can identify the existence of the phase transition. However, in the future, it would be desirable to quantify the evolution of the LEED spots (both the intensity and the width) in the close vicinity of the phase transition. Perhaps the utilization of SPA-LEED is ideal. At the same time, it is important that such experiment be performed for heating as well as cooling across the transition temperature. Such experiments should, in principle, identify whether the transition is of 1st order (irreversible) or 2nd order (reversible) with the presence or absence of the hysteresis, and if the experimental precision permits, the critical exponents pertinent to the phase transition could be obtained.

It is worthwhile to point out that based on the Lifshitz condition [1], which imposes the symmetry restriction on continuous phase transition, the continuous order-disorder transition of Au overlayer structure for (3x1) and (4x1) Au/Mo(112), which exhibits rectangular symmetry, are not allowed. However, the Lifshitz condition assumes the presence of ‘global’ or ‘perfect’ symmetry and thus, if the overlayer system exhibits only a ‘local’ symmetry, such as in the presence of domain structures etc., the system is in fact, allowed to undergo the continuous order-disorder transition [2,3]. It has been pointed out that dislocations of atoms in the (*p*x1) rectangular lattice, where $p \geq 3$, can form multiple types of domain walls. From such phase, the system can undergo the continuous transition, classified as chiral *p*-states Potts model [4]. Thus, if the order-disorder transitions on (3x1) and (4x1) Au/Mo(112) are to be identified as continuous, then between the ordered and the disordered phase, there must exist another phase, which is still ordered, but lacks the global symmetry. In order to test for the existence of such phase, the temperature-dependent STM measurements may be an ideal experimental probe, although perhaps the imaging difficulties at high temperature must be overcome. In fact, we suspect that the observed temperature-dependent change in the Fermi surface at (4x1) 1.75 ML may be related to the structural phase transition from the ordered phase (< 290 K) to this intermediate phase of broken global symmetry (> 290 K).

In order to elucidate the possible role of many-body interactions in driving the order-disorder transition on Au/Mo(112), we believe it is critical to carry out the high-resolution ARPES experiments for the disordered phase. Across the transition temperature, the role of electron-phonon coupling and the nesting phonons can be elucidated by calculating the Lindhard response function from the experimental Fermi surface contour, as done for 2*H*-$TaSe_2$ and similar materials [5-7]. Such method allows for the identification of phonon mode(s) providing the critical perturbation to the electronic as well as the structural instability towards the formation of charge density wave and the lattice distortions and its possible roles in driving the observed order-disorder transitions on Au/Mo(112).

References

[1] M. Schick, *Progress in Surface Science* **11**, 245 (1981).

[2] D.A. Huse and M.E. Fisher, *Phys. Rev. Lett.* **49**, 793 (1982).

[3] D.A. Huse and M.E. Fisher, *Phys. Rev.* B **29**, 239 (1984).

[4] Y.N. Yang, E.D. Williams, R.L. Park, N.C. Bartelt and T.L. Einstein, *Phys. Rev. Lett*. **64**, 2410 (1990).

[5] S.V. Borisenko, A.A. Kordyuk, A.N. Yaresko, V.B. Zabolotnyy, D.S. Inosov, R. Schuster, B. Buchner, R. Weber, R. Follath, L. Patthey and H. Berger, *Phys. Rev. Lett.* **100**, 196402 (2008).

[6] D.S. Inosov, D.V. Evtushinsky, V.B. Zabolotnyy, A.A. Kordyuk, B. Buchner, R. Follath, H. Berger and S.V. Borisenko, *Phys. Rev.* B **79**, 125112 (2009).

[7] D.S. Inosov, V.B. Zabolotnyy, D.V. Evtushinsky, A.A. Kordyuk, B. Buchner, R. Follath, H. Berger and S.V. Borisenko, *New Journal of Physics* **10**, 125027 (2008).

Appendix A
Selection rules on electron-phonon coupling

The matrix element that describes the electron-phonon coupling is given by [1,2]

$$\langle \alpha', \beta' | H_{ep} | \alpha, \beta \rangle , \tag{A.1}$$

where H_{ep} is the electron-phonon coupling Hamiltonian and α (α') and β (β') denote the complete set of quantum numbers for initial (final) electron state and phonon state respectively. In the rigid-ion approximation [1,2], H_{ep} can be written in position basis as

$$H_{ep} = \sum_j u_j \cdot \nabla V(r - R_j) , \tag{A.2}$$

where u_j is the small displacement of j-th ion from its equilibrium position R_j. Assuming the electronic part of the wave function can be written as a product of Bloch states, the coupling of a single electron with wave vector k with phonon mode of wave vector q and polarization p can be described by the matrix element

$$M_{ep} = \langle \beta' | \int \psi^*_{k'} \sum_j u_j \cdot \nabla V(r - R_j) \psi_k d^3 r | \beta \rangle , \tag{A.3}$$

where ψ_k and $\psi_{k'}$ denote the initial and final electronic wave functions, respectively. Since the displacement u_j is an operator which acts on the phonon states,

$$u_j = -i \sum_{q,p} \left(\frac{\hbar}{2NM\omega_{q,p}} \right)^{1/2} e^{iq\cdot R_j} \left(a^+_{q,p} + a_{-q,p} \right) \hat{p} , \tag{A.4}$$

where $a^+_{q,p}$ and $a_{-q,p}$ are the creation and annihilation operators of phonon with wave vector q and polarization p respectively, and $\hat{p}$ is the phonon polarization unit vector. The matrix element becomes

$$M_{ep} = \sum_j \langle \beta' | -i \sum_{q,p} \left(\frac{\hbar}{2NM\omega_{q,p}} \right)^{1/2} e^{iq\cdot R_j} \left(a^+_{q,p} + a_{-q,p} \right) | \beta \rangle \int \psi^*_{k'} \hat{p}_j \cdot \nabla V(r - R_j) \psi_k d^3 r , \tag{A.5}$$

where N is the number of ions, M is the ion mass, and $\omega_{q,p}$ is the frequency of the phonon mode (q, p). The phonon part of matrix element vanishes unless the initial and final states differ in the occupation number of the mode (q, p) by unity. In particular, if we take the process in which one particular phonon of (q, p) is emitted by an electron, we have

$$\begin{aligned} M_{ep} &= \sum_j \left\langle n_{q,p} \right| -i\left(\frac{\hbar}{2NM\omega_{q,p}}\right)^{1/2} e^{iq\cdot R_j}\left(a^{+}_{q,p}+a_{-q,p}\right)\left| n_{q,p}-1\right\rangle \int \psi^{*}_{k'}\hat{p}_j\cdot\nabla V(r-R_j)\psi_k d^3r \\ &= \sum_j -i\left(\frac{\hbar n_{q,p}}{2NM\omega_{q,p}}\right)^{1/2} e^{iq\cdot R_j}\int \psi^{*}_{k'}\hat{p}_j\cdot\nabla V(r-R_j)\psi_k d^3r \end{aligned} \quad , \text{(A.6)}$$

where $\left|n_{q,p}\right\rangle$ denotes the state in which there is $n_{q,p}$ phonons of mode (q, p) (the occupation numbers for all the other phonon modes are omitted for brevity). Note that q and p now denote the wave vector and the polarization of specific phonon mode involved in the electron-phonon coupling and are no longer the running index of summation. Since the phonon part of the matrix element is now constant, the electron-phonon coupling selection rule is dictated by the electronic part of the matrix element

$$\sum_j \int \psi^{*}_{k'}\hat{p}_j\cdot\nabla V(r-R_j)\psi_k d^3r\,. \quad \text{(A.7)}$$

In general, the integral must vanish if the triple tensor product of irreducible representations of initial state, final state and perturbation operator does not contain a fully symmetric representation. In the present study, the band renormalization is observed for the electronic states near the Fermi level along $\bar{\Gamma}-\bar{\mathrm{X}}$ direction and the symmetry of the associated wave functions were found to be even with respect to the reflection about *xz*-plane (i.e., transforms as A’ representation in C_{1h} group). Thus, the phonons with wave vector along $\bar{\Gamma}-\bar{\mathrm{X}}$ direction are allowed to couple with these electrons of A’ symmetry only if the polarization of phonon and the final electronic state share the same symmetry (i.e., both A’ or both A”). In particular, for the coupling with $q = 2k_F$, for which the initial and final electronic states share the same symmetry (A’), we are lead to conclude that the coupling phonons must also have A’ symmetry. Since the horizontal transverse mode (marked brown in Figure 7.5) transforms as A”, it cannot serve as a coupling mode and hence not expected to contribute to the Eliashberg function or the observed band renormalization (at least for the contribution due to electron-phonon coupling). It is important to note that this selection rule only applies when the initial and final electronic states lie along the same symmetry axis. For any final states at the general point in the SBZ (near the Fermi level), the symmetry selection rule does not a priori exclude the possibility of electron-phonon coupling, provided, of course, the existence of phonon modes which conserve the momentum.

References

[1] G. Grimvall, *The Electron-Phonon Interaction in Metals* (Selected Topics in Solid State Physics XVI), 1st ed. (Elsevier Science Ltd, 1981).

[2] J. M. Ziman, *Electrons and Phonons: the Theory of Transport Phenomena in Solids* (Oxford University Press, USA, 2001).